NATIONAL & INTERNATIONAL SCIENTIFIC EVENTS

The 49th International Congress and Exposition on Noise Control Engineering

Venue: Convention and Exhibition Center
Location: Seoul, Korea

Begins: August 23, 2020
Ends: August 26, 2020

36th European and 12nd International Peptide Symposium

Venue: Hotel Meliá Sitges
Location: Barcelona, Spain

Begins: August 30, 2020
Ends: September 04, 2020

FISITA World Congress 2020

Venue: O_2 Universum
Location: Prague, Czech Republic

Begins: September 14, 2020
Ends: September 18, 2020

14th International Conference on Hydroscience and Engineering

Venue: Radisson Blu Resort & Spa
Location: Cesme, Turkey

Begins: September 22, 2020
Ends: September 25, 2020

46th Annual Conference of the IEEE Industrial Electronics Society-IECON 2020

Venue: Marina Bay Sands Expo and Convention Centre
Location: Malaysia

Begins: October 18, 2020
Ends: October 21, 2020

23rd International Conference on Electrical Machines and Systems (ICEMS2020)

Venue: ACT CITY Hamamatsu
Location: Hamamatsu, Japan

Begins: November 24, 2020
Ends: November 27, 2020

14th Mediterranean Congress of Chemical Engineering

Venue: Gran Via
Location: Barcelona, Spain

Begins: December 1, 2020
Ends: December 4, 2020

73rd Annual Session of Indian Institute of Chemical Engineers (CHEMCON2020)

Venue: Institute of Minerals & Materials Technology
Location: Bhubaneswar, India

Begins: December 27, 2020
Ends: December 30, 2020

39th IEEE International Conferenceon Consumer Electronics (ICCE 2021)

Location: Las Vegas, USA

Begins: January 10, 2021
Ends: January 12, 2021

8th International Conference on Geological and Civil Engineering (ICGCE 2021)

Location: Tokyo, Japan

Begins: January 28, 2021
Ends: January 30, 2021

33rd International Symposium on Power Semiconductor Devices and ICs (ISPSD)

Venue: Nagoya Congress Center
Location: Nagoya, Japan

Begins: May 30, 2021
Ends: June 3, 2021

35th IAS Meeting of Sedimentology

Venue: Conference Centre of the Vienna House Diplomat Hotel
Location: Prague, Czech Republic

Begins: June 22, 2021
Ends: June 24, 2021

Abstracted & Indexed in:

TR Dizin Mühendislik ve Temel Bilimler Veri Tabanı | CrossRef | Google Scholar | MIP Database | StuartxChange | ResearchBib | Scientific Indexing Services (SIS)

HITTITE

HJSE Official Journal of Hitit University Volume 7, Issue 2, 2020 www.hjse.hitit.edu.tr

ISSN 2148-4171

HITIT UNIVERSITY

JOURNAL OF SCIENCE & ENGINEERING

HITTITE

Volume 7, Issue 2, 2020

www.hjse.hitit.edu.tr

HJSE Official Journal of Hitit University Volume 7, Issue 2, 2020 www.hjse.hitit.edu.tr

JOURNAL OF SCIENCE & ENGINEERING
HITTITE

JOURNAL OF SCIENCE & ENGINEERING
HITTITE

CONTENT

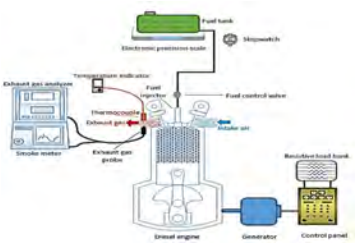

The objective of the present experimental research deal with the exploring and compare the inf luence of the ternary fuel mixtures of petroleum-based diesel fuel, cottonseed oil me-thyl ester (COME) and long-chain alcohols of isopropanol (Pr), 1-butanol (Bt), and isopentanol (Pt) on the performance and emission characteristics of a single-cylinder, four-stroke, naturally-aspirated, direct-injection compression-ignition (CI) engine.

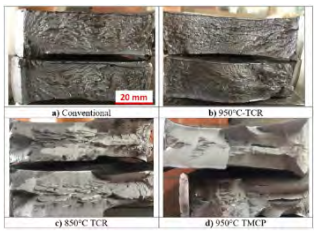

This study was undertaken to determine the controlled rolling and cooling conditions for the production of 20 mm thick American Petroleum Institute (API) X60 and X70 grade steel plates.

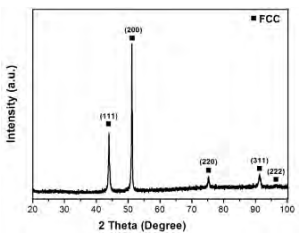

The structure and mechanical properties of CoCrFeNi and CoCrFeNiTi0.5Al0.5 (in molar ratio) high entropy alloys were investigated using X-ray diffraction (XRD), optical microscope (OM), scanning electron microscope (SEM), hardness and compression tests.

Owner
Prof. Dr. Ali Osman ÖZTÜRK
on behalf of Hitit University

Editor-in-chief
Prof. Dr. Ali KILIÇARSLAN

Associate Editors
Prof. Dr. D. Ali KÖSE
Assist. Prof. Dr. Öncü AKYILDIZ

Production
Assoc. Prof. Dr. Kazım KÖSE
Mustafa Reşit HABOĞLU
Erhan ÇETİN
Tugrul YILDIRIM
Harun Emre KIRAN
Ömer Faruk TOZLU

Editor's Office
Tel: +90 364 227 45 33 / 12 36
Fax: +90 364 227 45 35
Email: alikilicarslan@hitit.edu.tr

Subscription Service:
Tel: +90 364 227 45 33 / 12 82
Fax: +90 364 227 45 35
Email: hjse@hitit.edu.tr

EDITORIAL BOARD

Journal Name	: HITTITE JOURNAL OF SCIENCE AND ENGINEERING
Year	: 2020
Managing Editor	: Prof. Dr. Ali KILIÇARSLAN
Managing Office	: Hitit University Faculty of Engineering
Managing Office Tel	: +90 364 227 45 33 / 12 36
Publication Language	: English
Publication Type	: Peer Reviewed, Open Access, International Journal
Delivery Format	: 4 times a year (quarterly)
Print ISSN	: 2149-2123
Online ISSN	: 2148-4171
Publisher Address	: Hitit Üniversitesi Kuzey Kampüsü Çevre Yolu Bulvarı 19030 Çorum / TÜRKİYE
Publisher Tel	: +90 364 227 45 33/1236

This new issue of Hittite Journal of Science and Engineering contains twelve manuscripts from the disciplines of chemistry, civil engineering, geomatics engineering, mechanical engineering, materials science and engineering. These manuscripts was first screened by Section Editors using plagiarism prevention software and then reviewed and corrected according to the reviewer's comments. I would like to express my gratitude to all our authors and contributing reviewers of this issue.

I would like to thank to the new President of Hitit University, Prof. Dr. Ali Osman Öztürk, for his support and interest in HJSE and also to the Associate Editors of HJSE, namely Prof. Dr. Dursun Ali Kose and Asst. Prof. Dr. Oncu Akyildiz, as well as our Production Editors Dr. Kazim Kose, Mustafa Reşit Haboğlu, Erhan Çetin, Tugrul Yildirim, Harun Emre Kıran and Ömer Faruk Tozlu for their invaluable efforts in making of the journal.

It's my pleasure to invite the researchers and scientists from all branches of science and engineering to join us by sending their best papers for publication in Hittite Journal of Science and Engineering.

Dr. Ali Kilicarslan

Editor-in-Chief

Hittite Journal of Science and Engineering, 2020, 7 (2) 81-87
ISSN NUMBER: 2148-4171
DOI: 10.17350/HJSE19030000176

An Investigation upon DNA Interaction of 2 (3), 9 (10), 16 (17), 23 (24) –Tetrakis 4-(4-(2-phenylprop-2-yl) phenoxy) Phthalocyanine Compound

Ali Arslantas[1], Mehmet Salih Agirtas[2] and Cihan Durmus[2]
[1]Karabuk University, Biomedical Engineering, Karabuk/Turkey
[2] Van Yuzuncu Yil University, Chemistry, Van/Turkey

ABSTRACT

The DNA binding activity of previously synthesized and characterized 2(3), 9(10), 16(17), 23(24) –Tetrakis 4-(4-(2-phenylprop-2-yl) phenoxy) phthalocyanine compound (PcF) with CT-DNA was studied using UV/Vis, emission spectroscopic titrations, the melting temperature, viscosity measurement, and agarose gel electrophoresis methods in a Tris-HCl buffer solution at a pH of 7.1 at room temperature. The absorption titration spectra studies of PcF showed that absorbance intensities were decreased with increasing of concentrations of CT-DNA and the finding proved that the compound interacts with the DNA. Addition to absorption titration study, emission spectroscopic titration, the melting temperature, viscosity measurement, and agarose gel electrophoresis methods were also performed to investigate the binding activities of PcF with the DNA. The results of these methods confirmed the findings of absorption spectra study that the compound interacts with the DNA.

Keywords:
Absorption spectra; Fluorescence spectroscopy; DNA binding; Phthalocyanines.

Article History:
Received: 2019/10/10
Accepted: 2020/05/29
Online: 2020/06/26

***Correspondence to**: Ali Arslantas,*
Karabuk University, Biomedical Engineering,
78050, Karabuk, TURKEY
E-Mail: arsoz33@gmail.com
Phone: +90 (370) 433 70 21
Fax: +90 (370) 433 32 90

INTRODUCTION

Phthalocyanine compounds have several important chemical properties due to their chemical structures. Nowadays, phthalocyanine compounds have great attention from scientists around the world because of their explicit applications including photodynamic treatment [1], sensors [2], pigments [3], chemotherapy treatment and enzymatic inhibitors [4, 5]. Around the world, a great number of human beings suffer from deadly carcinoma, and many people die every day due to cancer [6]. It is reported in the literature that cancer is a very critical health problem worldwide, and it is expected that it will keep causing the deaths of numerous people in the near future [7]. Due to these reasons, chemotherapy treatment and studies on preventing cancer have gained great importance. Therefore, designing cancer drugs is a fundamental concern for overcoming this fatal disease. Recently, there has been significant progress in treatments against cancer cells. On the other hand, this progress has not yet reached the desired level. As stated in the recent literature, many researchers have particularly focused on the cell cycle and DNA molecule [7, 8]. The interaction between therapeutic drugs and DNA may change DNA's structure and transcription of the DNA molecule [9, 10]. Binding is considered to be where the major binding mode of tiny healing biological molecules with the DNA takes place via the intercalation and non-intercalation binding modes [10, 11].

Recently, various studies have been carried out on the binding of phthalocyanines to DNA molecules. Various phthalocyanine-containing groups could bind to DNA molecules by either of intercalation and non-intercalation mechanisms [12]. The reactivity of phthalocyanines may be modified by changing their peripheral ligands [13]. For instance, it was reported that the phenoxy-acetamide-substituted metal phthalocyanine complex is a biologically active compound. The phthalocyanine metal complex with octakis phenoxy acetamide ligands could have potential applications in cancer treatment [14] and antibacterial healing [14, 15].

The binding of phthalocyanines to the DNA can inhibit the spread of cancer cells, and this health issue has gained great attention. Many interesting studies have been conducted in this field. Phthalocyanine compounds could be very useful therapeutic agents for inc-

reasing the scope of anticancer research. In this study, the DNA binding activities of previously synthesised 2(3), 9(10), 16(17), 23(24)–tetrakis4-(4-(2-phenylprop-2-yl)phenoxy) phthalocyanine compound as shown in Fig. 1[16] with calf thymus-DNA (CT-DNA) were analyzed by use of absorption spectral titration, fluorescence emission spectra, melting point temperature, agarose gel electrophoresis and viscosity studies.

MATERIAL AND METHODS

Materials

This study used the 2(3), 9(10), 16(17), 23(24)–tetrakis 4-(4-(2-phenylprop-2-yl) phenoxy) phthalocyanine compound [16] to examine its DNA binding activities. Tris-Hydrochloride and calf thymus DNA reagents were supplied owing to Aldrich and Sigma firms. Sodium chloride was provided by the Merck company and the entire reagents calf thymus- DNA, DNA ladder, TBE, Tris-HCl, NaCl, milli-Q water and DMF solvent were of biochemical grade. Hence, these reagents were utilized without further purification. The samples of calf thymus DNA were produced by using Tris-HCl and NaCl buffer solution. All the solutions were prepared with milli-Q water.

Absorption titrations for DNA binding activities of PcF were carried out with an Agilent Technologies Cary 60 UV/Vis spectroscope, while fluorescence titration experiments were conducted with a Perkin Elmer LS Fluorescence Spectroscope. A Thermo Scientific Owl Electrophoresis System was utilized for gel electrophoresis. Thermal melting temperatures were studied at 260 nm with UV/Vis spectroscopy. Ubbelohde viscometer experiments were carried out for viscosity measurement. The entire analyses were conducted in a Tris-HCl buffer solution at pH of 7.1 at controlled room temperature.

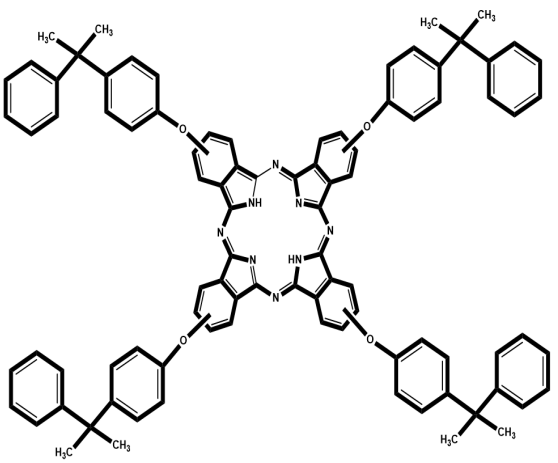

Figure 1. Chemical structure of the PcF compound.

The synthesis of PcF compound

In this study, PcF compound was prepared according to literature [16].

DNA binding experiments

In CT-DNA binding experiments, the changes in intensities of absorption spectrum are associated with the interaction between such compounds and DNA because of the packing of the aromatic part with DNA bases [17]. The DNA interaction of PcF at varied amounts were investigated based on absorption titration in the buffer solution at pH of 7.1 at controlled room temperature. PcF displayed absorbance peaks at around 675 nm, 640 nm and 340 nm. Adsorption spectroscopy was used the wavelength of 260 nm for calculating the molar extinction constant of the DNA molecule for preparing CT-DNA samples. The experiment showed that CT-DNA was protein-free [18]. UV/Vis titration spectra were analyzed from 300 to 800 nm. The findings from the experiment were compared to the control absorption titration spectra with Tris-HCl instead DNA for determining the dilution effects [18]. The binding constant of the PcF compound was computed with Wolfe-Shimmer formula [19].

Fluorescence spectra experiments

In this research, CT-DNA interactive properties of PcF using the fluorescence spectroscopy technique were studied in a Tris-HCl buffer at a fixed pH of 7.1. In this study, the calf thymus DNA (CT-DNA) sample was used to examine the interactive activities of PcF. The concentration of the compound (20 μM) was kept constant during titration with the increasing amounts of the DNA. The mixture consisted of PcF and the calf thymus DNA in a Tris-HCl and NaCl buffer at a pH 7.1. Firstly, the excitation of PcF compound was performed, and then, the emissions of the compound were recorded. The solution of CT-DNA and PcF was permitted to attain the equilibration for a certain time before the experiments were conducted [20, 21].

Thermal melting experiments

To verify CT-DNA interactive activities of PcF, thermal denaturation experiments were conducted by absorption spectroscopy of the DNA at varying concentrations in a Tris-HCl buffer at a constant pH 7.1. The melting temperature measurements were conducted at a constant wavelength [22-25] by using absorption spectroscopy. The sample of CT-DNA and PcF in the buffer solution at a pH of 7.1 containing sodium chloride were increased temperature from 25 to 95 °C every 5 mins. The values of ab-

sorption titrations were obtained after successive heating of the CT-DNA and PcF solution.

Viscosity measurement experiments

In this study, the viscosity studies were conducted the with Ubbelohde viscometer. The viscometer was submerged into a water-filled bath at a fixed temperature approximately 30 °C. The concentrations of PcF and ethidium bromide were increased to identify the DNA binding properties of PcF. The flow time was obtained by measuring the sample three times. The viscosity of the solution was obtained from $\eta_i = (t_i - t_0)/t_0$ equation. ηi represents the DNA viscosity and ti belongs to the time of flow of PcF and CT-DNA. t_0 indicates the flow time of the Tris-HCl buffer at pH of 7.1. Recorded values are shown for $(\eta / \eta_0)^{1/3}$ against [PcF]/[CT-DNA]. The η represents the viscosity of DNA in the presence of EB and PcF, and η_0 shows CT-DNA viscosity [26].

Agarose gel electrophoresis experiments

The binding of PcF to the DNA was investigated by the electrophoresis in a TBE buffer solution. In these experiments, the concentration of the compound was kept fixed at 20 μM, but the amounts of the DNA were increased from 0 to 25 μM and the results are shown in Fig. 5. CT-DNA samples (0, 5, 15, 25 μM) and PcF (20 μM) were loaded with the dye. Agarose gel electrophoresis experiments were conducted at 80 volts during 3 hours in the buffer solution, and the CT-DNA bands were then monitorized with a UV lamp. Agarose gel electrophoresis system from Thermo Scientific Owl company was used for this study [27-31].

RESULTS AND DISCUSSION

Absorption spectra experiments

Phthalocyanine compounds have two characteristic electronic spectra. One of these spectra appears approximately between 300 and 400 nm for the B-band and the other band is at about 600-780 nm for Q-band. For PcF, the typical Q-bands appeared at around 675-700 nm and B-band of PcF appeared approximately at 345 nm. The increase in the concentration of phthalocyanine compounds causes aggregation that is easy to observe in the absorption spectra of Q-band. In the present study, PcF exhibited aggregation in THF at varying amounts of PcF due to the large molecular structure of 2(3), 9(10), 16(17), 23(24)–tetrakis 4-(4-(2-phenylprop-2-yl) phenoxy) phthalocyanine [32].

The UV/Vis spectroscopy procedure is widely applied to investigate the binding of chemical complexes by the DNA. Generally, the interaction of tiny biomolecules to CT-DNA pertains to the change in hyperchromicity, hypochromicity, blue shift or redshift in wavelength of electronic titration spectra [33]. The binding mode of intercalation is generally associated with hypochromicity and redshift [32]. Absorption titration is a very much helpful method in investigating the binding activities of phthalocyanines on the DNA molecules. The interaction of tetracationic zinc and phthalocyanine were reported in the literature [34]. The results of previous studies indicated that the quaternary Zn(II) and metal-free phthalocyanine compound interact with the DNA molecule [34, 35]. Another study on the morpholine zinc (II) phthalocyanine complex demonstrated that phthalocyanine complex binds to DNA molecule with intercalative mechanisms [36]. The findings of other studies showed that positively charged phthalocyanines interact with DNA by non-intercalation mode [37]. A study on Cu(II), Mn(III) and Zn(II) phthalocyanine complexes demonstrated that phthalocyanine complexes bind to the DNA molecule by an intercalative mechanisms [38]. Cu(II) bearing hexamethyleneimino-ethoxy phthalocyanine complex was also studied, and the finding showed that it has a strong interaction by DNA [34]. Additionally, the interactions of a cationic cobalt and palladium phthalocyanine complexes with the DNA were also reported. The results of the investigation demonstrated that the phthalocyanine complex interacts with the DNA molecule [39]. The absorption titrations of the 2(3), 9(10), 16(17), 23(24) –tetrakis4-(4-(2-phenylprop-2-yl)phenoxy) phthalocyanine compound at various concentrations of CT-DNA are displayed at Fig. 2. In the absence of CT-DNA, the electronic titration spectra of PcF (20 μM) was performed from 300 to 800 nm. PcF indicated two particular electronic spectra, which are at around 675 and 640 nm for Q-bands and approximately 340 nm for the B-band as shown in Fig. 2. The electronic titration experiment of the DNA binding activities with PcF compound was conducted in a Tris-HCl buffer at pH of 7.1 in the presence of the DNA. The absorption titration of PcF showed decreasing in absorbance intensities by increase in the concentrations of CT-DNA. The changing in the electronic titration spectra of PcF during titration by the DNA are indicated in Fig. 2. The results showed that PcF had hypochromicity with redshift as shown in Fig. 2. The hypochromicity that appeared proved that PcF binds to the DNA with intercalative mechanisms. It is accepted that redshift in absorption spectra is related to the decreasing of energy from HOMO to LUMO of the ring of phthalocyanine, but hypochromicity refers to the binding between chemical complexes and the bases of CT-DNA molecule [40-42]. The changing in hypochromicity indicates that PcF interacts by the DNA through the intercalation binding mechanisms. The results of this method proved that PcF compound binds to the DNA by intercalative binding. The additional, method described over, the Kb

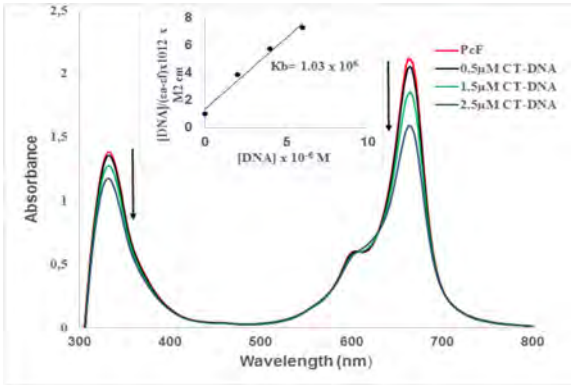

Figure 2. The electronic titration spectra of PcF (20 μM) in the buffer solution at a pH of 7.1 with increasing concentrations of the DNA. Arrows show absorption spectral shifting with increasing amounts of the DNA.

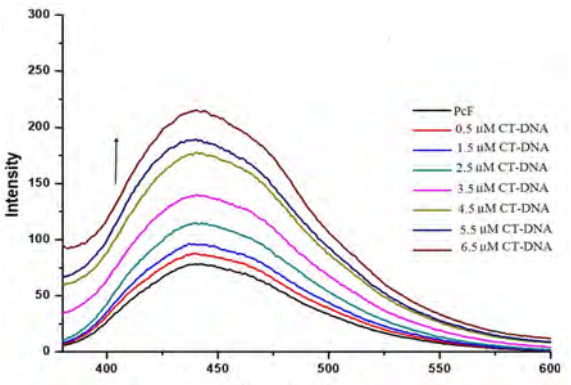

Figure 3. Fluorescence emission spectra of PcF compound in a Tris-HCl solution at a pH of 7.1. The arrow shows the increase in the intensity of fluorescence titration spectra with increasing amounts of DNA..

constant of PcF by the DNA was obtained by using the Wolfe-Shimer formula. The Kb was calculated as 1.03 × 106 M–1. The value demonstrated that PcF has a binding activity to the DNA by the intercalative binding[35].

Fluorescence spectra experiments

Fluorescence spectroscopic titration procedure is often applied to search the DNA interaction activities with chemical compounds. The emission titration technique provides a significant amount of understanding on the interaction among chemical compounds and the DNA molecule. Recently, in the literature, there have been several fluorescence titration studies that aimed to investigate the interaction between DNA and small chemical compounds [43]. In the present study, the emission titration experiments were conducted to study the interaction of PcF with CT-DNA in the buffer at a pH of 7.1. PcF generated fluorescence spectra with forming a peak around 445 nm in a Tris-HCl solution at a pH of 7.1 in the absence of the DNA as indicated in Fig. 3. In the buffer solution at a pH of 7.1, the fluorescence emission spectra of PcF were studied in the presence of the DNA as shown in Fig. 3. The arrow indicates the change in the intensities upon increase in concentrations of CT-DNA. When the amounts of CT-DNA was increased, the intensities of peaks of fluorescence emission gradually increased. This finding indicated that PcF interacts with CT-DNA by intercalation mechanism as the molecular structure of DNA was shifted with a chemical compound [44]. The increasing concentrations of DNA caused the increasing in the intensity of the emission spectra of PcF. This result specified that PcF has binding activities to CT-DNA.

Thermal denaturation profile experiments

A melting temperature (Tm) experiment was performed on the DNA samples for analyzing the binding properties of PcF. Thermal denaturation experiments of DNA produce a substantial amount of information about the activities of DNA based on the changes in temperature at a 260 nm wavelength [45]. The intercalation binding mechanism of biochemical complexes by DNA molecule enhances the thermal melting because of the impact of the interaction mode, but thermal melting temperatures of the non-intercalative binding mechanism for some chemical compounds with DNA either decrease or do not change [43]. The thermal melting temperature of the DNA was conducted by electronic spectra titration in the presence of a buffer at a pH of 7.1. The findings of melting temperature experiments were shown in Table 1. The temperature of the thermal denaturation of the DNA was observed to be 73.57 °C. In the presence of PcF, thermal denaturation temperature was observed as 81.64 °C. These findings demonstrated that PcF interacts with the DNA by intercalation mechanism because of the enhancement of melting temperature.

Table 1. Thermal denaturation temperatures (Tm) of CT-DNA in Tris-HCl at a pH of 7.1.

Sample	Melting temperature (Tm)
CT-DNA	73.57 °C
CT-DNA+ PcF	81.64 °C

The study of agarose gel electrophoresis

The Agarose gel electrophoresis method [46, 47] was utilized to investigate the interaction of phthalocyanine on CT-DNA in a Tris-HCl at a pH of 7.1 at 25 °C. The binding of PcF (20 μM) to CT-DNA (5, 15, 25 μM) was studied to verify the effect of CT-DNA on PcF (20 μM). Lane C represents the control DNA and lanes 1, 2 and 3 belong to the DNA and PcF mixtures. Lane M shows the DNA marker. Fig. 4 shows the DNA bands which were visualized under UV light. These findings clearly demonstrated that the band intensities of DNA significantly reduced when the concentrations of CT-DNA increased. There was a decline in the band intensities of CT-DNA after the interaction of PcF with CT-DNA because of the distortion of

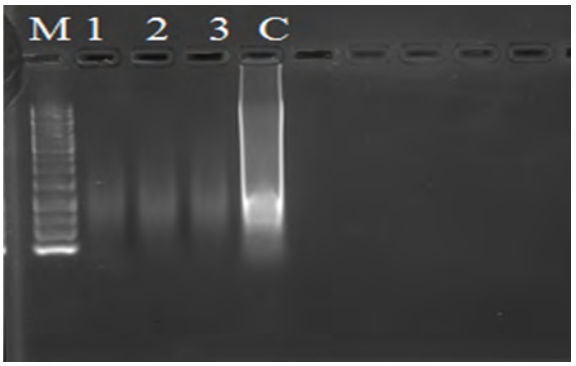

Figure 4. The CT-DNA bands of gel electrophoresis at a pH of 7.1 for PcF compound. The lane 1, 2 and 3 pertain to the DNA (5, 15, 25 μM) and PcF (20 μM), respectively. Lane C represents control CT-DNA, and lane M represents the DNA marker.

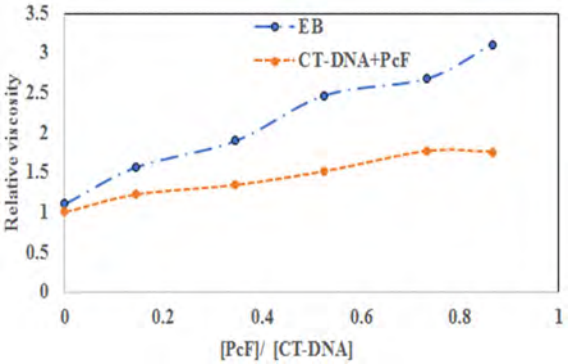

Figure 5. The viscosity of EB (Ethidium Bromide) (blue line) and the change in viscosity of CT-DNA and PcF compound (orange line).

the DNA's double helix [48, 49]. The results of this analysis verified that PcF interacted with the DNA molecule.

The change in intensities in CT-DNA bands appeared in lanes 1, 2 and 3 in the comparison of the DNA bands to the C DNA as shown in Fig. 4. When the interaction ability of PcF with the DNA was aligned with control DNA,

the findings showed that PcF had a strong interaction with CT-DNA. It was found that the control DNA showed no significant change. In a conclusion, the results of agarose gel electrophoresis study proved that PcF has a binding activity to CT-DNA.

Viscosity measurement experiments

The viscosity measurement procedure is widely applied to investigate the DNA binding characteristics of compounds based on increases and decreases in DNA viscosity based upon an increase in concentrations of chemical compounds. An increasing of viscosity indicates that chemical complexes bind to the DNA molecule with intercalative mechanisms that cause deformation and enlargement of the DNA. In contrast, a decrease in viscosity values demonstrates that the molecules interact by the DNA molecule through the non-intercalation mechanism.

The stacking of the ligands of compounds between DNA bases cause significant changes in the molecular structure of DNA [50, 51]. Viscosity measurements were performed to prove the binding activities of drug for treatment of DNA molecule for PcF compound at a constant pH of 7.1 as demonstrated in Fig. 5. Firstly, the relative viscosity measurements of ethidium bromide (EB) were carried out. Secondly, viscosity experiments of the DNA and PcF were performed in the presence of EB as given in Fig. 5. The increasing in the viscosity of CT-DNA was gradually enhanced when the concentration of PcF increased. The viscosity experiment demonstrated that PcF interacts with the DNA by partial intercalative binding.

CONCLUSION

In this study, the previously synthesised 2(3), 9(10), 16(17), 23(24)–tetrakis 4-(4-(2-phenylprop-2-yl) phenoxy) phthalocyanine compound was reported in the literature. The binding activities of the DNA for PcF compound were examined by electronic titration spectra, fluorescence spectra, thermal melting and the study of viscosity in the buffer at a pH of 7.1. The results of absorption spectra, fluorescence spectra, thermal melting and the study of viscosity methods verified that the compound binds to CT-DNA through an intercalative mechanism. In addition to above methods, the DNA interaction activities of PcF were also studied by the electrophoresis on calf thymus DNA. The result of the electrophoresis experiment showed that the compound binds to calf thymus DNA through an intercalative mechanism. These results suggested that PcF could be a potential therapeutic agent. Therefore, further studies are necessary to prove it as a therapeutic drug for the treatment of diseases such as cancer due to its DNA interaction characteristics.

ACKNOWLEDGEMENT

This scientific research was supported by Scientific Research Projects of Karabuk University and the Research Fund of Van Yüzüncü Yıl University (FYL-2016-5160). We special thank to Prof. Dr. Arif Baran and his research group members.

References

1. Mantareva V, Angelov I, Aliosman M, Stoineva I, Kussovski V. An overview on the impact of cationic phthalocyanine complexes for inactivation of drug-resistant microorganisms. Photodiagnosis Photodynamic Therapy 27 (2017) A43-A44.
2. Yazıcı A, Dalbul N, Altındal A, Salih B, Bekaroğlu Ö. Ethanol

sensing property of novel phthalocyanines substituted with 3,4-dihydroxy-3-cyclobuten-1,2-dione. Sensors Actuators B: Chemical 202 (2014)14-22.
3. Sevim MA, Ilgün C, Gül A. Preparation of heterogeneous phthalocyanine catalysts by cotton fabric dyeing. Dyes and Pigments 89 (2011)162-168.
4. Kantar C, Mavi V, Baltas N, Islamoğlu F, Şaşmaz S. Novel zinc(II)phthalocyanines bearing azo-containing schiff base: Determination of pKa values, absorption, emission, enzyme inhibition and photochemical properties. Journal of Molecular Structure 1122 (2016) 88-99.
5. Kantar GK, Kantar N, Baltaş N, Menteşe E, Şaşmaz S. Microwave-assisted synthesis and investigation of xanthine oxidase inhibition of new phthalonitrile and phthalocyanines containing morpholino substituted 1,2,4-triazole-3-one. Journal of Organometallic Chemistry 787 (2015) 8-13.
6. Siegel RL, Miller KD, Jemal A. Cancer statistics. CA: A Cancer Journal For Clinicians 65 (2015) 5-29.
7. Bagda E, Yabaş E, Bagda E. Analytical approaches for clarification of DNA-double decker phthalocyanine binding mechanism: As an alternative anticancer chemotherapeutic. Spectrochimica Acta Part A: Molecular and Biomolecular Spectroscopy 172 (2017) 199-204.
8. Oliveira LT, Garcia GM, Kano EK, Tedesco AC, Mosqueira VCF. HPLC-FLD methods to quantify chloroaluminum phthalocyanine in nanoparticles, plasma and tissue: application in pharmacokinetic and biodistribution studies. Journal of Pharmaceutical Biomedical Analysis 56 (2011)70-77.
9. Palchaudhuri R, Hergenrothe PJ. DNA as a target for anticancer compounds: methods to determine the mode of binding and the mechanism of action. Current Opinion in Biotechnology 18 (2007) 497-503.
10. Rescifina A, Zagni C, Varrica MG, Pistara V, Corsaro A. Recent advances in small organic molecules as DNA intercalating agents: Synthesis, activity, and modeling. European Journal of Medicinal Chemistry 74 (2014) 95-115.
11. Ozluer C, Satana Kara HE. In vitro DNA binding studies of anticancer drug idarubicin using spectroscopic techniques. Journal of Photochemistry and Photobiolology B: Biology 138 (2014) 36-42.
12. Williams AK, Dasilya SC, Bhatta A, Rawal B, Liu M, Korobkova EA. Determination of the drug–DNA binding modes using fluorescence-based assays. Analytical Biochemistry 411 (2012) 66-73.
13. Uslan C, Sesalan BŞ. The synthesis, photochemical and biological properties of new silicon phthalocyanines. Inorganica Chimica Acta 94 (2013) 353-362.
14. Aboraia AS, Abdel-Rahman HM, Mahfouz NM, El-Gendy MA. Novel 5-(2-droxyphenyl)-3-substituted-2,3-dihydro-1,3,4-oxadiazole-2-thione derivative Promising anticancer agents. Bioorganic and Medicinal Chemistry 14 (2006) 1236-1246.
15. Şahin G, Palaska E, Ekizoğlu M, Özalp M. Synthesis and antimicrobial activity of some 1,3,4-oxadiazole derivatives. II. Farmaco 57 (2002) 539-542.
16. Durmuş C, Master Thesis, Synthesis and Investıgatıon of Some Properties of 4-(4-(2-Phenylpropan-2-yl)phenoxy) Substituted phthalocyanines. Yüzüncü Yıl University (2017).
17. Demirbaş Ü, Barut B, Özel A, Çelik F, Kantekin H, Sancak K. Synthesis, characterization and DNA interaction properties of the novel peripherally tetra 4-(3-methyl-4-(3-morpholinopropyl)-5-oxo-4,5-dihydro-1H-1,2,4-triazol-1-yl) substituted water soluble Zn(II) and Cu(II) phthalocyanines. Journal of Molecular Structure 1177 (2002) 571-578.
18. Saha U, Mukherja K. DNA binding and nuclease activity of an oxovanadium valinato-Schiff base complex. International Journal of Biologycal Macromolecules 66 (2014)166-171.
19. Fu XB, Wang GT, Liu DD, Lie XY. Synthesis, characterization, DNA binding and cleavage, HSA interaction and cytotoxicity of a new copper(II) complex derived from 2-(2'-pyridyl)benzothiazole and glycylglycine. Journal of Photochemistry and Photobiolology A: Chemistry 276 (2014) 83-95.
20. Wolfe A, Shimer GH, Meehan T. Polycyclic aromatic hydrocarbons physically intercalate into duplex regions of denatured DNA. Biochemistry 26 (1987) 6392-6396.
21. Barut B, Demirbaş Ü, Özel A, Kantekin H. Novel water soluble morpholine substituted Zn(II) phthalocyanine: Synthesis, characterization, DNA/BSA binding, DNA photocleavage and topoisomerase I inhibition. International Journal of Biologycal Macromolecules 105 (2017) 499-508.
22. Azza AS, Mohamed MS. DNA binding, spectrocopic and antimicrobial studies of palladium (II) complexes containin 2,2o-bipyridin and 1-phenypiperazine. Spectrochimica Acta Part A: Molecular and Biomolecular Spectroscopy 96 (2012) 586-593.
23. Apilux A, Tabata O, Chailapakul M. Electrochemical bihaviors of native and thermal denatured fish DNA in the presence of cytosine derivatives and porphyrin by cyclic vol-tammetry using boron-drobed diamond electrode. Bioelectrochemistry 70 (2007) 435-439.
24. Arslantas A, Agirtas MS. A Comparative Study on DNA Binding Properties of 2,10,16,24-Tetrakis 4-(4-hydroxyphenyl)-1-phenylethyl) phenoxy)-Substituted Co(II) and Mg(II) Phthalocyanine Compounds. ChemistrySelect 2 (2017) 8661-8665.
25. Agirtas MS, Cabir B, Ozdemir S, Okumus V, Arslantas A. Synthesis, Aggregation, Antioxidant and DNA-Binding Properties of Metallophthalocyanines Bearing 5-Tert-butyl-2-hydroxyphenoxy Groups. ChemistrySelect 2 (2017) 11352-11357.
26. Demirezen N, Tarınc D, Polat D, Cesme M, Golcu A, Tumer M, Synthesis of trimethoprim metal complexes: Spectral, electrochemical, thermal, DNA-binding and surface morphology studies. Spectrochimica Acta Part A: Molecular and Biomolecular Spectroscopy 94 (2012) 243-255.
27. Arslantas A, Agirtas MS. Investigation of DNA-Binding Activities of Zinc(II) and Cobalt(II) Phthalocyanine Compounds with 3,4,5-Trimethoxybenzyloxy Substituents. ChemistrySelect 2 (2017) 11659-11665.
28. Reddy PR, Shilpa A, Raju N, Raghavaiah P. Synthesis, structure, DNA binding and cleavage properties of ternaryamino acid Schiff base-phen/bipy C(II) complexes. Journal of Inorgoanic Biochemistry 105 (2011) 1603-1612.
29. Arslantas A, Agirtas MS. Studies on DNA Interaction with 2(3),9(10), 16(17), 23(24)-Tetrakis 2((4-Phenoxyphenyl) Diazeylbenzoic acid) phthalocyaninato Zinc (II) Compound. ChemistrySelect 3 (2018) 1755-1760.
30. Liu XW, Shen YM, Li ZX, Zhong X, Chen YD, Zhang SB. Study on DNA binding behavior and light switch effect of new coumarin-derived Ru (II) complexes. Spectrochimica Acta Part A: Molecular and Biomolecular Spectroscopy 49 (2015) 150-156.
31. Arslantas A, Agirtas MS. Investigation of DNA Binding Activities of Peripherally 2,10,16,24-Tetrakis Dimethyl 5-(Phenoxy)-Isophthalate-Substituted Ni(II) Phthalocyanine Complex. ChemistrySelect 3 (2018) 3155-3160.
32. Özçeşmeci M, Sorar I, Hamuryudan E. Synthesis, optical and structural studies of tetrakis[4-(2',3',4',5',6'-pentafluorobenzyloxy) benzyloxy]-substituted metallo-phthalocyanines. Synthetic Metals 162 (2012) 154-161.
33. Barut B, Demirbaş Ü, Şenocak A, Özel A, Kantekin H. Water soluble axially morpholine disubstituted silicon phthalocyanines:

Synthesis, characterisation, DNA/BSA binding, DNA photocleavage properties. Synthetic Metals 229 (2017) 22-32.
34. Evren D, Kalkan A, Özçeşmeci Bİ, Sesalan BŞ. Synthesis of novel tetracationic phthalocyanines and investigation of their DNA-binding properties. Dyes and Pigments 96 (2013) 475-482.
35. Çakır V, Çakır D, Göksel M, Durmuş M, Bıyıklıoğlu Z, Kantekin H. Synthesis, photochemical, bovine serum albumin and DNA binding properties of tetrasubstituted zinc phthalocyanines and their water soluble derivatives. Journal of Photochemistry and Photobiolology A: Chemistry 299 (2015) 138-151.
36. Lopez Zeballos NC, Gauna GA, Garcia Vior MC, Awruch J, Dicelio LE. Interaction of cationic phthalocyanines with DNA and importance of the structure of the substituents. Journal of Photochemistry and Photobiolology B: Biology 136 (2014) 29-33.
37. Barut B, Sofuoglu A, Biyiklioglu Z, Özel A. The water soluble peripherally tetra-substituted zinc(II), manganese(III) and copper(II) phthalocyanines as new potential anticancer agents. Dalton Transactions 45 (2016) 14301-14310.
38. Uslan C, Sesalan BS. Synthesis of novel DNA-interacting phthalocyanines. Dyes and Pigments 94 (2012) 127-135.
39. Turanlı-Yıldız B, Sezgin T, Petek Çakar Z, Uslan C, Sesalan BŞ, Gül A. The use of novel photobleachable phthalocyanines to image DNA. Synthetic Metals 161 (2011) 1720-1724.
40. Bıyıklıoğlu Z, Barut B, Özel A. Synthesis, DNA/BSA binding and DNA photocleavage properties of water soluble BODIPY dyes. Dyes and Pigments 148 (2018) 417-428.
41. Smolkova R, Zelenak V, Gyepes R, Sabolova D, Imrichova N, Hudecova D, Smolko L. Synthesis, characterization, DNA binding, topoisomerase I inhibition and antimicrobial activity of four novel zinc(II) fenamates. Polyhedron 141 (2018) 230-238.
42. Baş H, Barut B, Biyiklioglu Z, Özel A. Synthesis, DNA interaction, topoisomerase I, II inhibitor and cytotoxic effects of water soluble silicon (IV) phthalocyanine and phthalocyanine bearing 1-acetylpiperazine units. Dyes and Pigments 160 (2019) 136-144.
43. Zhang SS, Niu SY, Qu B, Jie GB, Xu H, Ding CF. Studies on the interaction mechanism between hexakis(imidazole) manganese (II) terephthalate and DNA and preparation of DNA electrochemical sensor. Journal of Inorgoanic Biochemistry 99 (2005) 2340-2347.
44. Özen F, Günel A, Baran A. DNA-binding, enzyme inhibition, and photochemical properties of chalcone-containing metallophthalocyanine compounds. Bioorganic Chemistry 81 (2018) 71-78.
45. Keleş T, Barut B, Biyiklioglu Z, Özel A. A comparative study on DNA/BSA binding, DNA pA comparative study on DNA/BSA binding, DNA photocleavage and antioxidant activities of water soluble peripherally and non-peripherally tetra-3-pyridin-3-ylpropoxy-substituted Mn(II), Cu (II). Dyes and Pigments 139 (2017) 575-586.
46. Song Y, Yang P, Yang M, Kang J, Qin S, Lü B, Wang L. Spectroscopic and voltammetric studies of the cobalt (II) complex of Morin bound to calf thymus DNA. Transition Metal Chemistry 28 (2003) 712-721.
47. Pravin P, Utthra PP, Kumaravel G, Raman N. Effective DNA binding and cleavage tendencies of malonic acid coupled transition metal complexes. Journal of Molecular Structure 1123 (2016) 162-170.
48. Hassani L, Hakimian F, Safaei E, Fazzeli Z. Antibacterial effect of cationic porphyrazines and anionic phthalocyanine and their interaction with plasmid DNA. Journal of Molecular Structure 1052 (2013) 221-227.
49. Özçesmeci M, Ecevit ÖB, Sürgün S, Hamuryudan E. Tetracationic fluorinated inc(ii)phthalocyanine: Synthesis, characterization and DNA-binding properties. Dyes and Pigments 96 (2013) 52-58.
50. Al-Mogren MM, Alaghaz MA, Ebrahem EA. Synthesis, spectroscopic, molecular orbital calculation, cytotoxic, molecular docking of DNA binding and DNA cleavage studies of of transition metal complexes with N-benzylidene–N′-salicylidene-1,1-diaminopropane. Journal of Photochemistry and Photobiolology A: Chemistry 114 (2013) 695-707.
51. Shankaraiah N, Jadala C, Nekkati S, Senwar KR, Nagesh N, Shrivastaya S, Naidu VGM, Sathish M, Kamal A. Design and synthesis of C3-tethered 1,2,3-triazolo-β-carboline derivatives: Anticancer activity, DNA-binding ability, viscosity and molecular modeling studies. Bioorganic Chemistry 64 (2016) 42-50.

Hittite Journal of Science and Engineering, 2020, 7 (2) 89-97
ISSN NUMBER: 2148-4171
DOI: 10.17350/HJSE19030000177

Gold Nanoparticles/Graphene Oxide Based Disposable Sensor System for Voltammetric Detection of Ceftizoxime

Gulcin Bolat[1] Yesim Tugce Yaman[1,2] Ceren Yardimci[3] and Serdar Abaci[1,2]
[1]Hacettepe University, Department of Chemistry, Ankara, Turkey
[2]Hacettepe University, Advanced Technologies Application and Research Center, Ankara, Turkey
[3]Hacettepe University, Department of Analytical Chemistry, Ankara, Turkey

ABSTRACT

In this study, gold nanoparticles (AuNPs) were deposited onto graphene oxide (GO) modified pencil graphite electrode (PGE) in order to construct a disposable sensor platform for the electrochemical detection of ceftizoxime (CFX). Initially, electrode surface was covered with GO by physical adsorption and then AuNPs were deposited on the surface by electro-deposition method. Morphological feature of the developed sensor was investigated by scanning electron microscope. The parameters effecting the experimental conditions such as adsorption time of graphene oxide, deposition time of gold nanoparticles, supporting electrolyte pH, pre-concentrating potential/time were optimized. Under optimum experimental conditions, good linearity was obtained for CFX response in the range between 0.02-2.0 µM of CFX concentrations with a low detection limit (0.442 nM) by stripping voltammetry. The AuNPs/GO modified PGE was implemented to pharmaceutical samples with good recovery values. This study results proved that developed disposable sensor is a good alternative for the practical application of CFX analysis.

Article History:
Received: 2019/10/30
Accepted: 2020/05/01
Online: 2020/06/26

***Correspondence to**: Serdar Abaci, Hacettepe University, Department of Chemistry, Ankara, Turkey*
E-Mail: sabaci@hacettepe.edu.tr
Phone: +90 (312) 297 6080
Fax: +90 (312) 299 2163

Keywords:
Gold nanoparticles; Graphene oxide; Cephalosporins; Ceftizoxime; Anodic stripping voltammetry.

INTRODUCTION

Cephalosporins are β-lactam antibiotics which their main core is formed by cephem derivative of 7-amino-cephalosporanic acid [1]. Due to their similar antimicrobial indications with penicillin's, this group of antibiotics are widely used in treatment for penicillin resistive bacteria. Further, they have been prescribed safely for penicillin allergic patients. Cephalosporins show bactericide effect against various microbial organisms-bacteria and they have been classified into generations depending on their spectrum of activity. Specifically, ceftizoxime sodium (CFX), belonging to third generation of semi-synthetic cephalosporins, has broad-spectrum resistance against β-lactamases [2] (Fig. 1). The most important features of third-generation cephalosporins (except Cefoperazone) includes the increased efficiency to gram-negative bacteria, high stability against hydrolysis by β-lactamases and in particular, being free of serious side effects in patients. Furthermore, some of them are known to overcome the blood-brain barrier [3]. CFX shows high antibacterial effect against a broad range of gram positive and negative bacteria such as *Staphylococcus pneumoniae, Haemophilusinfluenzae, Escherichia coli*, and *Neisseria gonorrhoeae* by penetrating into bacterial cell wall and consequently leading to effective destruction of bacteria [4]. CFX, with a relatively long elimination half-life (3-4 h), is administered through the oral route for the treatment of moderate bacterial infections [5]. It is active against putrefaction and clinically effective in eradicating bacteria causing urinary tract infections, acute pharyngitis, otitis media, tonsillitis, gonorrhea and pneumonia [3]. Given it's pharmacological significance and extended use, quantitative analysis of CFX in biological fluids has great clinical value in order to reveal biochemical processes that occur in the drug metabolism and also in pharmaceutical formulations to assure drug quality.

Up to now, analysis of CFX in various matrixes, such as human and animals, biological materials, food, waters and pharmaceuticals have been studied by several chromatographic and spectrometric methods [6–10]. Although they provide very efficient analyses for the sensitive detection of CFX, these methods have some handicaps such as high cost instrumentation, long

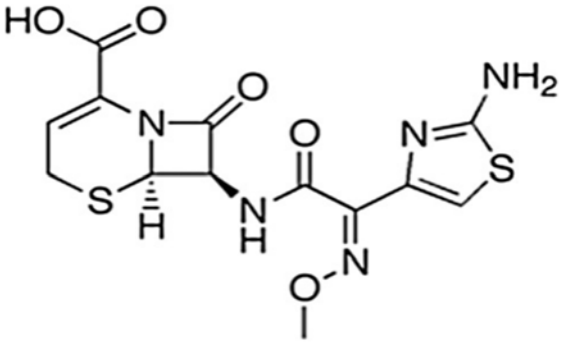

Figure 1. Chemical structure of Ceftizoxime.

analysis time, including the need for specialized staff. Since CFX is an electroactive molecule, electrochemistry is a promising approach for the analysis of CFX due to its benefits such as being simple, sensitive, fast and requiring portable and low-cost systems as well as being suitable for on-site detection. Up to now, only a few studies on the oxidation behavior and detection of CFX have been reported based on different electrochemical methodologies using solid electrodes. Jain et al., offered a fullerene based glassy carbon electrode (GCE) for the reduction of CFX in solubilized system and applied for the pharmaceutical tablet samples [11]. In another study, silver nanoparticle with nano graphite-diamond modified GCE was developed to determine the CFX in blood serum and commercial pharmaceutical tablet [12]. Nickel particle decorated on Poly(o-anisidine) sensor platform was constructed to detect CFX by Ojani et al. [13]. On the other hand, single-use sensor technologies offer some considerable advantages to design sensor platforms. Specifically, pencil graphite electrode (PGE), as a carbon based electrode, have extensively been applied in electroanalysis due to its benefits such as commercial availability, good electrochemical reactivity and mechanical resistance, feasibility for modification, as well as enabling disposable manipulation which eliminates the need for electrode surface cleaning steps [14]. Functionalization of the electrode surfaces with nanomaterials is crucial in order to significantly improve the electrochemical response. Standing out as an advanced material, graphene is a suitable nanomaterial for the electrochemical analysis due to its high electrical conductivity, high surface area, low cost and biocompatibility [15]. Graphene oxide (GO) is a valuable derivative of graphene which contains oxygen functional groups as distinct from the graphene [16]. Due to the outstanding features of GO, it has been extensively employed for the electrochemical determination of different analytes such as heavy metals [17], pathogens [18], pollutants [19] and drugs [20] etc. Metal nanoparticles have been used as a functional nanomaterial for the modification of electrochemical sensor surfaces. Especially, gold nanoparticle (AuNP) modified sensors are remarkably important surfaces owing to their excellent conductivity, high surface area and biocompatible properties [21]. To obtain highly electro-catalytic surfaces, AuNP's combined with other nanomaterials have widely been used in various analyses and catalysis [22–25] applications.

Hence, in the present study, AuNPs combined with GO modified PGE was constructed for the stripping analysis of CFX. AuNP/GO modified PGE was considered as an attractive platform from the stand point of easy use, cheapness and simple modification. Owing to considerable synergy between the AuNP and GO, anodic oxidation signal of CFX increased remarkably. The electrode surfaces were examined microscopically to prove the success of the modification. The experimental parameters such as adsorption time of graphene oxide, deposition time of gold nanoparticles, supporting electrolyte pH, pre-concentrating potential and time were optimized. Anodic stripping voltammetry (SWASV) measurements of CFX demonstrated good linear response with a low limit of detection (LOD) as 0.442 nM. The practical use of the sensor system was tested for commercial pharmaceutical tablets by standard addition method. The proposed sensor system has offered a low detection limit with respect to other studies in literature and also other parameters were comparable with the literature data.

MATERIAL AND METHODS

Reagents and Materials

Ceftizoxime sodium, gold (III) chloride trihydrate and graphene oxide (GO) were provided from Sigma Aldrich and Nanograf, respectively. 0.5 M of $HAuClO_4$ was prepared in 0.5 M of H_2SO_4. Britton-Robinson (B-R) buffer solution (0.04 M) was prepared by mixture of boric acid, acetic acid and phosphoric acid which was applied as a supporting electrolyte. Stock solution of CFX (10^{-2} M) was prepared in double distilled water and stored at +4 °C. More diluted solutions were prepared daily.

Instruments

CV, EIS and SWASV were recorded by Gamry interface 1000 model potentiostat/galvanostat. AuNP/GO modified PGE served as a working electrode. Pencil leads were purchased from local store in Turkey (0.5 mm diameter, Tombow). An Ag/AgCl (3M KCl) electrode was used as the reference and a platinum wire as the counter electrode. The surface morphology of the developed sensor was characterized by Zeiss Evo 60 EP-SEM. Besides, the AuNP/GO modified graphite surfaces were characterized by Energy-dispersive X-ray spectroscopy (EDX, Tescan/Czech Republic).

Fabrication of AuNP/GO/PGE sensor

Firstly, 1 cm of pencil leads were immersed in graphene oxide (GO) solution for 30 minutes. Afterwards, the leads were soaked in double distilled water for 5 seconds to remove the excess of GO attached on the surface. The GO modified electrodes were allowed to dry for 5 min at room temperature. Potential controlled electrolysis was used at - 0.3 V (vs. Ag/AgCl) for the electro-deposition of AuNPs on GO/PGE in 0.5 M $HAuClO_4$ solution (in 0.5 M H_2SO_4). The optimum electro-deposition time was found as 100 seconds.

Preparation of Drug Samples

Five tablets of Cefizox® (400 mg CFX per tablet) were weighed and pulverized in a mortar. Then, an average of 1 tablet weight was taken from this powder and dissolved in 100 mL double distilled water by ultrasonication for 1 hour. Upon centrifugation at 5000 rpm for 5 min, the supernatant was diluted in double distilled water.

Analytical Procedure

Electrochemical characterizations were performed by CV (between -0.2 V and 0.6 V (vs. Ag/AgCl)) and EIS (in the frequency range of 0.01–100,000 Hz) in redox probe solution (0.5 mM $Fe(CN)_6^{3-/4-}$ prepared in 0.1 M KCl). The electrochemical determination of CFX was carried out in 10.0 mL cell and BR buffer (pH 2.5 as optimum pH) was used as the supporting electrolyte by CV at potential from 0.7 V to 1.1 V (vs. Ag/AgCl). Square wave anodic stripping voltammetry (SWASV) was recorded from 0.6 V to 1.0 V (vs. Ag/AgCl) after a pre-concentrating step of 300 seconds at 0.6 V (vs. Ag/AgCl) accumulation and deposition time, respectively. After this pre-concentration step, stirring was stopped and 15s was waited as a release time. The pulse amplitude 4 mV, pulse size 50 mV and frequency 50 Hz were used as parameters of SWASV. Before the all electrochemical measurements, supporting electrolyte was purged with the nitrogen gas for 5 minutes.

RESULTS AND DISCUSSION

Morphology and Electrochemical Characterization of AuNP/GO modified PGE

In order to reveal the gradual changes on the electrode after the modifications, surface morphology of bare and modified pencil graphite electrodes (PGEs) were investigated with scanning electron microscopy (SEM). Fig. 2.a showed that bare PGE surface displayed irregular graphite layers with highly rough structure, as expected. When graphene oxide (GO) was deposited onto PGE surface, it was observed that single or few-layers of GO nano-sheets with high amount of wrinkles due to GO sheets were entangled with each other (Fig. 2.b). The nanosized AuNPs which were deposited by potential control electrolysis, were in a form of spherical structure uniformly distributed over the bare electrode surface and over the GO layers, respectively (Fig. 2.c,d). The morphology of the AuNP/GO modified PGE showed more even structure.

As it was shown in Fig. 2.g-h, the main elements of GO including carbon, and oxygen were all observed in EDX spectrum as expected [26]. Also, the presence of gold which resulted from the AuNPs on the surface of GO/PGE was confirmed with EDX analysis (Fig. 2.h). The carbon and oxygen peaks were observed on the bare graphite surface in Fig. 2.e-f. These results clearly suggested that AuNP/GO were successfully coated on the graphite surface.

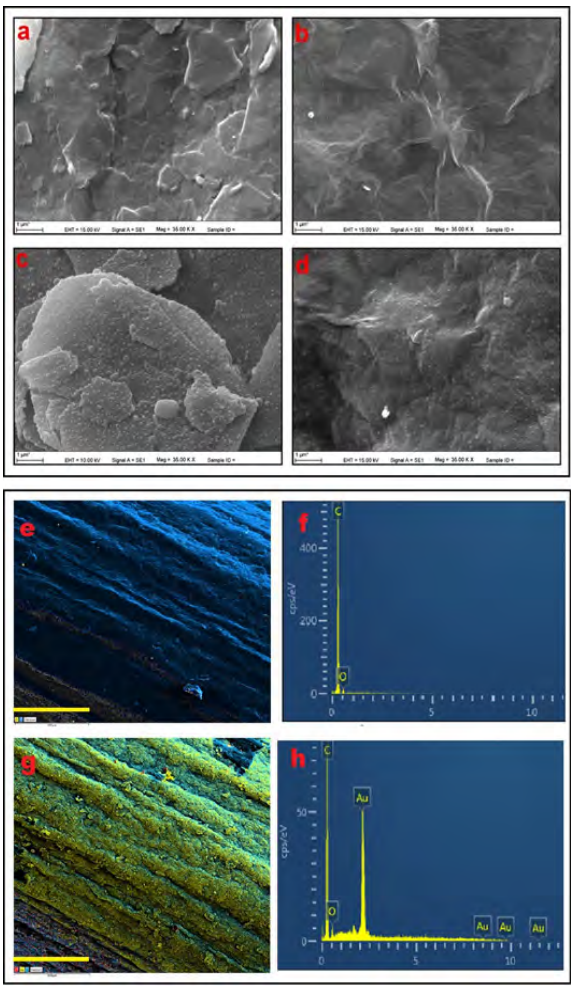

Figure 2. The scanning electron micrographs of **a)** Bare PGE, **b)** GO modified PGE, **c)** AuNP modified PGE, **d)** AuNP/GO modified PGE (Scale bar: 1 µm). EDX mapping of **e)** PGE (The colors: Blue:C; Yellow:O) and **g)** AuNP/GO/PGE (scale bar: 100 µm. The colors: Red:O; Blue:C; Yellow: Au) and corresponding elementel compositions of **f)** PGE and **h)** AuNP/GO/PGE.

Table 1. Anodic/cathodic peak currents (Ipa/Ipc) and peak potentials (Epa/Epc) at bare, GO modified and AuNP/GO modified PGEs.

Electrode	Ipa (μA)	Ipc (μA)	Epa (V)	Epc (V)	ΔEp (V)
PGE	336.0	323.0	0.306	0.173	0.133
GO/PGE	288.2	268.8	0.343	0.166	0.177
AuNP/GO/ PGE	461.7	468.6	0.292	0.175	0.117

To investigate the electrochemical behaviour of developed disposable nanosensor platform, cyclic voltammetry and impedance spectroscopy were employed in redox probe solution. Fig. 3.A depicts the decrease in anodic/cathodic peak currents of redox pairs at GO/PGE compared to bare PGE (Fig. 3.A.b and 2.A.a, respectively). Besides, peak-to-peak separation increased due to the negatively charged carboxyl groups of GO. When the medium pH is high enough, carboxyl groups in the GO structure are negatively charged and repel the negatively charged $Fe(CN)_6^{3-/4-}$ redox pair from the surface with electrostatic effects. Hence, the presence of GO on PGE impeded the electron transfer and reduced the peak currents [27]. When AuNP electrodeposition was performed onto GO film, AuNP/GO/PGE showed a well-defined CV, with approximately equal and reversible peaks (Fig. 3.A.c). The highest peak current values indicated a faster electron-transfer than the GO modified PGE. This was realized by the catalytic effect of AuNPs and increased

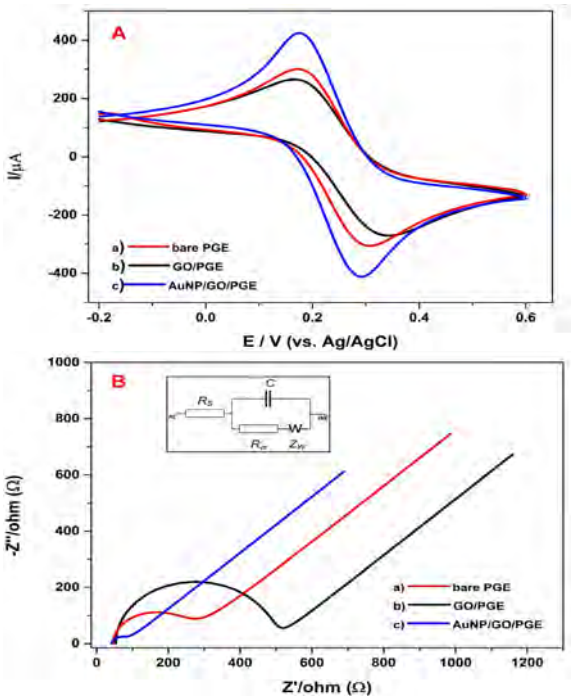

Figure 3. a) CVs showing a) bare, b) GO/PGE and c) AuNP/GO/PGE in 5 mM $Fe(CN)_6^{3-/4-}$ /0.1 M KCl at 50 mVs^{-1}. B) Nyquist diagrams of a) bare, b) GO/PGE and c) AuNP/GO/PGE in 5 mM $Fe(CN)_6^{3-/4-}$ /0.1 M KCl. (E: 0.2 V, Frequency: 100000-0.1 Hz). Inset: equivalent circuit for EIS spectrum. Rs: the electrolyte resistance, Cdl: double-layer capacitance, Rct: the electron transfer resistance, Zw: the Warburg impedance.

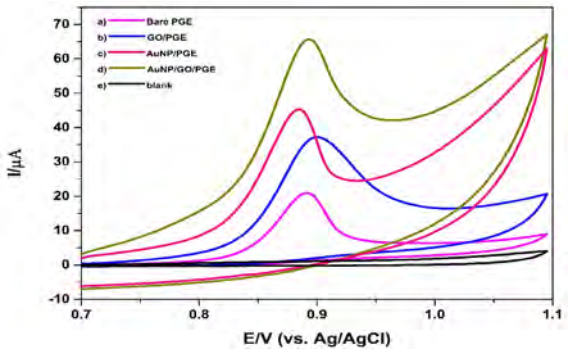

Figure 4. CVs for 50 μM of CFX in pH 3.0 B-R buffer solution at a) bare, b) GO modified, c) AuNP modified, d) AuNP/GO modified PGE. e) CV for AuNP/GO/PGE in the absence of CFX. (Scan rate: 100 mVs^{-1} vs. Ag/AgCl).

electrode surface area, accordingly. The corresponding results were summarized in Table 1.

To support this behavior of AuNP/GO/PGE, EIS method was utilized and obtained Nyquist diagrams were presented in Fig. 3.B. The charge transfer resistance (Rct) values were calculated from the obtained spectrum using Randles circuit at the electrode/solution interface (Fig. 3.B inset). The Rct values of bare and GO/PGE were calculated as 260 Ω and 440 Ω, respectively. The increased Rct can be explained by the restriction of electron transfer due to GO modification. The resistance of AuNP/GO modified electrode at the electrode/solution interface decreased, due to increased charge transfer, so, AuNP/GO/PGE had the lowest Rct (43 Ω) as expected. These results proved that modification of PGE surface was performed successfully.

The influence of modification of PGE on the electrochemical behavior CFX

The voltammetric response of CFX was examined at bare and modified surfaces (Fig. 4). All the CVs revealed an oxidation peak at about 0.9 V (vs. Ag/AgCl) and no reduction signal was recorded in the reverse scan due to irreversible nature of the electrode process for cephalosporins [28].

As previously reported, the oxidation of amino group at aminothiazole substituent to imino radical was responsible for the electrode process of this group of antibiotics [12] (Fig. 5).

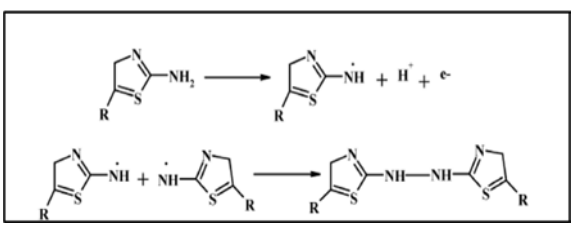

Figure 5. Electrochemical oxidation reactions of CFX.

As previously reported, the oxidation of amino group at aminothiazole substituent to imino radical was responsible for the electrode process of this group of antibiotics [12] (Fig. 5).

The recorded CVs for 50 µM of CFX in pH 3.0 B-R buffer showed that maximum peak current intensity was provided by GO/AuNP/PGE surface. The oxidation peak current was 3.5 times higher and the peak potential appeared at more negative potentials with respect to bare PGE. This can be ascribed to larger effective surface area and improved catalytic activity of the modified sensor surface. Thus, it was concluded that AuNP/GO modified PGE sensor system was suitable for sensitive CFX detection. In order to understand the effect of several experimental parameters, optimization studies were performed as below.

Effect of Scan Rate

The effect of scan rate was examined in the range of 10-400 mVs^{-1} at AuNP/GO/PGE (Fig. 6). The plot of oxidation peak current vs square root of scan rate showed excellent linearity. This linearity was given as follows (Eq1.)

$$I(\mu A) = 5.085\vartheta^{0.5} + 12.28 \qquad R^2 = 0.990 \qquad (1)$$

This behavior demonstrated that the electro-oxidation reaction of CFX was a typical diffusion controlled electrocatalytic process at AuNP/GO/PGE [11].

Effect of Electrolyte pH

The voltammetric behavior of CFX on the sensor was studied in BR buffer solutions of different pH values since the electrochemical characteristics is strongly dependent on the pH of the medium. Highest peak current was observed with the pH value of 2.5 and decreased up to pH value of 5.0 (Fig. 7). Thus, optimum pH value was determined as 2.5.

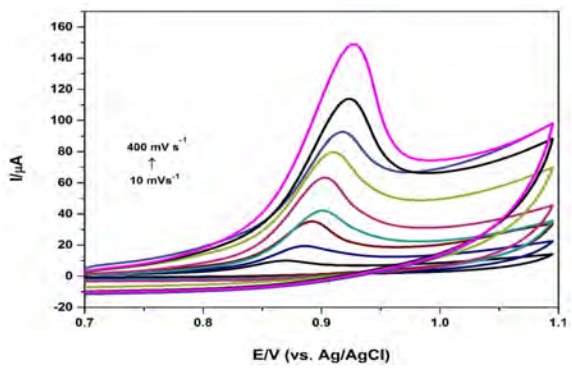

Figure 6. Scan rates from bottom to top: 10-400 mVs^{-1} for 50 µM CFX in pH 2.5 B-R Buffer.

Effect of AuNP and GO deposition time

After it was clearly demonstrated that the anodic oxidation of CFX increased when the modifying agents were combined together, AuNP/GO/PGE was employed in order to obtain improved electrochemical signal of the analyte. The dependence of response enhancement on GO and AuNP deposition time was examined. The physical adsorption time of GO was investigated between 15-90 minutes and the maximum oxidation peak current was obtained at 30 min (Fig. 8.a). After this adsorption time, peak current decreased which might have been due to electron transfer restriction with the increase of GO layer thickness. So, the optimum adsorption time of GO was used as 30 min.

After determining the optimization of physical adsorption time of GO, the bulk electrolysis time of AuNP onto GO/PGE was studied in the range of 25-300 s as deposition times (Fig. 8.b). The maximum peak current was obtained with deposition time of 100 s which promoted the electron transfer between the CFX and the electrode, and higher deposition times induced hinderance of the transfer. Therefore, 100 s of AuNP electrodeposition time was applied for further studies.

Effect of Pre-concentration Step

The pre-concentration of stripping analysis has two main steps; namely deposition potential and deposition time of the analyte. The deposition potential was changed at fixed concentration of CFX in the range of 0.0 to 0.7 V (vs. Ag/AgCl) at AuNP/GO modified PGE and stripping voltammograms were recorded. As shown in Fig. 9.a, according to the plot for applied deposition potential vs. the oxidation current of CFX, the measured peak current increased from 0.0 V to 0.6 V (vs. Ag/AgCl), and a roll-off rate was observed on the peak current after this value indicating that at more cathodic potentials which are close to oxidation potential of the analyte, CFX molecules are

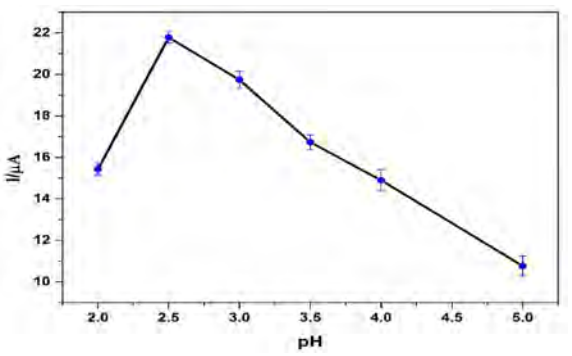

Figure 7. The current response of 5 µM CFX at AuNP/GO modified PGE at different pH (2.0, 2.5, 3.0, 3.5, 4.0, 5.0) BR buffer. Conditions: frequency: 15 Hz; step amplitude: 30 mV; pulse amplitude: 4 mV; $E_{deposition}$(E_{dep}): 0.5 V; tdeposititon (t_{dep}): 30 s.

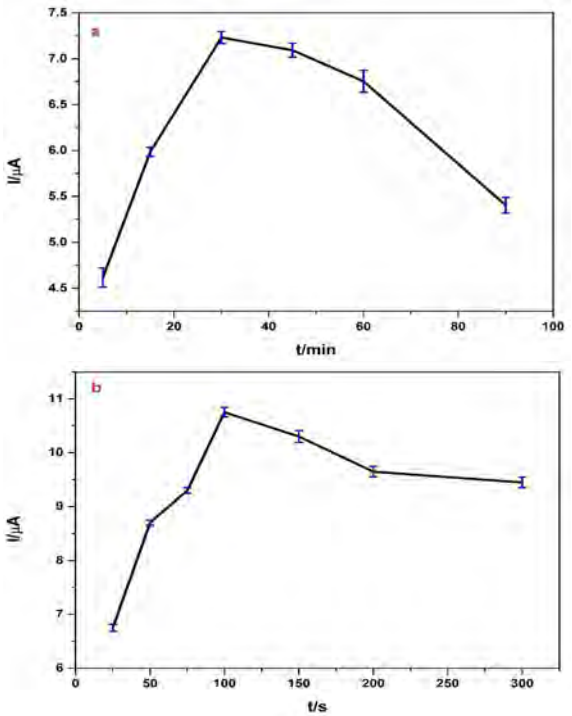

Figure 8. a) Effect of GO adsorption time onto PGE, b) Effect of electrodeposition time of AuNP to electrochemical response of 5 μM CFX. (Under the same SWASV experimental conditions).

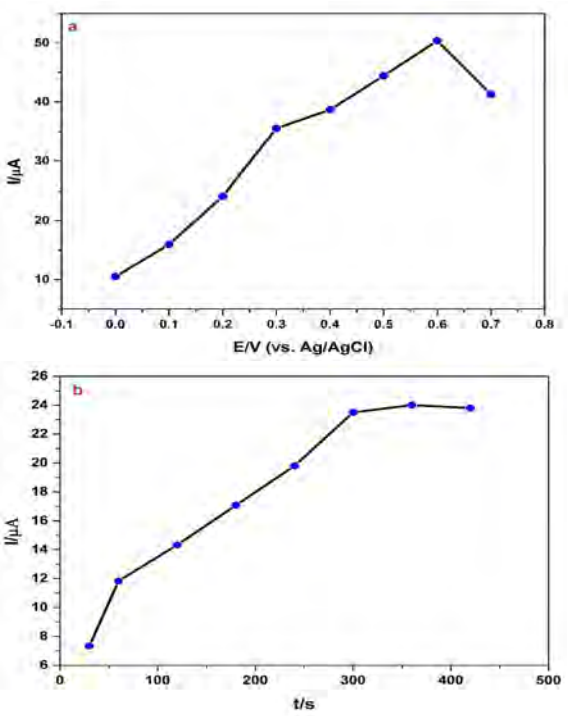

Figure 9. a) Effect of deposition potential and b) deposition time on the oxidation peak current of 0.5 μM CFX. (Under the same SWASV experimental conditions).

not strongly adsorbed on the electrode surface. Therefore, the optimum deposition potential was determined as 0.6 V (vs. Ag/AgCl).

To identify the optimum deposition time of CFX, different durations (60-420 s) at the optimum deposition potential were examined (Fig. 9.b). Up to 300 s, the peak currents increased and further increase in accumulation time yielded to almost stable response. This result proved that the sensor surface was saturated at 300 s deposition time. So, the optimum deposition time was selected as 300 s.

Analytical performance of the AuNP/GO/PGE

Since stripping analysis provides more sensitive measurements, it has frequently been applied for various drug determination studies [29–31]. Hence, under the optimized conditions, SWASV was performed for the quantitive detection of CFX (Fig. 10). The well-defined oxidation peak currents with respect to the increasing CFX concentrations were monitored and the measured peak currents increased linearly with CFX concentrations in the range of 0.02-2.0 μM. The corresponding calibration graph was illustrated in Fig. 10 (inset).

The obtained linear equation was (Eq.2),

$$I(\mu A) = 45.21\ C(\mu \mathrm{M}) + 3.412 \quad \mathrm{R}^2 = 0.9985\ . \qquad (2)$$

As a result, based on 3σ/m equation (σ is standard deviation of the analytical signal for the blank solution (n=3), m is the calibration curve slope), the LOD and LOQ were determined as 0.442 nM and 1.32 nM, respectively. When compared with other reported electrochemical studies about CFX (Table 2), the proposed sensing system had compatible results.

Furthermore, the intra/inter-day reproducibility of the AuNP/GO modified surface was examined by SWASV. To estimate reproducibility of the electrode, six AuNP/GO/PGE were fabricated independently and the RSD values for these electrodes were 2.43% (n=3) and 2.26% (for 6 days). The developed AuNP/GO/PGE showed good reproducible results. The interference study results showed

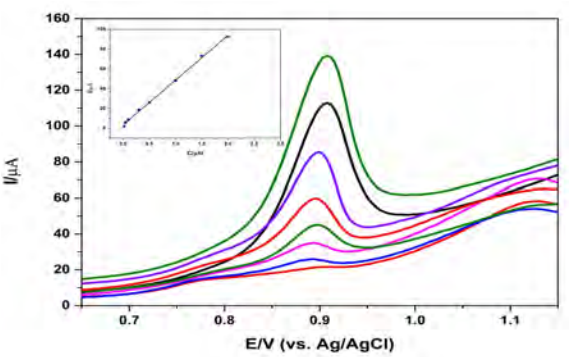

Figure 10. SWASV curves at AuNP-GO modified PGE in BRT containing 0.02; 0.05; 0.1; 0.5; 1.0; 1.50 and 2.00 μM (down to up) of CFX. (Inset: Linear calibration graph for CFX).

Table 2. List of electrochemical sensors of CFX.

Working electrode type	Method	LOD (M)	Linear Range (M)	Reference
AgNPs-ND-G/GCE	LSV	$6.0x10^{-9}$	2.0x10-8-7x10^{-6}	[12]
Fullerene/GCE	SWV	$6.6x10^{-10}$	2.96x10-6-25.4 x10^{-6}	[11]
Poly(o-anisidine)/SDS/Ni/CPE	chronoamperometry	$8.0x10^{-5}$	1.0x10-5-2.0x10^{-3}	[13]
MIP/Ag@AuNPs/ILs/GCE	DPV	$2.0x10^{-12}$	1.0x10-9-1.0x10^{-11}	[32]
HGNPs/rGO/PGE	AdDPV	$3.5x10^{-13}$	1.0x10-12-1.0x10^{-11} 1.0x10-11- 1.0x10^{-9}	[33]
AuNP/GO/PGE	SWASV	$4.42x10^{-10}$	2.0x10-8-2.0x10^{-6}	This work

GCE: Glassy carbon electrode, AgNPs-ND-G: silver nanoparticles Decorated Nano Diamond, SDS: sodium dodesulphate, CPE: carbon paste electrode, MIP/Ag@AuNPs/ILs: molecularly imprinted polymer based silver@gold nanoparticles/ionic liquid, HGNPs/rGO: Hollow gold nanoparticles/reduced graphene oxide, AdDPV: adsorptive differential pulse voltammetry.

that 250 fold concentration of ascorbic acid, 150 fold concentration of glucose and 150 fold concentration of lidocaine had no significant influence on the measured 0.5 µM CFX peak current (RSD values less than 5%).

Real Sample Analysis

The commercial CFX tablet was used to show the practical application of AuNP/GO modified PGE. The tablet samples were analysed by standard addition method and the recovery values of different concentrations of spiked CFX were given in Table 3.

The recovery and precision values confirmed that the adjuvants of the drug did not show important interference on the voltammetric response of CFX. These results clearly proved that this sensor system can be used in real samples for the detection of CFX with high accuracy.

CONCLUSION

A simple and an effective disposable sensor system based on AuNP/GO was developed for the electrochemical detection of CFX for the first time. When PGE surface was coated with AuNP/GO, the oxidation peak of CFX improved remarkably due to a synergistic effect. The optimum conditions were examined for the detection of CFX by SWASV. The described ultra-sensitive detection strategy had good sensing performance and exhibited comparable results with the literature. To demonstrate the success of the practical application, the developed sensor system was applied to the commercial CFX tablet and the obtained recovery values showed that the proposed system can be used in real matrixes with high accuracy. The disposable modified sensor offers favourable features for the electrochemical detection of CFX in terms of high sensitivity, rapidness, simplicity and cost-effectiveness.

Table 3. Determination of CFX in tablet samples by standard addition method (n=3).

Sample	Added (µM)	Detected (µM)	RSD (%)	Recovery (%)
Tablet	0.0264	0.0261	1.60	101
	0.0600	0.0581	1.39	97.0
	0.0750	0.0742	1.29	99.0

ACKNOWLEDGEMENT

The authors acknowledge to the Research Council of Hacettepe University for financially supporting this study (THD-2015-7394).

References

1. Abo El-Maali N, Ghandour M a., Kauffmann JM. Cephalosporin antibiotics at carbon paste and modified carbon paste electrodes in both aqueous and biological media. Bioelectrochemistry and Bioenergetics 38 (1995) 91–97. DOI: 10.1016/0302-4598(95)01822-V.
2. Facca B, Frame B, Triesenberg S. Population pharmacokinetics of ceftizoxime administered by continuous infusion in clinically ill adult patients. Antimicrobial Agents and Chemotherapy 42 (1998) 1783–1787.
3. Wiseman LR, Benfield P. Cefprozil: A Review of its Antibacterial Activity, Pharmacokinetic Properties, and Therapeutic Potential. Drugs 45 (1993) 295–317. DOI: 10.2165/00003495-199345020-00008.
4. Jain R, Gupta VK, Jadon N, Radhapyari K. Voltammetric determination of cefixime in pharmaceuticals and biological fluids. Analytical Biochemistry 407 (2010) 79–88. DOI: 10.1016/j.ab.2010.07.027.
5. Ferreira SMZMD, Domingos GP, Ferreira DDS, Rocha TGR, Serakides R, De Faria Rezende CM, et al. Technetium-99m-labeled

ceftizoxime loaded long-circulating and pH-sensitive liposomes used to identify osteomyelitis. Bioorganic and Medicinal Chemistry Letters 22 (2012) 4605–4608. DOI: 10.1016/j.bmcl.2012.05.105.

6. Sanli S, Sanli N, Gumustas M, Ozkan S a., Karadas N, Aboul-Enein HY. Simultaneous estimation of ceftazidime and ceftizoxime in pharmaceutical formulations by HPLC method. Chromatographia 74 (2011) 549–558. DOI: 10.1007/s10337-011-2116-1.
7. Moore CM, Sato K, Hattori H, Katsumata Y. Improved HPLC method for the determination of cephalosporins in human plasma and a new solid-phase extraction procedure for cefazolin and ceftizoxime. Clinica Chimica Acta 190 (1990) 121–123. DOI: 10.1016/0009-8981(90)90290-9.
8. Péhourcq F, Jarry C. Determination of third-generation cephalosporins by high-performance liquid chromatography in connection with pharmacokinetic studies. Journal of Chromatography A 812 (1998) 159–178. DOI: 10.1016/S0021-9673(98)00265-9.
9. Wang L, Zheng X, Zhong W, Chen J, Jiang J, Hu P. Validation and Application of an LC–MS-MS Method for the Determination of Ceftizoxime in Human Serum and Urine. Journal of Chromatographic Science 54 (2016) 713–719. DOI: 10.1093/chromsci/bmv243.
10. Al-Momani I. Spectrophotometric determination of selected cephalosporins in drug formulations using flow injection analysis. Journal of Pharmaceutical and Biomedical Analysis 25 (2001) 751–757. DOI: 10.1016/S0731-7085(01)00368-5.
11. Jain R, Rather JA, Dwivedi A, Vikas. Highly Sensitive and Selective Voltammetric Sensor Fullerene Modified Glassy Carbon Electrode for Determination of Cefitizoxime in Solubilized System. Electroanalysis 22 (2010) 2600–2606. DOI: 10.1002/elan.201000243.
12. Shahrokhian S, Ranjbar, S, Ghalkhani, M.. Modification of the Electrode Surface by Ag Nanoparticles Decorated Nano Diamond-graphite for Voltammetric Determination of Ceftizoxime. Electroanalysis, 28, (2016) 469-476. DOI: 10.1002/elan.201500377
13. Ojani R, Raoof JB, Zamani S. A novel sensor for cephalosporins based on electrocatalytic oxidation by poly(o-anisidine)/SDS/Ni modified carbon paste electrode. Talanta 81 (2010) 1522–1528. DOI: 10.1016/j.talanta.2010.02.062.
14. Erdem A, Papakonstantinou P, Murphy H. Direct DNA hybridization at disposable graphite electrodes modified with carbon nanotubes. Analytical Chemistry 78 (2006) 6656–6659. DOI: 10.1021/ac060202z.
15. Pumera M, Ambrosi A, Bonanni A, Chng ELK, Poh HL. Graphene for electrochemical sensing and biosensing. TrAC-Trends in Analytical Chemistry 29 (2010) 954–965. DOI: 10.1016/j.trac.2010.05.011.
16. Yuan B, Xu C, Deng D, Xing Y, Liu L, Pang H, et al. Graphene oxide/nickel oxide modified glassy carbon electrode for supercapacitor and nonenzymatic glucose sensor. Electrochimica Acta 88 (2013) 708–712. DOI: 10.1016/j.electacta.2012.10.102.
17. Promphet N, Rattanarat P, Rangkupan R, Chailapakul O, Rodthongkum N. An electrochemical sensor based on graphene/polyaniline/polystyrene nanoporous fibers modified electrode for simultaneous determination of lead and cadmium. Sensors and Actuators B: Chemical 207 (2015) 526–534. DOI: 10.1016/j.snb.2014.10.126.
18. Tiwari I, Singh M, Pandey CM, Sumana G. Electrochemical genosensor based on graphene oxide modified iron oxide-chitosan hybrid nanocomposite for pathogen detection. Sensors and Actuators, B: Chemical 206 (2015) 276–283. DOI: 10.1016/j.snb.2014.09.056.
19. Gan T, Sun J, Huang K, Song L, Li Y. A graphene oxide-mesoporous MnO2 nanocomposite modified glassy carbon electrode as a novel and efficient voltammetric sensor for simultaneous determination of hydroquinone and catechol. Sensors and Actuators, B: Chemical 177 (2013) 412–418. DOI: 10.1016/j.snb.2012.11.033.
20. Cheemalapati S, Palanisamy S, Mani V, Chen SM. Simultaneous electrochemical determination of dopamine and paracetamol on multiwalled carbon nanotubes/graphene oxide nanocomposite-modified glassy carbon electrode. Talanta 117 (2013) 297–304. DOI: 10.1016/j.talanta.2013.08.041.
21. Yaman YT, Abaci S. Sensitive adsorptive voltammetric method for determination of Bisphenol A by gold nanoparticle/polyvinylpyrrolidone-modified pencil graphite electrode. Sensors (Switzerland) 16 (2016) 756. DOI: 10.3390/s16060756.
22. Suea-Ngam A, Rattanarat P, Wongravee K, Chailapakul O, Srisa-Art M. Droplet-based glucosamine sensor using gold nanoparticles and polyaniline-modified electrode. Talanta 158 (2016) 134–141. DOI: 10.1016/j.talanta.2016.05.052.
23. Afkhami A, Bahiraei A, Madrakian T. Gold nanoparticle/multi-walled carbon nanotube modified glassy carbon electrode as a sensitive voltammetric sensor for the determination of diclofenac sodium. Materials Science and Engineering C 59 (2016) 168–176. DOI: 10.1016/j.msec.2015.09.097.
24. Saengsookwaow C, Rangkupan R, Chailapakul O, Rodthongkum N. Nitrogen-doped graphene-polyvinylpyrrolidone/gold nanoparticles modified electrode as a novel hydrazine sensor. Sensors and Actuators, B: Chemical 227 (2016) 524–532. DOI: 10.1016/j.snb.2015.12.091.
25. Kanyong P, Rawlinson S, Davis J. Gold nanoparticle modified screen-printed carbon arrays for the simultaneous electrochemical analysis of lead and copper in tap water. Microchimica Acta 183 2016 2361–2368. DOI: 10.1007/s00604-016-1879-3.
26. Mani V, Periasamy A P, Chen S. Highly selective amperometric nitrite sensor based on chemically reduced graphene oxide modified electrode. Electrochemistry Communications 17 2012 75-78. DOI: 10.1016/j.elecom.2012.02.009
27. Yavuz S, Erkal A, Af İ, Solak AO. Carbonaceous Materials-12 : a Novel Highly Sensitive Graphene Oxide-Based Carbon Electrode : Preparation , Characterization and Heavy Metal Analysis in Food Samples 9 (2016) 322-331. DOI: 10.1007/s12161-015-0198-3.
28. Sleegers N, Van Nuijs ALN, Van Den Berg M, De Wael K. Cephalosporin Antibiotics: Electrochemical Fingerprints and Core Structure Reactions Investigated by LC-MS/MS. Analytical Chemistry 91 (2019) 2035–2041. DOI: 10.1021/acs.analchem.8b04487.
29. Rodríguez J, Castañeda G, Lizcano I. Electrochemical sensor for leukemia drug imatinib determination in urine by adsorptive striping square wave voltammetry using modified screen-printed electrodes. Electrochimica Acta 269 (2018) 668–675. DOI: 10.1016/j.electacta.2018.03.051.
30. Santos AM, Wong A, Cincotto FH, Moraes FC, Fatibello-Filho O. Square-wave adsorptive anodic stripping voltammetric determination of norfloxacin using a glassy carbon electrode modified with carbon black and CdTe quantum dots in a chitosan film. Microchimica Acta 186 (2019) 148. DOI: 10.1007/s00604-019-3268-1.
31. Temerk YM, Ibrahim HSM, Schuhmann W. Square Wave Cathodic Adsorptive Stripping Voltammetric Determination of the Anticancer Drugs Flutamide and Irinotecan in Biological Fluids Using Renewable Pencil Graphite Electrodes 28 (2016) 372–379. DOI: 10.1002/elan.201500329.
32. Beytur M, Kardaş F, Akyıldırım O, Özkan A, Bankoğlu B, Yüksek H, et al. PT. Journal of Molecular Liquids 251 (2017) 212-217. DOI:

10.1016/j.molliq.2017.12.060.
33. Azadmehr F, Zarei K. Ultrasensitive determination of ceftizoxime using pencil graphite electrode modified by hollow gold nanoparticles / reduced graphene oxide. Arabian Journal of Chemistry 2018, (in press). DOI: 10.1016/j.arabjc.2018.02.004.

Hittite Journal of Science and Engineering, 2020, 7 (2) 99-108
ISSN NUMBER: 2148-4171
DOI: 10.17350/HJSE19030000178

A Knowledge-Based System for Fine Aggregate Material Problem Selection in Concrete Production

Abdullah Demir
Kutahya Dumlupinar University, Department of Civil Engineering, Kutahya, Turkey

ABSTRACT

One of the main problems of our country is inability to select the right materials of high quality in production. Decision making based on multiple criteria has an important role to do the right selections in each sector. One of these sectors is construction. Construction sector develops rapidly and using the right material is an important issue. Using the right material in this period when construction sector develops rapidly has a great importance. In the construction sector, the building material which has been used the most widely from past to present is concrete. In this study, a knowledge-based system via TOPSIS approach was proposed to generalize the multi-criteria decision making problems of fine aggregate material selection in concrete production. In addition, six different mortar series were produced by using the fine aggregates which were obtained from various plants used in the production of ready-mixed concrete in Kütahya and CEN Standard sand. The methylene blue, physical and mechanical tests were carried out on the produced mortars in order to get an idea for the strength and durability of concrete. The purpose of the study was to determine which of the five different fine aggregates had characteristics that are the closest to those of CEN Standard sand based on defined these multi criteria. It was found that the best fine aggregate series was A based on the defined criteria by considering the results of the experiments, assigning weights based on importance and analyzing these with TOPSIS approach.

Article History:
Received: 2019/12/20
Accepted: 2020/05/10
Online: 2020/06/26

***Correspondence to**: Abdullah Demir, Deparment of Civil Engineering, Kütahya Dumlıpınar University, Kütahya, Demir*
Tel: +90 2744434140
Fax: +90 2742652066
E-Mail:abdullah.demir@dpu.edu.tr

Keywords:
Knowledge-based system, Concrete Production, Fine Aggregate, Material Selection, MCDM, TOPSIS,

INTRODUCTION

Nowadays, the competition of the companies continues rapidly and each of them tries to make the best decisions. Decision making in all sectors should be made according to the different criteria at the same time. Multi-criteria decision making problems can be handled in different areas such as construction sector. The decisions should be made by trying to optimize each criterion but some of them conflict. Therefore multi-criteria decision making (MCDM) approaches can be used in these problems.

Aggregates which constitute the undercarriage of concrete, the most widely used load bearing structure material, are used in amounts of 1600 to 1900 kg in 1 m^3 of concrete mixture based on varying factors. While the physical (petrographic structure, granulometric combination, density and water absorption ratio, unit weight, organic and washable material ratio, alkaline aggregate reactivity, abrasive strength, etc.) and mechanical (compressive strength, modulus of elasticity, Poisson's ratio) properties of aggregate effect the concrete's strength, durability, stability in time, appearance, weight and workability, they also play an important role in the unit material cost of the concrete. For example, the elasticity module of the concrete is controlled by the elasticity module of the mixture and aggregate, and therefore, aggregate choice becomes important in cases where portion calculations and fineness are important. Additionally, the aggregate's physical properties are important in choice of methods in concrete mixture design [1]. In case of strong, quality aggregate with constant water absorption ratio, the design is based on a constant water/cement ratio. In this case, the standard deviation of compression strength becomes smaller. If the aggregate has high water absorption ratio, it comes from different sources or there are fluctuations in its granulometric composition, the design of the mixture is prepared based on constant settlement. Preference and control of the aggregate are also important for quality control. The main properties preferred for concrete aggregates are the following:

- Suitable granulometrics
- Exclusion of harmful materials
- Sufficient strength

- Suitable grain shape
- Strength against frost

Based on the place where the concrete will be used and conditions of usage and environment, some of the properties mentioned above may be more important, while some may be less important. While choosing the source of aggregate, these properties are determined by conducting laboratory analyses, investigating reports of previous analysis and consulting other users who supply aggregates from the same source. In addition to these, capacity of the furnace, uniformity of the material, organization and the order of working are also considered. After determining potential sources, concrete mixture trials are made and technical and economic tests are conducted. Quality is also constantly controlled during production.

Decision makers may encounter multi-criteria problems in every area and they aim to find the most suitable solutions to these problems in the shortest possible time. For this problem in CEN (European Committee for Standardization) standard sand with different aggregates, methylene blue, compressive strength, ultrasonic pulse velocity, water absorption by weight, flexural strength, capillarity coefficient and modulus of dynamic elasticity values were obtained and the most suitable aggregate series was obtained. Therefore, TOPSIS (Technique for Order Preference by Similarity to Ideal Solution) approach, which is one of the methods of multi criteria decision making, was used with this purpose. On the other hand, a knowledge based system for TOPSIS was proposed to generalize the MCDM problems in material selection.

TOPSIS approach was developed by Hwang and Yoon in 1981 to solve multi criteria decision making problems [2]. The logic of the approach is based on determining the option that is the closest to the positive ideal solution and farthest from the negative ideal solution [3]. Its application in different fields may be seen in the literature. These fields include energy, strategy, production/engineering [4], supply chain management and logistics, marketing, human resources, environment and resource management [5], financial performance analysis [6].

In this study, a knowledge-based system was proposed to find out the optimum aggregate serial. Based on this opinion, some experiments were made in order to obtain the methylene blue values and physical and mechanical properties of fine aggregates used as fine materials in the ready-mixed concrete plant in the province of Kütahya. According to the experiment results, it was aimed to determine the sample with properties that are the closest to those of CEN Standard sand, accepted as the ideal, by considering multi criteria via TOPSIS approach. Also, the proposed knowledge-based system can be used to evaluate different materials.

TOPSIS AND KNOWLEDGE-BASED SYSTEM FOR MATERIAL SELECTION

Material selection problem is one of the important multi criteria decision making problems for the production processes in the sectors and also the environmental impacts in the world. The problem has been studied in the literature in different aspects. Jahan et al. [7] studied on a literature review and presented that TOPSIS, ELECTRE (Elemination and Choice Translating Reality English) and AHP (Analytic Hierarchy Process) have been the most prevalent techniques in material selection context. Warren Liao [8] presented two interval type 2 fuzzy multi-attribute decision making methods that based on TOPSIS for material selection problem. Yazdani and Payam [9] analyzed for different applications of microelectromechanical systems electrostatic actuators, based on the actuation voltage and force, speed of actuation and electrical resistivity, and selected the most appropriate materials by using TOPSIS and VIKOR (VlseKriterijumska Optimizacija I Kompromisno Resenje). Kaspar et al. [10] presented a formalized approach to support the material selection decisions. The approach is part of an overall material-oriented development methodology that considers production process and material information. Mousavi-Nasab and Sotoudeh-Anvari [11] used a simple and comprehensive MCDM-based framework to solve a material selection problem with TOPSIS, COPRAS (Complex Proportional Assessment) and DEA (Data Envelopment Analysis). Zhang et. al. [12] studied on how to select a suitable material in multiple bone transplant replacement materials with similar properties by a TOPSIS method. Maghsoodi et al. [13] studied on a material selection problem by applying a hybrid decision-making approach supported on the Step-Wise Weight Assessment Ratio Analysis (SWARA) method and COmbinative Distance-based ASsessment (CODAS) technique containing target-based attributes. A case-study for selecting the optimal cement material type based on a real-world conceptual dam construction project in Iran has been analyzed.

In the literature, it can be seen that TOPSIS with information systems has been studied in some fields. Papathanasiou et al. [14] presented an implementation of a web-based decision support system that incorporates TOPSIS and VIKOR and allows decision makers to compare the results. Ploskas and Papathanasiou [15] studied on a decision support system for multiple criteria alternative ranking using TOPSIS and VIKOR in fuzzy and non-fuzzy environments. Kwok and Lau [16] studied on a decision support algorithm entitled as Vague Set TOPSIS to help travelers to rank the hotel options. Konstantinos et al. [17] proposed a methodo-

logy which is the combination of a MCDM and GIS (Geographic Information System) in order to determine the most suitable locations for wind farms installation. The calculated locations are then ranked with TOPSIS to rank the locations based on installation suitability.

In this study, a knowledge-system with TOPSIS was proposed for fine aggregate material selection problem in the production of ready-mixed concrete. To determine the contributions of the series in the concrete is an important issue and the problem can be recurrently solved based on the problem with an interactive way. Therefore a knowledge based system was proposed in the study.

The steps in the application of TOPSIS are given as the following:

Step 1. Formation of the decision matrix

Step 2. Formation of the standard decision matrix

Step 3. Formation of the weighted standard decision matrix

Step 4. Formation of the ideal (A^*) and negative ideal (A^-) solutions

Step 5. Calculation of the criteria of alternation

Step 6. Calculation of the relative proximity to the ideal solution

The interface of the knowledge-based system is given in Fig. 1. Matlab was used to design the system. The evaluation can be done by entering the number of criteria and series firstly, then the definitions can be made and after calculations the ranks can be given by the system.

Figure 1. Interface of the proposed knowledge-based system

While using TOPSIS in the knowledge-based system, the following steps were applied to evaluate the materials by the proposed system.

Step 1.Enter the number of criteria and series

Step 2.Define the criteria and series

Step 3.Enter the decision matrix

Step 4.Enter the weights of the criteria

Step5. Define the objectives' directions such as maximization or minimization

Step6. Select the TOPSIS type for the analysis and push 'Results Report' button.

The calculation details for TOPSIS are given with a case study in the fine aggregate material selection problem part.

MATERIALS AND EXPERIMENT RESULTS

The study consisted of four stages as methylene blue, sample production, physical and mechanical experiments.

Materials

The study used CEM I 42.4 R cement, produced by a cement factory. The chemical properties of this cement are given in Table 1. As water mixture, the city of Kütahya mains water with 5.8 mg/lt sulphate content, 3.9 mg/lt hardness and pH 6.3 was used. For the mixture series to be prepared, CEN Standard sand was used in the control series. In the remaining mixture series, fine aggregates obtained from different ready-mixed concrete facilities in Kütahya and designated as A, B, C, D and E were used.

Table 1. Properties of the cement

Properties	CEM I 42.5 R
SiO_2	20.74
Al_2O_3	5.68
Fe_2O_3	4.12
CaO	63.70
MgO	1.22
Na_2O	0.17
K_2O	0.53
SO_3	2.29
Cl	0.019
Loss ignition	1.34
Insoluble residue	0.57
Free lime	1.29
Specific gravity	3.14
Specific surface, cm^2/gr	3450
28 days compressive strength, MPa	48.5

Criteria

In the study, the methylene blue values of the fine materials were determined before starting mixture production. Methylene blue experiment starts with preparing a methylene blue solution. For the solution, 10 gr of methylene blue powder is added onto 50 ml of distilled water at 40°C in the beaker. It is stirred until the powder dissolves and cooled down to 20°C. The solution in the beaker is transferred to a 1-liter volumetric flask. Distilled water is added to fill it up to 1 liter and it is transferred to a lightly

colored protective glass bottle. After the methylene blue solution is prepared, stain experiment starts. To form a suspension, the dried part of experiment sample (200 gr of sand passed through 2 mm sieve) is added to 500 ml of distilled water by stirring. The suspension is mixed in the speed of 600 cycles/min for 5 minutes. Then 5 ml of stain solution is added, and the process continues at 400 cycles/min. After 1 minute of mixing, a drop is taken from the mixture by a glass rod and dropped on filter paper. The filter paper should be placed on a beaker or a suitable support so that its surface does not contact any solid or liquid. Mixture is continued after adding another 5 ml of stain. Again, after 1 minute, a drop is added on the filter paper. It is expected that a light blue circle surrounding a blue central accumulation will form. Otherwise, the same process is repeated by adding 5 ml of stain again. Stain experiment and stain addition is continued with 1 minute intervals until a circle is formed. After 5 minutes, the process is continued by adding 2 ml of stain instead of 5. In the case of circle formation, it the circle can be sustained for 5 minutes, the experiment is considered positive and ended. The amount of stain added until circle formation is recorded. The light blue circle's thickness should be about 1 mm for the accumulation between 8 mm and 12 mm [18].

In this study, mixture preparation was made based on TS EN 196-1 [19]. Based on TS EN 196-1 [19] materials were determined by mass as one-part cement, three-parts standard sand and 1/2-part water (water/cement ratio of 0.50). In amounts sufficient for three experiment containers with dimensions of 40x40x160 mm, 450±2 g CEM I 42.5 R, 1350±5 g aggregate and 225±1 g water were prepared for each mixture series. Cement, aggregate, water and devices were kept in the temperature of the laboratory environment.

A cement mixer suitable for TS EN 196-1 [19] was used for mixture preparation. The mixture is obtained as a result of mechanical mixing for 4 minutes. While the mixer is working, the water is poured into the mixing container and cement is added. Then the mixer is used in low speed, and after 30 seconds, the aggregate is added for 30 seconds by constantly stirring. When all materials are combined, the mixer is set to high speed and used for 30 more seconds. The mixer is stopped after 1 minute and 30 seconds. The parts of the mixture accumulated on the sides and base of the container are collected by a plastic scraper for 15 seconds and gathered in the middle. It is covered by a damp cloth and let rest for 75 seconds. Mixing is continued for another 60 seconds in high speed. The prepared mixture is added onto the molds with dimensions of 40x40x160mm in two steps, containing 60 free falls in each step on the vibratory table unit. The mixture series prepared in this way, after flattening the mixture surface at the end, were laid to rest for 24 in the climatization cabin with 90% relative humidity. The samples removed from the molds were kept in lime-saturated water at 20±2°C for physical and mechanical tests till the 7th and 28th days, and their physical and mechanical characteristics were determined in the following stage.

Results of the Methylene Blue Experiment

A methylene blue analysis experiment was run for the aggregates used in the study. The purpose of this experiment is to determine the content of clay-based materials in the fine aggregate. This is because humic and organic materials in fine aggregates distribute finely and damage the hardening and compression strength of the concrete, or distribute in grains and lead to changes in color or tearing on the surface of the concrete by expanding. It has been observed that aggregates with the same rate of fine materials provide very different methylene blue values. Fig. 2 shows the filter paper as a result of methylene blue in the sand E. The methylene blue results of other aggregates and relative analysis results obtained by taking the standard sand series representing CEN Standard sand as a reference are given in Fig. 3. Methylene blue values change in the range of 0.1-0.350 ml/g in series. The highest methylene blue value was in sand C, with 250% increase on the reference series. The lowest value was seen in sand A with 125% increase over the reference series. There were significant changes between the methylene blue values of the series and the reference value. In order to predict concrete behavior, there is a need for methylene blue experiment, which provides information about the quality of fine materials. Including this experiment in continuous quality control plans is useful to guarantee the sustainability of the quality of the aggregate, and the concrete produced with it.

Figure 2. Determining the methylene blue value of sand

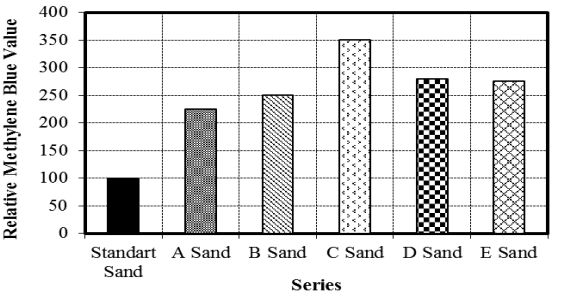

Figure 3. Relative methylene blue values

Physical and Mechanical Experiment Results

Unit weight, ultrasonic pulse velocity, water absorption by weight, capillarity, flexural strength and compressive experiments were conducted at the end of the 7th and 28th days on mixture samples prepared according to TS EN 196-1 [19]. Unit weights, ultrasonic pulse velocities, modules of dynamic elasticity, water absorption rates by weight, capillarity coefficients, flexural strengths and compressive strengths were calculated for the samples. In the analyses made in varying durations of curing, the results of relative values obtained by calculations taking the sample age of all samples of the standard sand series as a reference were explained.

Fig. 4 shows the changes in unit weight in series composed of different fine aggregates in different ages. The unit weights in the produced mixture series change between 2.12 and 3.15 g/cm^3. The unit weight of the standard sand series changes in the range of 2.23-2.25 g/cm^3. When the produced series were compared among each other especially in further ages, an average of 1% increase was seen in their unit weights. However, when their unit weights were analyzed in relation to the standard sand series, sands C and E had values that were 3% and 2% lower respectively. Therefore, it is concluded that the composition of the aggregates in these series were lower.

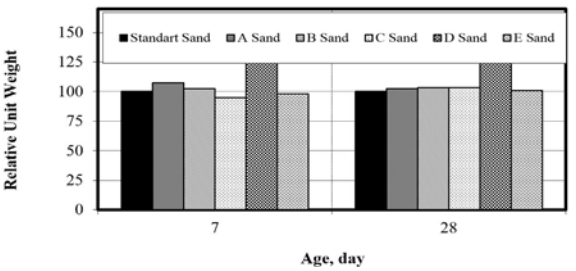

Figure 4. Relative unit weight values

In the ultrasonic pulse velocity experiment, the velocities were found between 32.1 and 52.4 μ s. Fig. 5 shows the calculated relative ultrasonic pulse velocities of the series. The values of ultrasonic pulse velocity changed between 4.98 and 2.94 km/s. At the end of the 7th and 28th days, the ultrasonic pulse velocities of the standard sand series were 4.73 and 4.98 respectively. The highest velocity values in different curing times were obtained from the standard sand series. Based on the results at the end of the 28th day, the standard sand was followed in order by sands C and A. It was observed that, as a result of two different curing times, all samples had ultrasonic pulse velocities over 3 km/s, except the 7th day value of the sand D. The ultrasonic pulse velocities of sand A and C series changed between 3.09 and 3.86 km/s at the end of two different curing times. Considering the change in velocities between the series' own values in two different curing times, the highest increase was seen in sand A by 9%. The highest rate of decrease based on the standard sand series was seen in sand D by 28%. This shows that porosity increased in sand D series.

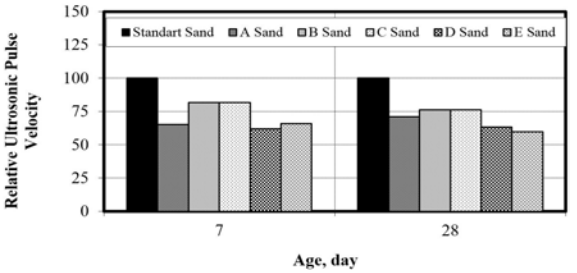

Figure 5. Relative ultrasonic pulse velocity values

Fig. 6 shows relative modulus of dynamic elasticity values calculated using the results of ultrasonic pulse velocity and unit weight. Modulus of dynamic elasticity (Edin) was calculated using Equation (1).

$$Edin = \frac{10^5 x V^2 x \Delta}{9.81} \quad (1)$$

In Equation (1), "V" is the ultrasonic pulse velocity in units of km/s, " Δ " is the unit weight in units of kg/lt, and the unit of Edin is GPa [20]. Modulus of dynamic elasticity values changed between 20.14 and 51.90 GPa. Considering the results, the changes in modulus of dynamic elasticity of sands A and C relative to the standard sand series were lower than those of other series. The highest decrease was found as 31% in sand E series in the 28th day.

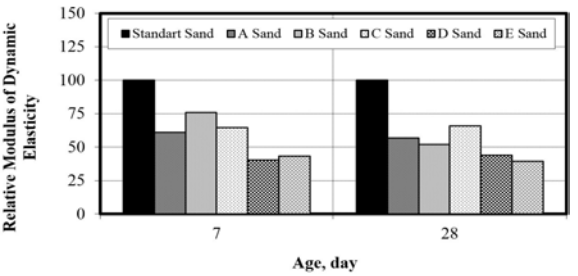

Figure 6. Relative modulus of dynamic elasticity values

Fig. 7 shows the tensile strength values calculated using the results of the flexural strength experiments conducted on mixture series. The tensile strength values changed between 2.47 and 4.51 MPa at the end of the 7th day. At the end of the 28th day, they changed between 6.28 and 4.00 MPa. Considering the tensile strengths at the end of the 7th day, tensile strength values of the series of sands A and B were higher than that of the standard sand series by 38% on average. At the end of the 28th day, it was observed that tensile strength values of all series except B were lower than that of the standard sand series. The increase in the tensile strength of sand B was 6% in relation to the standard sand series. The highest amount of decrease in relation to the standard sand series was seen in sands C, D and E by 23%.

The decrease in the series of sand A was approximately 10%.

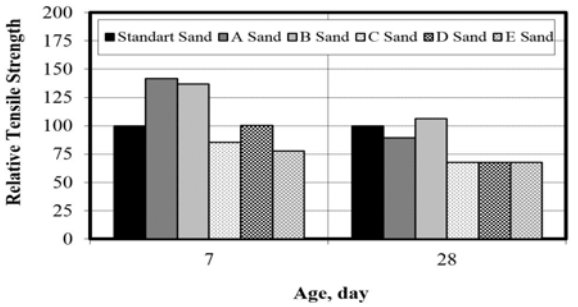

Figure 7. Relative tensile strength values

Fig. 8 shows the relative compressive strength values of the produced fine aggregate mixture samples. Compressive strength values were between 23.08 and 54.80 MPa. The 7th and 28th day values of the standard sand series were 38.7 and 54.80 MPa respectively. Compressive strengths of other series came out to be lower than those of the standard sand series. It was observed that only the compressive strength values of sands A and B were higher than that of the standard sand series by 10% and 5% respectively at the end of the 7th day. The sand A had a 10% lower value in relation to the standard sand series at the end of the 28th day. These series were followed by sand C (24%), sand E (37%) and sand D (43%). When the increase in strength of the series is considered within their own values, the highest increase from the 7th to the 28th day was seen in sand B by 44%.

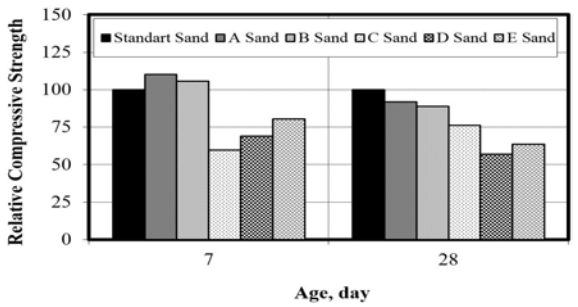

Figure 8. Relative compressive strength values

Fig. 9 shows the samples' water absorption by weight values. No very large differences were seen in the values of the series for different curing periods. The water absorption by weight values changed in the range of 7-11.15%. The standard sand series had the lowest water absorption by weight value. All other series had higher values. After the 7th day, the highest increase in water absorption by weight value was seen in sand D by 21%. A 3% decrease was observed in sand B series. However, in the water absorption by weight values calculated at the end of the 28th day, the highest increase was found again in sand D by 56%, and the lowest was found in sand C by 27%. It was followed by sands B, A and E with very small difference. The increase in the water absorption values is an important factor in understanding the permeability and therefore durability of the concrete in cases where physical characteristics are important. It is preferred that this value is not too high.

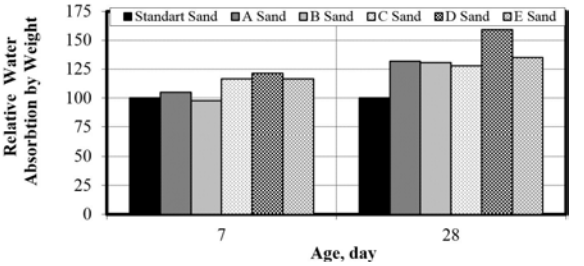

Figure 9. Relative water absorption by weight values

Fig. 10 shows the capillarity coefficients calculated using the capillary absorption experiments conducted on mixture samples. Capillarity coefficients changed between 1.79 x 10-6 and 7.64 x 10-6 cm^2/s. In the analyses conducted by taking the standard sand series as reference, the capillarity coefficients of all series were found low at the end of the 7th day. In the capillarity coefficients obtained at the end of the 28th day, there were increases in sands B and D by 6% and 20% respectively. The highest amount of decrease was found in the sand E series by 45%. This series was followed by the sand A series by 29%, and the sand C series by 24%. As opposed to the case in other properties, these series had lower capillarity coefficients in relation to the standard sand series. This is a preferred situation in cases where physical properties are important. This is because, due to the good distribution of aggregate grains in these series, the distances among grains are shorter, the connective mixture is used on an optimal level, the interface connections between the aggregate and the mixture are stronger, and a higher quality outer surface is formed.

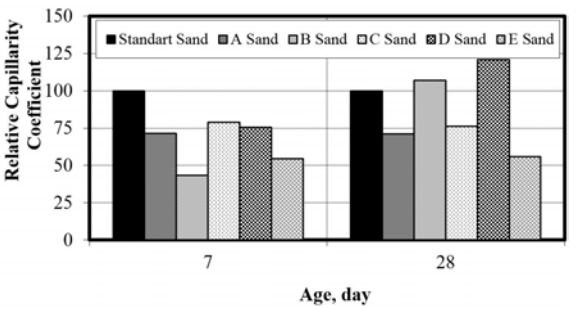

Figure 10. Relative capillarity coefficient values

Fine Aggregate Material Selection Problem

In this study, a fine aggregate material selection problem in concrete production was studied by designing a knowledge-system to obtain an interactive decision making environment. A case study for concrete production was analyzed with TOPSIS based knowledge system as in the steps below [2] and the most suitable series was proposed.

Step 1. Formation of the decision matrix

In the experiment results, methylene blue (ml/gr) (C1),

compressive strength (MPa) (C2), ultrasonic pulse velocity (km/s) (C3), water absorption by volume (%) (C4), flexural strength (MPa) (C5), capillarity coefficient (10-6 cm^2/s) (C6) and modulus of dynamic elasticity (GPa) (C7) were used as criteria and the decision matrix in Table 2 was formed.

Table 2. Decision matrix

	C1	C2	C3	C4	C5	C6	C7
Standart sand	0.10	54.80	4.98	7.00	5.91	3.20	51.90
A sand	0.23	50.28	3.54	9.23	5.29	2.28	29.55
B sand	0.25	48.62	3.37	9.14	6.28	3.42	26.97
C sand	0.35	41.76	3.79	8.95	4.01	2.44	34.12
D sand	0.28	31.30	3.15	11.15	4.01	3.87	22.76
E sand	0.28	34.84	2.98	9.44	4.00	1.79	20.49

In the proposed knowledge-based system, the decision matrix was obtained by using the data entry interface and definitions of series as given Fig. 11 and 12. The decision matrix can be seen in Fig. 13.

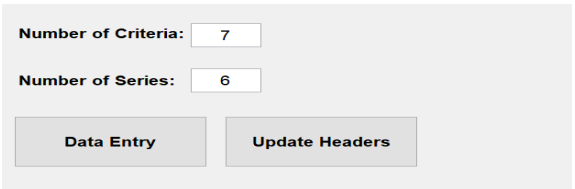

Figure 11. Data entry interface

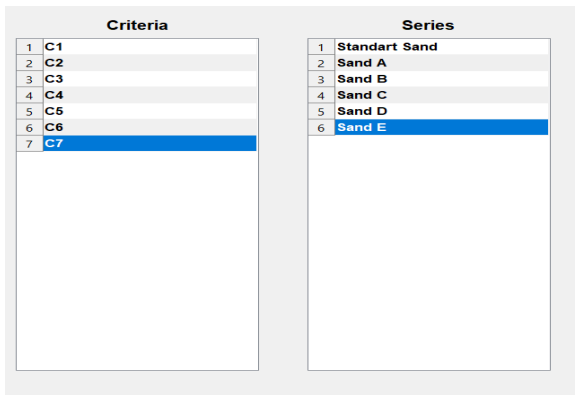

Figure 12. Definitions of criteria and series

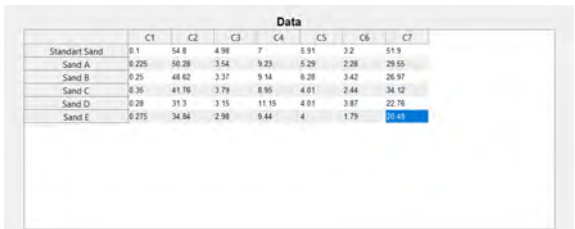

Figure 13. Decision matrix

Step 2. Formation of the standard decision matrix

All criteria were converted to the maximization form and the standard decision matrix was formed using the aij values in Table 3 as in the Equation (2).

$$r_{ij} = \frac{a_{ij}}{\sqrt{\sum_{k=1}^{m} a_{ij}^2}} \quad (2)$$

Table 3. Standard decision matrix

	C1	C2	C3	C4	C5	C6	C7
Standart sand	0.795	0.503	0.550	0.725	0.481	0.216	0.648
A sand	0.397	0.462	0.391	0.335	0.431	0.514	0.369
B sand	0.318	0.446	0.372	0.351	0.511	0.145	0.337
C sand	0.000	0.383	0.418	0.384	0.326	0.462	0.426
D sand	0.222	0.287	0.348	0.000	0.326	0.000	0.284
E sand	0.238	0.320	0.329	0.298	0.326	0.673	0.256

Step 3. Formation of the weighted standard decision matrix

While compressive strength, ultrasonic pulse velocity and flexural strength were criteria for maximization, others were criteria for minimization. All criteria were represented for maximization for calculations. While the weights of methylene blue, compressive strength and capillarity coefficient were 0.20 in the analyses, others' weights were 0.10. The weighted standard decision matrix in Table 4 was formed by multiplication of criterion values with the defined weights.

Table 4. Weighted standard decision matrix

	C1	C2	C3	C4	C5	C6	C7
Standart sand	0.159	0.101	0.550	0.073	0.048	0.043	0.065
A sand	0.080	0.092	0.039	0.034	0.043	0.103	0.037
B sand	0.064	0.089	0.037	0.035	0.051	0.029	0.034
C sand	0.000	0.077	0.041	0.038	0.033	0.093	0.043
D sand	0.045	0.058	0.035	0.000	0.033	0.000	0.028
E sand	0.048	0.064	0.033	0.030	0.033	0.135	0.026

The weights and the objectives were also entered to the proposed system as given in Fig. 14 and 15. On the other hand, the interface of the proposed system with data can be seen in Fig. 16.

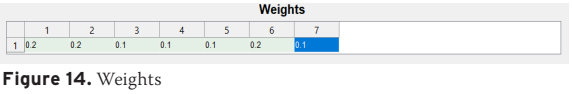

Figure 14. Weights

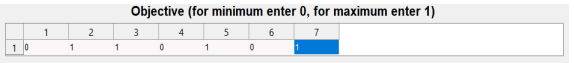

Figure 15. Objective directions

Step 4. Formation of the ideal (A^*) and negative ideal (A^-) solutions

The ideal solution set is formed by choosing the highest ones among the weighted analysis criteria. Formation of the ideal solution set is shown in Equation (3).

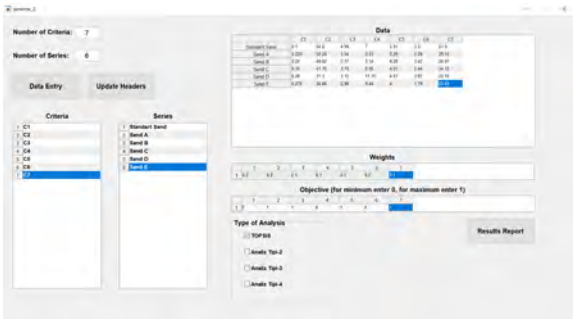

Figure 16. Interface of the knowledge-based system with data

$$A^* = \left\{ \left(\max_i v_{ij} \middle| j \in J \right), \left(\min_i v_{ij} \middle| j \in J' \right) \right\} \quad (3)$$

The set calculated using the Equation (3) may be shown as $A^* = v_1^*, v_2^*, \ldots, v_n^*$.

The negative ideal solution set is formed by choosing the smallest ones among the weighted analysis criteria. Formation of the negative ideal solution set is shown in Equation (4).

$$A^- = \left\{ \left(\min_i v_{ij} \middle| j \in J \right), \left(\max_i v_{ij} \middle| j \in J' \right) \right\} \quad (4)$$

The set calculated using the Equation (4) may be shown as $A \quad v_1, v_2, \ldots, v_n$.

Step 5. Calculation of the criteria of alternation

The Euclidean distance approach is used in the TOPSIS approach to find the deviations from the positive ideal and negative ideal solution sets of the analysis criteria value of each series. The deviation values of the determined series are defined as positive ideal alternative (S_i^*) and negative ideal alternative (S_i^-) criteria. Calculation of the positive ideal alternative (S_i^*) criterion is given in Equation (5), while calculation of the negative ideal alternative (S_i^-) criterion is given in Equation (6).

$$S_i^* = \sqrt{\sum_{j=1}^{n} (v_{ij} - v_j^*)^2} \quad (5)$$

$$S_i^- = \sqrt{\sum_{j=1}^{n} (v_{ij} - v_j^-)^2} \quad (6)$$

Step 6. Calculation of the relative proximity to the ideal solution

Ideal and negative ideal alternative criteria are used in calculation of the relative proximity of each series to the ideal solution, C_i^* . The values of proximity to the ideal solution were calculated using the Equation (7) and the rank of the series among themselves based on the considered criteria is given in Table 5. The results of the problem by the proposed knowledge-based system can be also seen in Fig. 17.

$$C_i^* = \frac{S_i^-}{S_i^- + S_i^*} \quad (7)$$

Table 5. Rank of the series

	S_i^*	S_i^-	C_i^*	Series
Standart sand	0.091	0.192	0.677	1
A sand	0.100	0.139	0.582	2
B sand	0.152	0.087	0.364	5
C sand	0.173	0.104	0.375	4
D sand	0.201	0.045	0.182	6
E sand	0.134	0.146	0.512	3

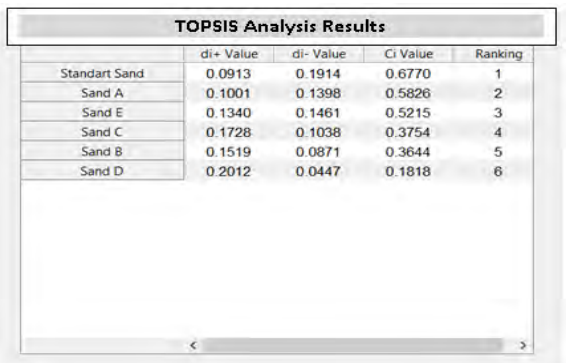

Figure 17. Interface of the analysis results

Considering these proximity values, the standard sand had the first place in the order of proximity to the ideal value. This situation is expected due to the fact that the standard sand was taken as ideal, while the aggregate series in the second place belonged to sand A.

CONCLUSION

In the study, a decision making problem with multiple criteria in selection of the most suitable aggregate series in the construction sector was studied. In this case, different related criteria were evaluated and tried to be optimized. TOPSIS approach was used to determine which of the five different aggregates used in concrete production as fine aggregate had properties that are the closest to those of CEN Standard sand, which was assumed to be ideal. The study utilized methylene blue experiments on fine aggregates in the series, and physical and mechanical experiments on mixture samples obtained using these aggregates. The outcomes of these experiments are given below:

- Results of methylene blue experiment showed that aggregates with the same fine material ratio had very different methylene blue values. The sand A series had the closest methylene blue value to that of the CEN Standard sand. Methylene blue experiment, which shows the

quality of fine material, is needed to predict the behavior of the concrete. It is recommended that aggregate producers should make improvements based on methylene blue experiment results.

- Based on the unit weight experiment results, the sand D series had a unit weight value higher than all other series.
- According to the ultrasonic pulse velocity experiment results, which provide information regarding the pockets in the mixture or the concrete, the highest values after those of CEN Standard sand belonged to sands C and A.
- According to the modulus of dynamic elasticity results obtained by using the unit weight and ultrasonic pulse velocity values, again, the series of sands C and A had the highest values following those of CEN Standard sand.
- The highest tensile strength value among the ones obtained as a result of flexural strength experiments was found in the series of sand B.
- In one of the most significant properties of concrete, the highest compressive strength was seen in sand A, after CEN Standard sand.
- While the physical property of water absorption by weight value is one of the preferred properties in cases where the concrete's strength against external factors is important, the series of sand C was found to have the lowest water absorption by weight value.
- While the capillarity coefficient is one of the most important physical properties that provide information on permeability, which is the most significant reason for problems in durability, the lowest value of capillarity coefficient in the study belonged to the series of sand E.

As the purpose of the study was to determine which of the five different fine aggregates had characteristics that are the closest to those of CEN Standard sand based on defined these multi criteria, it was found that the best fine aggregate series was A based on the defined criteria by considering the results of the experiments, assigning weights based on importance and analyzing these with TOPSIS approach. The ranks of the other series were as sand E, sand C, sand B and sand D. On the other hand, different criteria may be analyzed by using TOPSIS approach and different results may be obtained by changing the weights of the criteria in the future studies.

Considering all these issues, choice of materials and properties of such materials may be significant for the desired qualities of workability, strength and durability in concrete and technology of concrete. It may be difficult to make a decision in material selection when all properties are considered and there is a question of ranking the importance of certain criteria. Hence, it can be recommended to use multi criteria decision making techniques like TOPSIS in the selection or usage of materials to achieve more accurate results. On the other hand, as an extension of this study, it is thought that it would be beneficial for the sector to carry out study involving the solution of a problem in which all of the basic materials that make up concrete, such as cement, aggregate and concrete admixture, are included and cost information is added.

REFERENCES

1. Arıoğlu E, Köylüoğlu ÖS. Discussion of "estimation of coarse aggregate strength in high strength concrete" by TP Chang and N K Su. ACI Materials Journal November-December (1996) 637-639.
2. Olson DL. Comparison of weights in TOPSIS models. Mathematical and Computer Modelling 40 (2004) 721-727.
3. Wu DS, Olson DL. A TOPSIS data mining demonstration and application to credit scoring. International Journal of Data Warehousing and Mining 2(3) (2006) 1-10.
4. Huanga IB, Keislerb J, Linkov I. Multi-criteria decision analysis in environmental sciences: Ten years of applications and trends. Science of The Total Environment 409(19) (2011) 3578–3594.
5. Velasquez M, Hester PT. An analysis of multi-criteria decision making methods. International Journal of Operations Research 10(2) (2013) 56-66.
6. Feng CM, Wang RT. Considering the financial ratios on the performance evaluation of highway bus industry. Transport Reviews: A Transnational Transdisciplinary Journal, 21(4) (2001) 449-467.
7. Jahan A, Ismail MY, Sapuan, SM, Mustapha F. Material screening and choosing methods–a review. Materials & Design 31 (2010) 696-705.
8. Warren Liao T. Two interval type 2 fuzzy TOPSIS material selection methods. Materials & Design (2015) 1088-1099.
9. Yazdani M, Payam AF. A comparative study on material selection of microelectromechanical systems electrostatic actuators using Ashby, VIKOR and TOPSIS. Materials & Design 65 (2015) 328-334.
10. Kaspar J, Baehre D, Vielhaber M. Material selection based on a product and production engineering integration framework. Procedia CIRP 50 (2016) 2–7.
11. Mousavi-Nasab SH, Sotoudeh-Anvari A. A comprehensive MCDM-based approach using TOPSIS, COPRAS and DEA as an auxiliary tool for material selection problems. Materials & Design 121 (2017) 237-253.
12. Zhang K, Zhan J, Yao Y. TOPSIS method based on a fuzzy covering approximation space: An application to biological nano-materials selection. Information Sciences 502 (2019) 297-329.
13. Maghsoodi AI, Maghsoodi AI, Poursoltan P, Antucheviciene J, Turskis Z. Dam construction material selection by implementing the integrated SWARA–CODAS approach with target-based attributes. Archives of Civil and Mechanical Engineering 19(4) (2019) 1194-1210.
14. Papathanasiou J, Ploskas N, Bournaris T, Manos B. A Decision Support System for Multiple Criteria Alternative Ranking Using TOPSIS and VIKOR: A Case Study on Social Sustainability in Agriculture. In: Liu S., Delibašić B., Oderanti F. (eds) Decision Support Systems VI - Addressing Sustainability and Societal Challenges. ICDSST 2016. Lecture Notes in Business Information

Processing, 250. Springer, Cham, 2016.
15. Ploskas N, Papathanasiou J. A decision support system for multiple criteria alternative ranking using TOPSIS and VIKOR in fuzzy and nonfuzzy environments. Fuzzy Sets and Systems Available online 23 January 2019, in press (2019).
16. Kwok PK, Lau HYK. Hotel selection using a modified TOPSIS-based decision support algorithm. Decision Support Systems 120 (2019) 95-105.
17. Konstantinos I, Georgios T, Garyfalos A. A Decision Support System methodology for selecting wind farm installation locations using AHP and TOPSIS: Case study in Eastern Macedonia and Thrace region, Greece. Energy Policy 132 (2019) 232-246.
18. TS EN 933-9+A1. Tests for geometrical properties of aggregates - part 9: assessment of fines - methylene blue test. Turkish Standardization Institute, Ankara (in Turkish), 2014.
19. TS EN 196-1. Methods of testing cement - part 1: determination of strength. Turkish Standardization Institute Ankara (in Turkish), 2009.
20. Postacıoğlu B. Concrete-Binding Materials. Aggregates Concrete Volume 2, Turkey, Istanbul Technical University (in Turkish), 1986.

Hittite Journal of Science and Engineering, 2020, 7 (2) 109-114
ISSN NUMBER: 2148-4171
DOI: 10.17350/HJSE19030000179

Doped TiO_2 Photocatalysts for the Photocatalytic Degradation Efficiency of Methylene Blue and Humic Acid under Solar Light

Nazli Turkten[1] and Miray Bekbolet[2]
[1]Kirsehir Ahi Evran University, Department of Chemistry, Kirsehir, Turkey
[2]Bogazici University, Institute of Environmental Sciences, Istanbul, Turkey

ABSTRACT

In various advanced oxidation processes, photocatalysis is a promising and efficient way? to remove natural organic matter consisting of humic acids and fulvic acids. The principle of this method involves both usage of a semiconductor photocatalyst and O_2 for the generation of radicals. Among them, TiO_2 photocatalysis is the most popular and studied one since TiO_2 has unique properties such as being chemically inert, photocatalytically stable, cheap, non-toxic, environmentally benign and exhibiting high oxidative power. However, despite all the advantages of using TiO_2 as a photocatalyst, there is a major disadvantage. Since TiO_2 has a broad band gap, its usage widely under solar light is limited and only allows to be active under UV light. Doping is one of the most popular methods to enhance the photocatalytic activity of TiO_2 via using metal or non-metal species as dopants. In this respect, solar light sensitive TiO_2 photocatalyst, C, N, S, Se doped and S/N codoped TiO_2 photocatalysts were synthesized by using wet-impregnation method. These doped photocatalysts were characterized by Raman spectroscopy to determine the crystal surface morphology. Moreover, methylene blue was used to investigate the photocatalytic performance of prepared doped TiO_2 photocatalysts in the presence or absence of organic matrix. Photocatalytic experiments were performed using a solar light simulating photoreactor. Humic acid characterization was monitored by UV-vis and fluorescence spectroscopy.

Keywords:
Raman spectroscopy; Metal/non-metal doped TiO_2; Humic acid; Photocatalysis.

Article History:
Received: 2020/01/26
Accepted: 2020/05/01
Online: 2020/06/26

***Correspondence to**: Nazli Turkten, Kirsehir Ahi Evran University, Chemistry, 40100, Kirsehir, Turkey*
E-Mail: nazli.turkten@ahievran.edu.tr
Phone: +90 (386) 280 3104
Fax: +90 (386) 280 4525

INTRODUCTION

Wastewater is polluted with severe concentration of dyes in industries such as textile, cosmetic, paper, leather, food, etc. and this causes a critical environmental and health public issue [1, 2]. Accordingly, many studies have been reported for the removal of these colored effluents from wastewater using different methods such as physicochemical treatments, chemical methods, advanced oxidation processes (AOPs), and biological methods [3-8]. The application of the physicochemical treatments are limited because of the formation of sludge to be disposed of or the need of regeneration of the adsorbent materials. Although, biological methods are environmentally friendly and inexpensive, they are not effective to degrade the dyes in wastewaters and thus uncompleted degradation can cause secondary pollution. Even if ozonation is an effective process for the decolorization of dyes, this method causes very high operating costs [2, 9-11].

Among AOPs, heterogeneous photocatalysis in which a semiconductor, such as TiO_2, ZnO, SnO_2, etc. is used as a photocatalyst is an effective alternative method to conventional methods. TiO_2 photocatalysis is based on the formation of photogenerated charge carriers on the surface of titanium dioxide. Photocatalytic mechanism is initiated with the excitation and transfer of an electron from the valence band to the conduction band of TiO_2 and positively charged holes are formed in the valence band at the same time. These generated electron-hole reacts with water and O_2 or OH^- to form extremely reactive oxygen species (ROS) such as superoxide anions, and hydroxyl radicals. During the photocatalytic process, hydroxyl radicals react with surface adsorbed pollutants and leads them to degrade. Subsequently, further reactions with ROS could mineralize the organic matter to carbon dioxide and water [3, 4, 12].

TiO_2 is the most popular and promising photocatalyst with great photosensitivity and chemical stability. Moreover, it is non-toxic and a low-cost material. Nevertheless, TiO_2 with wide and gap of E_{bg}=3.2 eV limits its photocatalytic activity under solar light (This sentence needs correcting). Thus, doping method by using metal ions i.e. Cu, V, Se, Fe, etc., non-metal elements i.e. B, C, S, N, etc. and co-doping with metals and non-metals (N/S, N/Se, etc.) has been used to improve the photocatalytic activity of TiO_2 as an effective strategy under visible light [5, 7, 12-18].

In this study, C, N, S, Se doped and N/S codoped TiO_2 photocatalysts were synthesized by wet-impregnation method. Crystal surface morphology of the doped TiO_2 photocatalyts was determined by using Raman Spectroscopy. Photocatalytic acitivity of these specimens were investigated using methylene blue (MB) as a basic dye under simulated solar light in presence and absence of humic acid (HA) .

MATERIAL AND METHODS

Materials

Commercial HA (humic acid sodium salt) was purchased from Aldrich. TiO_2 Evonik P25 was used as the photocatalyst for doping procedure. Doped TiO_2 photocatalysts were synthesized via an incipient wet-impregnation method using $C_6H_{12}O_6$ (glucose), CH_4N_2O (urea), NH_2CSNH_2 (thiourea), $SeCl_4$ (selenium tetrachloride) and CH_4N_2O coupled with NH_2CSNH_2 (urea and thiourea) as C, N, S, Se and S/N sources, respectively. All doping sources and MB were purchased from Merck. Distilled water was used for the preparation of the solutions. The chemical structures of MB and HA are given in Fig. 1.

Preparation of Doped TiO_2 Photocatalysts

Dopant concentration was selected as 0.50% wt. for all photocatalysts as it was determined in previous work [13-18]. In incipient wet-impregnation method, 0.50% dopant agents in 15 mL water was added to 10 g TiO2 Evonik P25 and stirred for 1 h at room temperature. Afterwards, doped photocatalysts were washed with distilled water, dried in air oven at 378 K for 24 h, and calcined at a predetermined temperature and time which were given in Table 1. Finally, the obtained samples were ground and passes through a sieve (32 Micron) to achieve a more homogeneous size distribution.

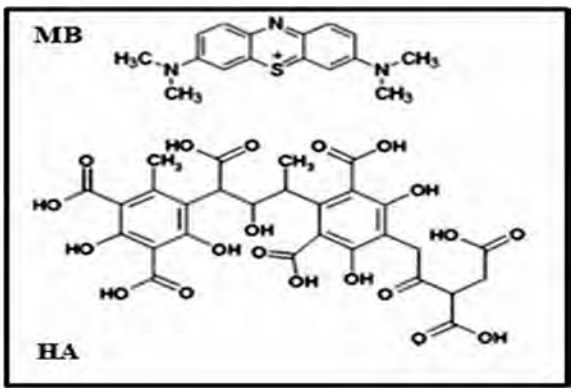

Figure 1. Chemical structures of MB and Steelink's proposed unit structure of HA [19].

Table 1. Calcination time and temperature for the prepared photocatalysts.

	Photocatalyst	*Synonym*	*Temperature & Calcination*
1	*C-doped TiO_2*	*C-350-3-TiO_2* *C-500-3-TiO_2*	*350°C 3h* *500°C 3h*
2	*N-doped TiO_2*	*N-350-3-TiO_2* *N-500-3-TiO_2*	*350°C 3h* *500°C 3h*
3	*S-doped TiO_2*	*S-350-3-TiO_2* *S-500-3-TiO_2*	*350°C 3h* *500°C 3h*
4	*Se-doped TiO_2*	*Se-350-3-TiO_2*	*350°C 3h*
5	*N/S-codoped TiO_2*	*N/S-350-3-TiO_2*	*350°C 3h*

Solar Photocatalytic Experiments

Atlas-Suntest CPS+ solar simulator was used for the photocatalytic experiments [16]. The solar degradation of MB (20 mg/L) using doped TiO_2 specimens under solar light with 60 min irradiation time in presence and absence of HA (20 mg/L) was investigated. After the photocatalytic process, TiO_2 was removed by a filtration process. The photocatalytic experiments were carried out without pH adjustment (pH~5.5).

Characterization

Absorbance of filtered MB solutions at λ=662 nm was monitored by UV-vis spectrophotometry (Perkin Elmer lambda 35). EEM fluorescence spectra was measured by a Luminescence Spectrometer (Perkin Elmer LS 55). The detailed procedure was given in our previous work [16]. Raman spectra were acquired by a Thermo Scientific NXR FT-Raman spectrometer using Ar^+ laser excitation at λ=532 nm, with a laser power 10 mW and a resolution 2 cm^{-1}.

RESULTS AND DISCUSSION

Raman Spectroscopy

Raman spectroscopy was employed for the characterization of the surface structure and identifying the phase transformation of doped TiO^2 photocatalysts. Moreover,

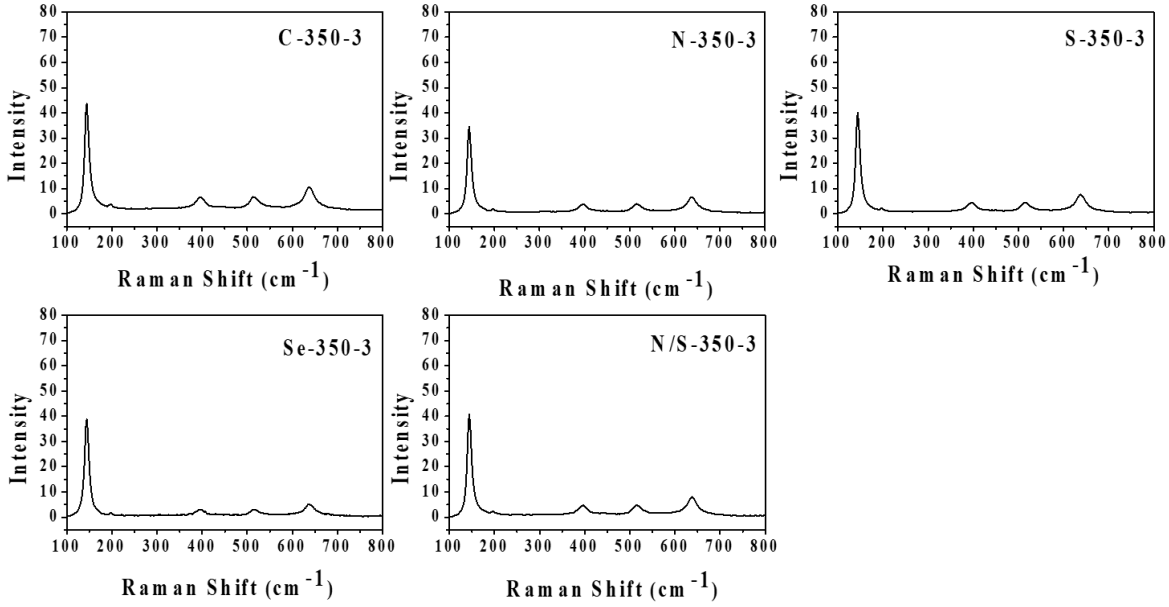

Figure 2. FT-Raman spectra of doped TiO_2 samples calcined at 350°C for 3h.

the effect of different dopant agents and different calcination temperatures on the transformation of crystallographic phases were identified. The FT-Raman spectra of the doped TiO_2 samples calcined at 350°C for 3h are displayed in Fig. 2.

Raman peaks were acquired at 144 (E_g), 197 (E_g), 397 (B_{1g}), 515 (A_{1g}, B_{1g}), and 637 (E_g) cm^{-1} in the spectra of each sample, indicating the presence of anatase phase [16, 20]. Similarly, Raman spectroscopy of the samples calcined at 500°C for 3h (Fig. 3) revealed the presence of only anatase phase.

Any phase transformation from anatase phase to rutile phase and any significant shift in the Raman bands were not observed as expected. The reason could be explained by the anatase phase transformation to rutile phase starting at 550°C [21].

Photocatalytic Experiments

Photocatalyst performances were estimated by the removal percentage values of MB in the absence and presence of HA. Removal percentages were determined from Equation (1), where C_0 is the initial concentration of MB and C is concentration at time t of MB.

$$\text{Re}moval\% = \frac{C_0 - C}{C_0} x100 \quad (1)$$

In Fig. 4 (a), removal % values of MB by using doped TiO_2 photocatalysts under solar light at 60 min are shown. Se-350-3 and N-350-3 TiO_2 photocatalysts exhibited the highest removal of MB as 87.30% and 89.31%, respectively. It was found that N/S-350-3 TiO_2 has the lowest ability for the decolorization of MB compared to other doped photocatalysts. Moreover, the effect of calcination temperature on the anion doped photocatalysts (C-doped TiO_2, N-doped TiO_2 and S-doped TiO_2 photocatalysts) were investigated and shown in Fig. 4 (b). N-doped and C-doped TiO_2 photocatalysts almost exhibited the same removal efficiency, while S-doped TiO_2 samples performed a lowered photocatalytic activity with increasing calcination temperature. The reason may be explained by its having a large surface area compared to N-doped and C-doped TiO_2 samples which were reported in our previous work [13]. A larger surface area could promote an increment on the photogenerated electrons and photocatalytic activity [22]. For this reason, a further study is needed to investigate the removal percentage of anionic dyes by using anion doped TiO_2 photocatalysts.

In Fig. 4 (c), the removal % efficiency of MB with the presence of HA is shown. HA caused a retardation effect on the photocatalytic system. The reason of this retardation could be explained by two assumptions.

i)HA could reduce the light transmittance thereby effects photo-oxidation process.

ii) The competition between HA and MB for the active sites of TiO_2 surface [23].

Fig. 5 displays the UV-vis spectra of MB solution with the absence and presence of HA after 60 min for doped TiO_2 photocatalysts. The spectrum of MB was characte-

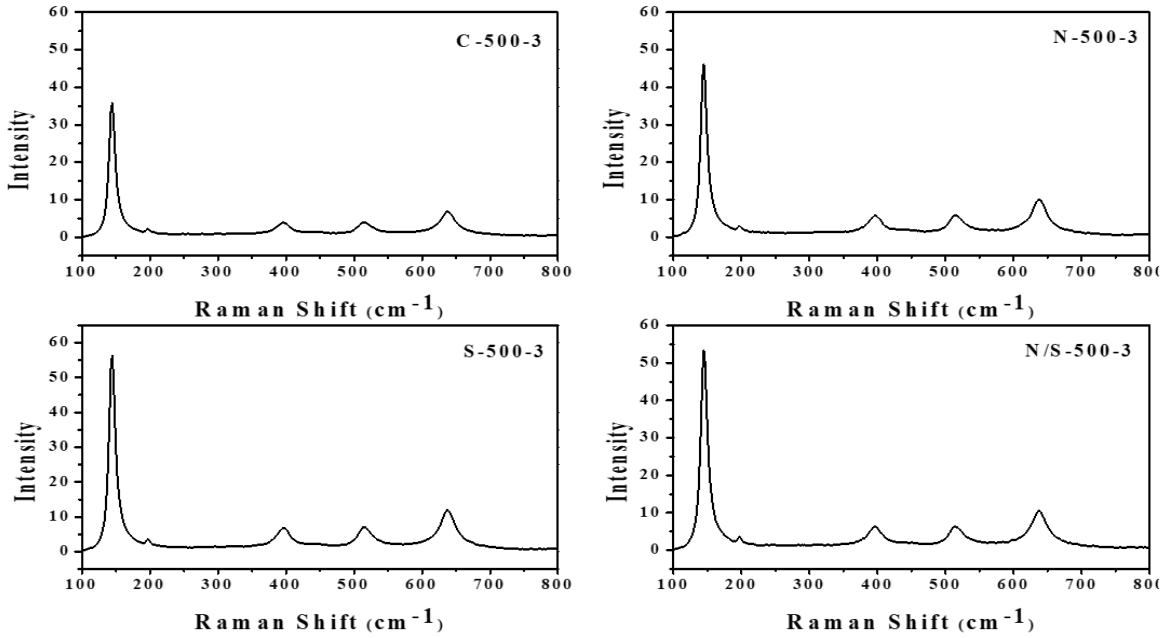

Figure 3. FT-Raman spectra of doped TiO_2 samples calcined at 500°C for 3 h.

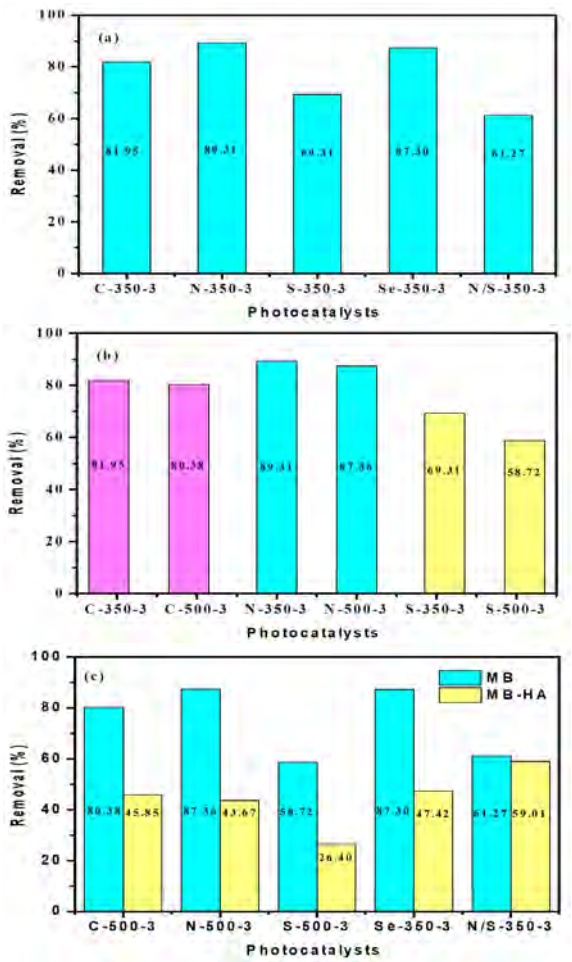

Figure 4. The removal % values of MB **(a)** 350°C 3h, **(b)** 350°C and 500°C 3h, **(c)** the retardation effect of HA.

rized by an absorption band λ=662 nm and a shoulder at 612 nm in visible light region. This absorption band was attributed to a chromophore including an elongated conjugate system. The absorption bands located in the UV region at 292 nm and 245 nm were corresponded to the conjugated system of the benzene ring structure [24, 25].

In Fig. 5 (a) and (b), the characteristic absorption peak of MB solution at 662 nm was significantly lowered in intensity with solar light irradiation and the shoulder was disappeared. Furthermore, a decrease in the intensity of benzene rings after irradiation, confirmed that decolorization and degradation of MB occurs at the same time. Among all doped TiO_2 photocatalysts, N-TiO_2 was the most effective one and decolorize approximately 87-89% of MB after 60 min. In Fig. 5 (c), the presence of HA effected the disappearance of hump at 612 nm after irradiation. Besides, the intensity of aromatic peaks and maximum absorption peak were decreased as expected after 60 min. However, the retardation effect of HA caused an adverse impact by decreasing the intensity of peaks compared to the peaks in absence of HA spectra.

EEM Fluorescence Contour Plots

Regional specification of the EEM spectra of HA was expressed in four regions. Region I, II and III were defined as aromatic proteins I, aromatic proteins II and fulvic-like in the excitation wavelength region of λ_{exc}=200–250 nm with emission wavelength regions of λ_{emis}=280–332 nm, λ_{emis}=332–380 nm and λ_{emis}=380–580 nm respectively.

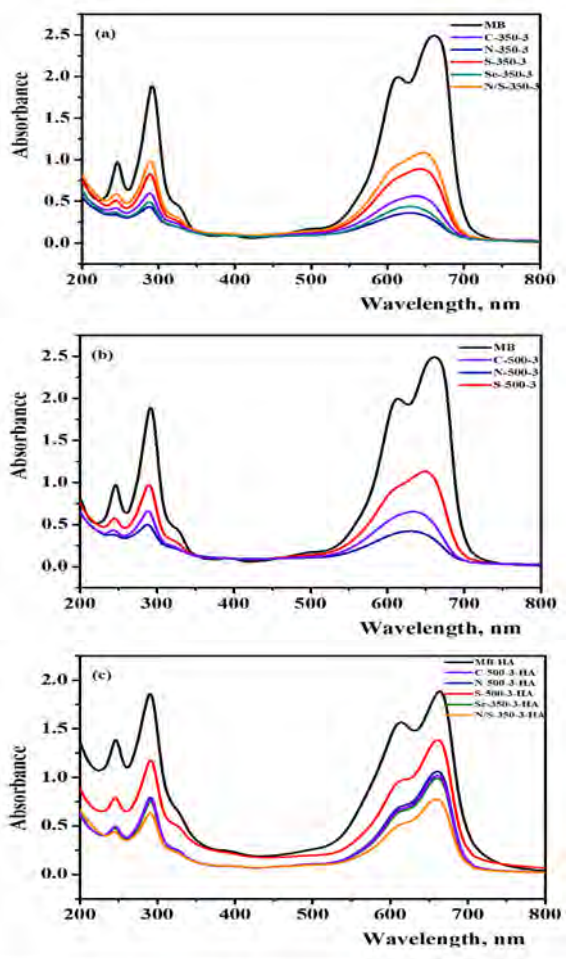

Figure 5. UV-vis spectra of MB dye solution by doped TiO_2 photocatalysts **(a)** 350°C 3h, **(b)** 350°C and 500°C h, **(c)** presence of HA.

Region IV and V were expressed by microbial byproducts and humic-like in the excitation wavelength region of λ_{exc}=250–470 nm with an emission wavelength region of λ_{emis}=280–380 nm and λ_{emis}=380–580 nm respectively [26].

In Fig. 6, EEM contour plots of HA and MB subsequent to photocatalysis of 60 min using doped-TiO_2 samples are shown. It is notable from the figure that humic-like features decreased in all spectra after 60 min irradiation, but the most significant changes were observed in the presence of N-TiO_2, C-TiO_2, and Se-TiO samples. The humic-like region was slightly decreased in S-TiO_2 and N/S-TiO_2 samples compared to anion doped TiO_2 samples.

CONCLUSION

In this study, C, N, S, Se doped and N/S codoped TiO_2 photocatalysts were prepared using wet-impregnation method. It was found that Se-350-3 and N-350-3 TiO_2 photocatalysts exhibited the highest removal of MB. The removal efficiency % was decreased in HA medium because of the retardation effect of HA on the photocatalytic system. In Raman spectra, any phase transformation from anatase phase to rutile phase was not observed due to different calcination temperature as expected. The results in Raman spectra confirmed that all doped TiO_2 photocatalysts exhibited anatase phase. In accordance with removal data, the change of EEM spectra with a decrease in intensity of the humic-like region was noticable after 60 min irradiation especially in anion doped TiO_2 photocatalysts.

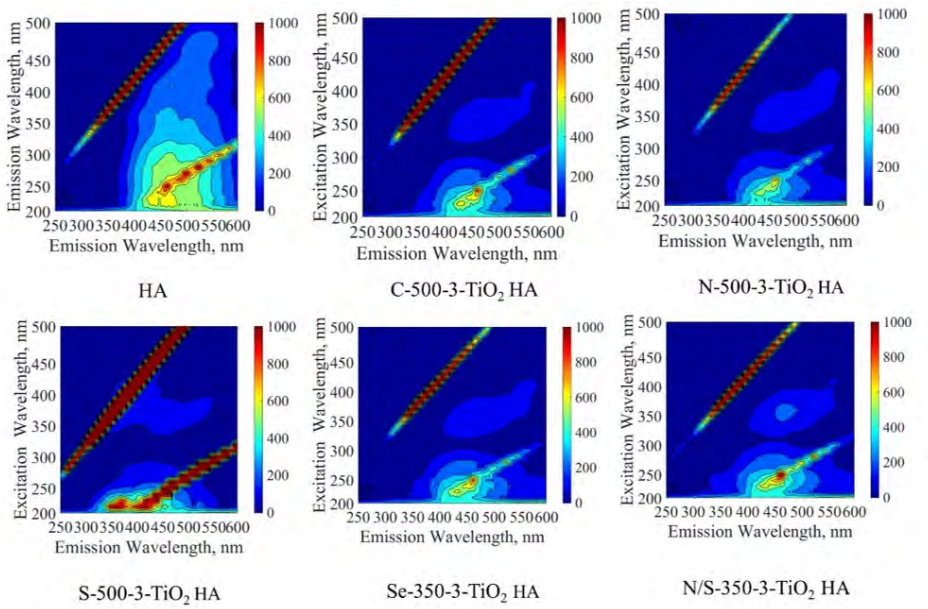

Figure 6. EEM contour plots of HA and MB with respect to irradiation 60 min using doped TiO_2.

ACKNOWLEDGEMENT

The authors express their thanks to Kirsehir Ahi Evran University Research Foundation for financial support (Project No. FEF.A4.19.009).

References

1. Aksakal O., Ucun H.. Equilibrium, kinetic and thermodynamic studies f the biosorption of textile dye (Reactive Red 195) onto Pinus sylvestris L.Journal of Hazardous Materials 181 (2010) 666-672.
2. Brillas E., Martínez-Huitle C.A. Decontamination of wastewaters containing synthetic organic dyes by electrochemical methods. An updated review, Applied Catalysis B: Environmental 166-167 (2015) 603-643.
3. Bora L.V., Mewada R.K. Visible/solar light active photocatalysts for organic effluent treatment: Fundamentals, mechanisms and parametric review, Renewable and Sustainable Energy Reviews 76 (2017) 1393-1421.
4. Byrne C., Subramanian G., Pillai S.C. Recent advances in photocatalysis for, environmental applications, Journal of Environmental Chemical Engineering 6 (2018) 3531-3555.
5. Pelaez M., Nolan N.T., Pillai S.C., Seery M.K., Falaras P., Kontos A.G., Dunlop P.S.M., Hamilton J.W.J., Byrne J.A., O'Shea K., Entezari M.H., Dionysiou D.D. A review on the visible light active titanium dioxide photocatalysts for environmental applications Applied Catalysis B: Environmental, 125 (2012) 331-349.
6. Srikanth B., Goutham R., Badri Narayan R., Ramprasath A., Gopinath K.P., Sankaranarayanan A.R. Recent advancements in supporting materials for immobilised photocatalytic applications in waste water treatment, Journal of Environmental Management, 200 (2017) 60-78.
7. Zangeneh H., Zinatizadeh A.A.L., Habibi M., Akia M., Hasnain Isa M. Photocatalytic oxidation of organic dyes and pollutants in wastewater using different modified titanium dioxides: A comparative review, Journal of Industrial and Engineering Chemistry, 26 (2015) 1-36.
8. Uyguner-Demirel C.S., Birben C.N., Bekbolet M. A comprehensive review on the use of second generation TiO2 photocatalysts: Microorganism inactivation, Chemosphere, 211 (2018) 420-448.
9. Farabegoli G., Chiavola A., Rolle E., Naso M. Decolorization of Reactive Red 195 by a mixed culture in an alternating anaerobic–aerobic Sequencing Batch Reactor, Biochemical Engineering Journal 52 (2010) 220-226.
10. Forgacs E., Cserháti T., Oros G. Removal of synthetic dyes from wastewaters: a review, Environment International 30 (2004) 953-971.
11. Martínez-Huitle C.A., Brillas E. Decontamination of wastewaters containing synthetic organic dyes by electrochemical methods: A general review, Applied Catalysis B:Environmental 87 (2009) 105-145.
12. Khaki M.R.D., Shafeeyan M.S., Raman A.A.A., Daud W.M.A.W. Application of doped photocatalysts for organic pollutant degradation - A review, Journal of Environmental Management 198 (2017) 78-94.
13. Birben N.C., Uyguner-Demirel C.S., Sen-Kavurmaci S., Gürkan Yelda Y., Türkten N., Kılıç M., Çınar Z., Bekbolet M. Photocatalytic Performance of Anion Doped TiO2 on the Degradation of Complex Organic Matrix, in:Journal of Advanced Oxidation Technologies 2016, pp. 199.
14. Birben N.C., Uyguner-Demirel C.S., Kavurmaci S.S., Gürkan Y.Y., Turkten N., Cinar Z., Bekbolet M. Application of Fe-doped TiO_2 specimens for the solar photocatalytic degradation of humic acid Catalysis Today, 281 (2017) 78-84.
15. Birben N.C., Uyguner-Demirel C.S., Sen-Kavurmaci S., Gurkan Y.Y., Turkten N., Cinar Z., Bekbolet M. Comparative evaluation of anion doped photocatalysts on the mineralization and decolorization of natural organic matter Catalysis Today, 240, Part A (2015) 125-131.
16. Turkten N., Cinar Z., Tomruk A., Bekbolet M., Copper-doped TiO_2 photocatalysts: application to drinking water by humic matter degradation, Environmental science and pollution research international, 36 (2019) 36096–36106.
17. Gurkan Y., Kasapbasi E., Turkten N., Cinar Z. Influence of Se/N codoping on the structural, optical, electronic and photocatalytic properties of TiO_2 Molecules, 22 (2017) 414.
18. Birben N.C., Tomruk A., Bekbolet M. The role of visible light active TiO_2 pecimens on the solar photocatalytic disinfection of E. coli, Environmental science and pollution research international, 24 (2017) 12618-12627.
19. Tan K.H. Humic Matter in soil and the environment: principles and controversies, Second Edition, CRC PressTaylor & Francis Group 6000, Broken Sound Parkway NW, Suite 300Boca Raton, FL, pp. 240.
20. Bassi A.L., Cattaneo D., Russo V., Bottani C.E., Barborini E., Mazza T., Piseri P., Milani P., Ernst F.O., Wegner K., Pratsinis S.E. Raman spectroscopy characterization of titania nanoparticles produced by flame pyrolysis: The influence of size and stoichiometry Journal of Applied Physics, 98 (2005) 074305.
21. Mathpal M.C., Tripathi A.K., Singh M.K., Gairola S.P., Pandey S.N., Agarwal A., Effect of annealing temperature on Raman spectra of TiO2 nanoparticles, Chemical Physics Letters, 555 (2013) 182-186.
22. Tian H., Ma J., Li K., Li J. Hydrothermal synthesis of S-doped TiO_2 nanoparticles and their photocatalytic ability for degradation of methyl, orange, Ceramics International 35 (2009) 1289-1292.
23. Lin C., Lin K.S. Photocatalytic oxidation of toxic organohalides with TiO2/UV: the effects of humic substances and organic mixtures Chemosphere, 66 (2007) 1872-1877.
24. Liu X., Yang Y., Shi X., Li K. Fast photocatalytic degradation of methylene blue dye using a low-power diode laser, Journal of Hazardous Material, 283 (2015) 267-275.
25. Yu X., Huang L., Wei Y., Zhang J., Zhao Z., Dai W., Yao B. Controllable preparation, characterization and performance of Cu_2O thin film and photocatalytic degradation of methylene blue using response surface methodology, Materials Research Bulletin 64 (2015) 410-417.
26. Sen-Kavurmaci S., Bekbolet M. Tracing TiO_2 photocatalytic degradation of humic acid in the presence of clay particles by excitation–emission matrix (EEM) fluorescence spectra, Journal of Photochemistry and Photobiology A:Chemistry, 282 (2014) 53-61.

Hittite Journal of Science and Engineering, 2020, 7 (2) 115-123
ISSN NUMBER: 2148-4171
DOI: 10.17350/HJSE19030000180

2D and 3D Positioning Performance of UAV-Based Photogrammetry in Residential Regions

Mehmet Nurullah Alkan[1] Kayhan Aladogan[1] Zafer Kose[1] Oyku Alkan[2]
[1]Hitit University, Osmancık Vocational School, Corum, Turkey
[2]Istanbul Technical University, Graduate School of Science Engineering and Technology, Istanbul, Turkey

ABSTRACT

UAVs (Unmanned Aerial Vehicles) are commonly used in photogrammetric observations in research fields like agriculture, archaeology, industry and construction of base maps. They present several advantages like low-cost platforms, rapid results, high positioning accuracy and less labor effort in the field.

In this study, we evaluate the positioning accuracy of UAV based photogrammetry with conventional observation techniques in a sample area. Our main motivation is to examine if the final model of a low altitude UAV can reach the positioning accuracy of conventional observation techniques, especially in residential regions. For this purpose, we evaluate the results of 3 separate photogrammetric flights in a pre-observed field. Results indicate that low-altitude UAV flights can provide high accuracy both in 2D and 3D positioning in residential and densely constructed areas.

Keywords:
UAV, Photogrammetry, GNSS, Terrestrial observations, SfM, Positioning accuracy.

Article History:
Received: 2020/02/17
Accepted: 2020/06/03
Online: 2020/06/26

***Correspondence to**: Mehmet Nurullah Alkan, Hitit University, Osmancik Vocational High School*
E-mail: nurullahalkan@hitit.edu.tr,
Phone: +90 532 432 9145,
Fax: +90 364 611 5030.

INTRODUCTION

Photogrammetry has been widely used for acquiring field data, which has much more better spatial resolution than remote sensing. Also, close range aerial photogrammetry by using unmanned platforms is a new concept considering other techniques and methods. Using that technique is mainly based on the necessity for low-cost and less labor applications. Aim is to extract geo-referenced information of the interested objects and/or regions in a wide range of data diversity by automated processing with the help of stereo aerial imagery [1-7].

Considering the aim and purpose, model from a UAV flight can procure accurate data in a wide range of small to large scaled projects (Fig. 1) [1, 4]. In this concept, requirement and applications of UAV photogrammetry vary from agriculture to forestry, archeology, geology and even specific activities like measurement of the tree heights for monitoring the development of the forestland, soil displacement and such civil engineering applications [1-6, 8].

Nowadays, there are several types of those UAV platforms (fixed or rotary wings, etc.) with mounted digital sensors for different purposes that allow to model ground truth by using multiple scene data in a short-time window. Also, UAVs for photogrammetric applications generally include a GNSS (Global Navigation Satellite System) sensor combined with an INS (Inertial Navigation System) unit for automatic take-off and landing, acquiring images, calculating precise position of the imagery sensor and certain parameters at the time of the photo-shoot. Those information are inputs for constitution of an accurate photogrammetric model of the scenery. UAV platforms generally have a mounted digital camera to acquire photos but in some cases, that camera type can be rearranged to have a LIDAR (Light Detection and Ranging) or multispectral image sensors according to the pre-determined conditions of the study [1, 3, 6, 9].

A UAV-based photogrammetric model is based on some certain steps like a flight trajectory plan, observation of common points (on the ground and images), creating a point cloud and constitution of 3D models, respectively. As a result, final outputs of a UAV flight can be used for creating ortho-images, digital terrain models, gathering metric information and even 3D mo-

del of the area. Another benefit of UAV platforms is that they can adopt to certain changes on the field because of their quick response time and model constitution [1, 3, 6, 10].

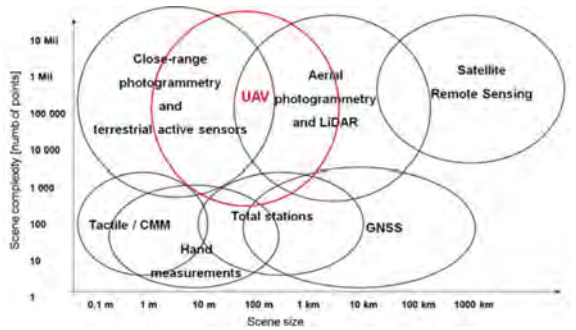

Figure 1. Available techniques and sensors for data acquisition and UAV based photogrammetric model in the manner of number of points in the point cloud and magnitude of the project area (from [1]).

METHODOLOGY FOR A UAV-BASED PHOTOGRAMMETRIC MODEL

Important variables should be considered before a UAV flight. Those are important parameters and may vary from scene to scene and should be adopted according to the analysis of the study area (Fig. 2):

- Aim of the project (emergency situation or precise model constitution),
- Required ground sampling distance (GSD) based on the subject,
- Size of the area,
- Flight trajectory and energy consumption of the platform,
- Overlap ratios for the photos [1, 5, 7-8, 11-13],
- Data process time.

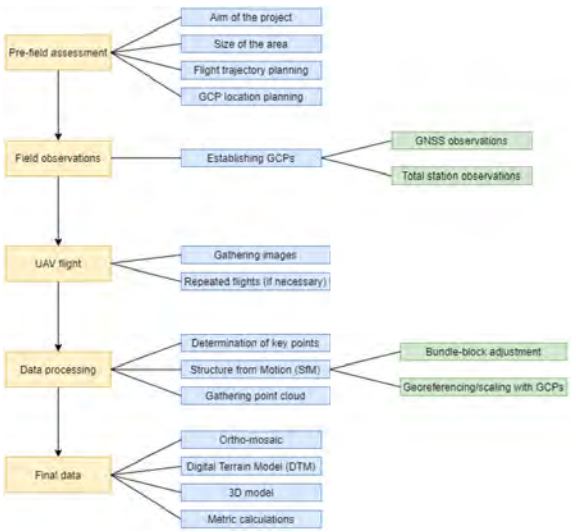

Figure 2. Workflow of a UAV based photogrammetry [2, 5, 14].

Those UAV-based photogrammetric models requires a pre-field study if the scenery information is essential with the ground coordinate system. That process is generally realized by using common points (Ground Control Points - GCPs) both available on the images and on the ground. A GCP is a pre- or post-observed point used for image transformation between image-ground coordinate systems, which can be defined as manual key points. Their coordinates can be estimated before or after the flight and can be chosen as distinct objects or can be manually established on the ground by the user [15]. General approach to acquire the position of the GCPs are related with RTK (Real-time kinematic) or network-based GNSS observations nowadays to increase the accuracy of the model. Later on the process, multiple GCPs are used for geo-referencing and scaling the mosaic overview of the interested area. But a more recent advance is to use a UAV with combined RTK-GNSS and INS modules which allows to estimate the coordinates of the photo-shoot point and orientation parameters on board [1, 5, 7, 10, 11, 16].

In general, main issue to acquire data from scene photos is to establish a correlation between the photo-plane and the ground truth and that can be realized by using GCP data. In the constitution of the final 3D model, all photos from the imagery sensor evaluated together by using bundle-block adjustment, which can eliminate systematic errors with the help of a minimum number of GCPs on the scene. That step includes a coordinate transformation and there should be at least 3 known points at both images and the ground to gather information later from the photos. The number of GCPs can be increased if the elevation of the region has abrupt changes [1, 4, 5, 11, 17].

For traditional photogrammetry, the link between those coordinate systems requires parameters such as interior orientation values for the camera (calibration report) and

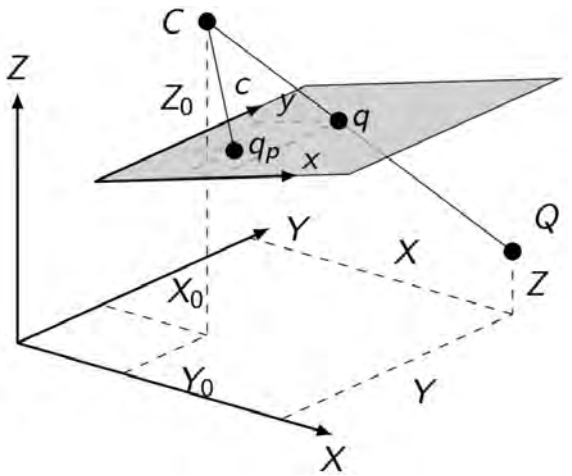

Figure 3. Relationship between a ground point (Q), camera center (C) and the orientation of the photo plane regarding the terrestrial coordinate system [18].

certain features (GCPs) both visible and observable on the image and on the ground for the exterior orientation variables [1, 5, 11] (Fig. 3).

It can be derived from Fig. 3 that XYZ axes are the ground coordinate system and xy axes are photo plane system. Also, c represents the principal distance, q_p is the principal point and X_0, Y_0, Z_0 are the coordinates of the camera center in terrestrial coordinate system [18]. Regarding the position of the camera and its orientation, the collinearity equation can be written as follows:

$$x - x_p = -c\frac{r_{11}(X - X_0) + r_{21}(Y - Y_0) + r_{31}(Z - Z_0)}{r_{13}(X - X_0) + r_{23}(Y - Y_0) + r_{33}(Z - Z_0)} \quad (1)$$

$$y - y_p = -c\frac{r_{12}(X - X_0) + r_{22}(Y - Y_0) + r_{32}(Z - Z_0)}{r_{13}(X - X_0) + r_{23}(Y - Y_0) + r_{33}(Z - Z_0)} \quad (2)$$

In the equation:

- x, y : Coordinates of the image point (q)
- X, Y, Z : Coordinates of the ground point (Q)
- x_p, y_p : Coordinates of the principal point
- X_0, Y_0, Z_0 : Coordinates of the camera center in terrestrial coordinate system
- $r_{11} - r_{33}$: Angular orientation matrix along 3 axes between photo-ground coordinate system [11, 19].

However, with a bundle-block adjustment approach, all required parameters can be computed automatically with high precision. That procedure is known as "Structure from Motion (SfM)", an automated model constitution from images, and such software solutions can combine SfM with bundle-block effectively. That allows using multiple imagery from different platforms and does not require specific camera orientation parameters or precise position [1, 11, 5, 14, 8, 20].

The next step, image assessment, involves the analysis of every image from the scene and estimating the common features or points to link and chain all data. That is established by calculating the camera positions and orientation parameters for each image simultaneously which is derived from SfM approach. Point cloud data in that stage does not have a scale or orientation, but that procedure is completed by using a minimum number of GCP variables [5, 7-8].

The final output of a UAV-based photogrammetric model generally includes an ortho-mosaic view of the scene and a 3D model which may used for metric calculations such as distance, volume, base map construction, etc. Accuracy of the constructed photogrammetric model may vary, but is up to centimeter-decimeter level according to the scenery variables(flight altitude, camera specifications, etc.). Such regulations limit the position accuracy to a certain level, but necessary precision can be derived by a UAV model [1, 6-9, 14, 21].

MATERIAL AND METHODS

Model Area

In this study, the research area is located in the Osmancık campus of Hitit University in Çorum, which consists of a main building with two playfields, recreational areas and parks. Vegetation is sparse considering wood density and area is suitable for both geodetic observations and UAV flights, with no significant flight obstacles around. Campus area is about 0.05 km^2 in total and land elevation ranges between ~420 – 445 m. That gives a height difference roughly above 20 m and 5% slope at its maximum, thus the area can be defined as low-pitched (Fig. 4).

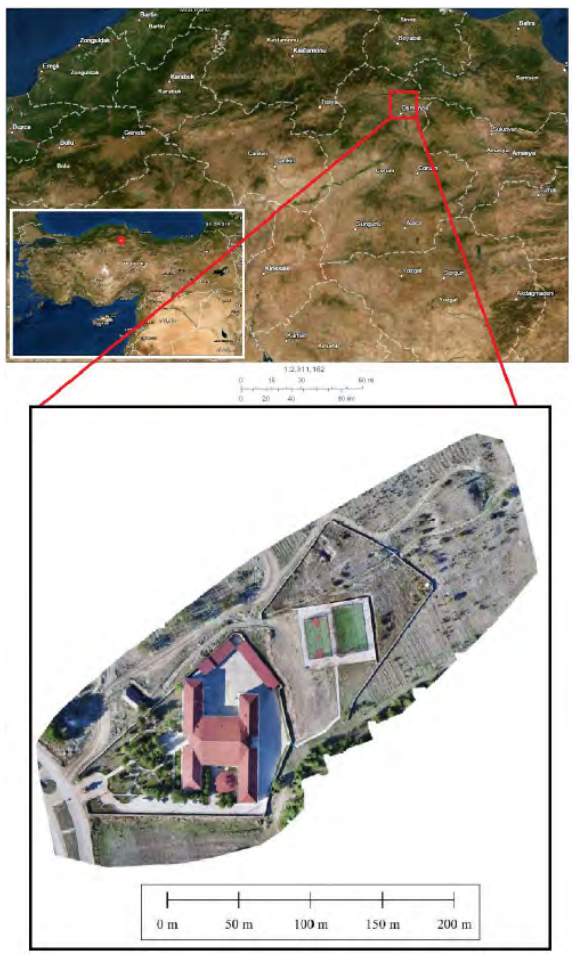

Figure 4. Location of the study area and Hitit University Osmancık campus general overview (after [22]).

We focused on the main structure at the center of the campus. That is a double-floored concrete building and has a height around 7 m, but it is not a classical 4-cornered building. It looks like a tilted "H" and has deep corners. We

Figure 5. Main building of the campus from the parking lot at the north side. Fringe(yellow) and one of the deep corners(blue) are marked on the figure.

established two different field observations to acquire the field data for the characteristic points of that structure. First one is the terrestrial observations (joint GNSS and angle-distance surveying) and the second one is based on 3 different photogrammetric model flights with different altitudes. After acquiring the coordinates of characteristic points with two different methods, we made an evaluation considering both results (Fig. 5).

Data Acquisition

Terrestrial Observations

There are 9 benchmarks established on the field and geodetic observations are based on those points (Fig. 6). Location data for all the corners of the main building is derived using GNSS and total station observations, respectively. Because, obstacles are covering the open sky view (mainly caused by the building and fringes) and make it almost impossible to estimate the coordinates of the structure by GNSS observations.

At first, we used a Spectra SP80 GNSS receiver for 2 sessions to calculate the average coordinates of the benchmarks in the area. After that, we conducted observations

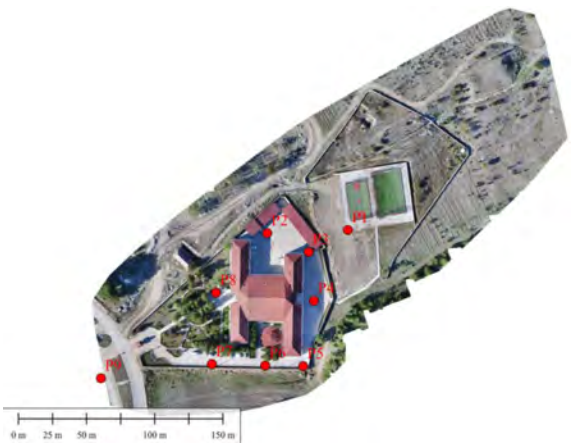

Figure 6. Location of the benchmarks used in data acquisition of the main structure in the campus with terrestrial observations.

Figure 7. Main structure at the center of the campus from above. 12 red dots are regular corners (C), and 8 white dots are deep corners (DC).

with a total station for final 3D coordinate acquisition of the building's characteristic points. The specifications of GNSS device and the observations are given at Table 1.

The locations of the benchmarks which are based on the network-RTK observations are given in Fig. 6. GNSS observations on those points completed by using TUSAGA-Aktif, a continuously operating GNSS network. It has 158 control points all around Turkey and allows the GNSS receivers to obtain real-time coordinates of any point on the terrain which has open sky view for satellite transmissions [24]. The positioning accuracy of the real-time GNSS observations are below ±3 cm in horizontally and ±5 cm vertically while using this network [25-26].

We concentrated our observations on the main building's corners and deep corners. Moreover, we acquired a total of 20 points' coordinates (Fig. 7). We used the benchmarks at appropriate locations around the structure with a Spectra Focus 8 total station. That device has a 2" angle and (2 mm ± 2 ppm) distance precision and suitable for data acquisition and the construction of base maps [27]. We used that device because it also has the capability to make observations using a laser beam without a reflector and allow direct targeting to the interested points (corners of the structure) which eliminates the offset error. Thus, data acquisition for interested points were mainly based on the combined angle and the distance measurements with that instrument.

Photogrammetric Data Acquisition

We used a DJI Phantom 4 Pro UAV for photogrammetric model construction, which has a 20 M resolution camera with 1" CMOS, the ability to take-off/land vertically and a Satellite Positioning System that works with both GPS (Global Positioning System) and GLONASS (Global Navigation Satellite System) [28].

Table 1. Specifications of the GNSS receiver and observation limitations [23]. Used GNSS satellites are marked with (*).

Receiver type	*Spectra SP80 Multi-frequency GNSS receiver (compatible with GPS*, GLONASS*, BeiDou, Galileo, QZSS, SBAS, IRNSS)*					
Precision in Network RTK	*8 mm ± 0.5 ppm horizontal*			*15 mm ± 0.5 ppm vertical*		
Satellite cut-off angle	*10°*					
Number of epochs for both sessions/point	*20*					
Epochs/second	*1*					
Gap between sessions	*>1 hour*					
Final coordinates	*Average coordinates of 2 sessions*					
Datum	*ITRF96*	*Mean meridian*	*36*		*Zone width*	*3°*
Ellipsoid	*GRS80*	*Reference epoch*		*2005.0*		
Observation mode	*Network RTK (VRS)*	*Connected network*		*TUSAGA-Aktif*		

We evaluated the field data with Pix4D software and it is advised that there should be well-distributed 5-10 GCPs in the working area by the manufacturer [5, 17]. Thus, before the flight, we established 6 temporary GCPs around the sampling area according to that initial information. The locations of GCPs are selected to have a normal distribution on the field as far as possible which might have a great influence on the accuracy of whole model [8, 14]. The coordinates of those points were acquired by using Spectra SP80 GNSS receiver with network-RTK method and their locations and ground materials are given at Figs. 8 and 9.

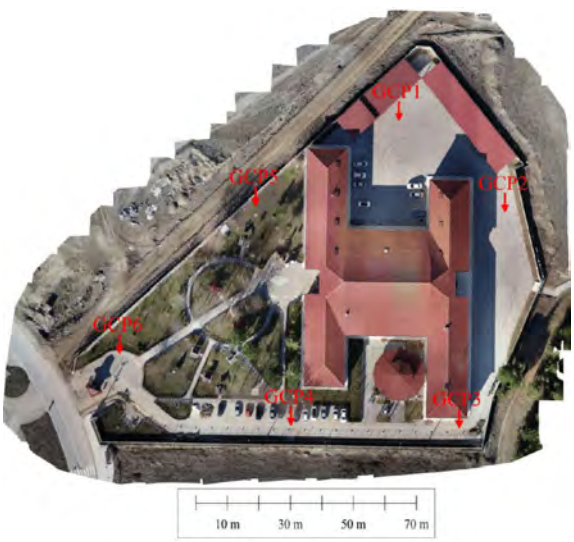

Figure 8. Location of the GCPs around the model area.

Figure 9. One of the temporary GCPs established on the ground for each flight. Image on the left is from actual photo of the feature and the right one is obtained from densified point cloud.

We conducted 3 different flights at different altitudes and selected different side and front overlaps for each trajectory (Table 2).

Table 2. Front and side overlap ratios for 3 different flight altitudes of the UAV.

Flight No	*Height*	*Front overlap*	*Side overlap*	*Number of photos*
1	*30 m*	*90%*	*70%*	*500*
2	*45 m*	*80%*	*70%*	*111*
3	*60 m*	*80%*	*70%*	*65*

1st flight's front overlap ratio differs from the other flights due to the improper photo-shoot point of the UAV at deep corners. There should be at least 2 photos for each corners to estimate actual coordinates, however, at 30 m height with lower front overlap (80%), that condition did not match due to the flight trajectory of the UAV. Thus, we increased the front overlap ratio to 90% for that altitude (Fig. 10).

A drawback with photogrammetric flight plan occurs that the main construction in the campus has deep corners which makes them hard to observe from all angles at the flying altitudes of the UAV. Additionally, the building has a low fringe height (~6 m). This is another drawback for data acquisition because they can completely or partially block the view of the flying platform due to improper photo-shoot point/flight plan, height or front/side overlap ratios of the UAV. Thus, we rearranged the flying trajectories and altitudes to eliminate those concerns.

We evaluated the final data with Pix4D software, which uses the photos from UAV and GCP data as input within several steps, based on aerial triangulation and bundle block adjustment [1, 29]. Results of the Pix4D process for each flight are given at the Table 3.

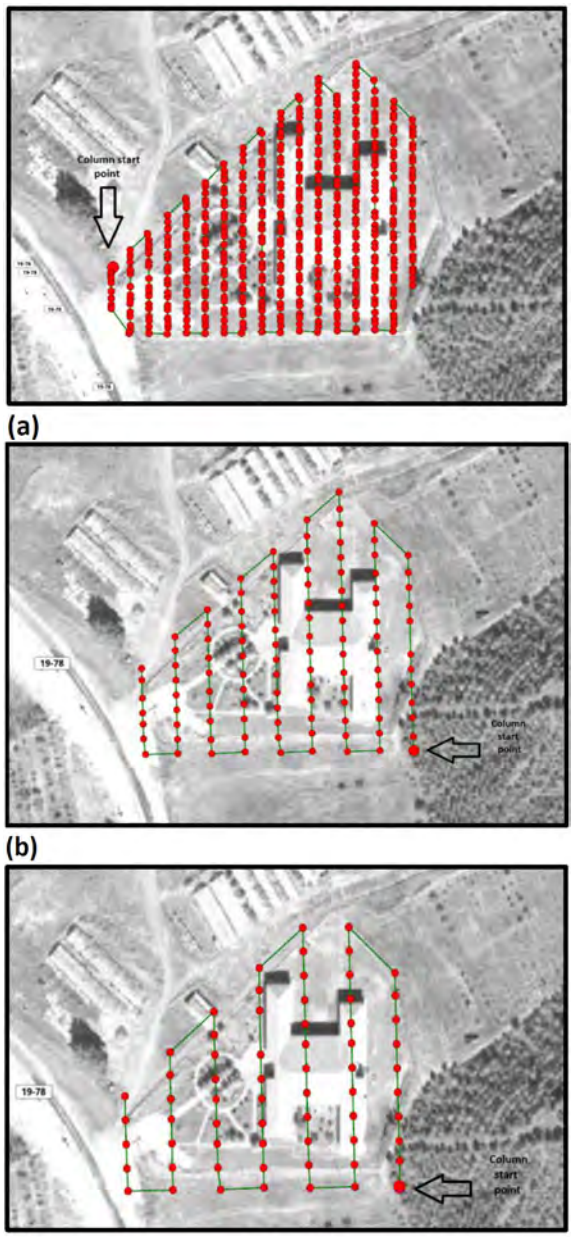

Figure 10. Flight plan for 3 different altitudes, (a) 30 m, (b) 45 m, and (c) 60 m, respectively. Red dots represents every photo-shoot point of the UAV during the flight and green lines indicates the trajectory of the platform.

Table 3. Pix4D processing results for 3 flight plans.

Flight No	*30 m flight*	*45 m flight*	*60 m flight*
Average Ground Sampling Distance (GSD)	*0.71 cm*	*1.12 cm*	*1.53 cm*
Model Area	*0.020 km²*	*0.027 km²*	*0.031 km²*
Number of images/ calibrated images	*500/500*	*111/111*	*65/65*
Error for GCPs georeferencing (mean RMS)	*0.011 m*	*0.012 m*	*0.012 m*
Mean reprojection error for Bundle Block Adjustment	*0.164 pixel*	*0.161 pixel*	*0.16 pixel*

After the full process of each flight, the characteristic points of the main structure were digitized using Pix4D interface and coordinates were acquired for further evaluation. There is a total of 20 points from the terrestrial observations and they were all matched with the Pix4D digitizing process.

At this phase, the corners are more visible in the photos (5-31 photos) then the deep corners (2-8 photos) as expected (Table 4&5), but visibility highly depends on the environmental conditions. In order to produce coordinate data from the photogrammetric model, all corners should be observed from at least 2 photos. Considering the flights, all corners are visible and match that condition. However, from three different models, we evaluated that fringes, improper photo-shoot position of the UAV, vegetation, sun light reflection on the white edges and even shadows prevent a clear view and digitizing of the characteristic points of the structure (Figs. 11 and 12). But those obstacles were obviated by using multiple photos of the interested points.

Table 4. Characteristic points of the building and their visible number of photos from different altitude UAV flights (C: corner, DC: deep corner).

Point No	*Visible in number of photos*		
	30 m flight	*45 m flight*	*60 m flight*
C1	*17*	*5*	*5*
C2	*31*	*11*	*11*
C3	*25*	*13*	*12*
C4	*24*	*9*	*8*
C5	*24*	*8*	*7*
C6	*24*	*8*	*7*
C7	*8*	*8*	*6*
C8	*15*	*9*	*10*
C9	*31*	*12*	*14*
C10	*16*	*7*	*7*
C11	*20*	*9*	*8*
C12	*22*	*9*	*10*
DC1	*6*	*4*	*4*
DC2	*6*	*4*	*4*
DC3	*6*	*4*	*2*
DC4	*7*	*3*	*2*
DC5	*6*	*2*	*3*
DC6	*4*	*4*	*2*
DC7	*8*	*4*	*4*
DC8	*6*	*6*	*5*

Table 5. Average number of photos for each flight.

	30 m flight	*45 m flight*	*60 m flight*
Average number of photos for corners (C)	*21.4*	*9.0*	*8.8*
Average number of photos for deep corners (DC)	*6.1*	*3.9*	*3.3*
Number of photos for DC/C	*0.29*	*0.43*	*0.37*
Overall number of photos for DC/C		*0.36*	

Figure 11. Challenges acquiring data from photogrammetric model. Shadow of the manmade structures and/or vegetation may prevent a proper positioning. At DC5, shadow of vegetation around the corner partially block the view and makes it harder to assess the actual location. Green cross represents the estimated location and yellow circle is the error estimation for the point.

Figure 12. Challenges acquiring data from photogrammetric model. At C12, color of the building over-radiated at the time of photoshoot and may lead to a poor positioning assessment. Green cross represents the estimated location and yellow circle is the error estimation for the point.

The coordinates of the characteristic points of the interested structure were all estimated by before mentioned methods. Thus, we finally had 1 set of data from terrestrial observations and 3 sets of data from 3 different photogrammetric models for further evaluation.

RESULTS AND DISCUSSION

We interpreted final data in the manner of location accuracy and evaluated every photogrammetric model results separately with terrestrial observations in 2D and 3D (Table 6 and 7).

Results indicate that the position differences ranges between 0.005 – 0.138 m in 2D and 0.02 – 0.181 m in 3D, considering all flights. In addition, the maximum positioning error at 60 m altitude is greater than other flights in 2D and 3D positioning and those differences occur especially at deep corners. At points DC1, DC3, DC4, DC5 and DC6 for 60 m flight, 2D and 3D positioning errors are roughly above a decimeter. Considering Table 4, those corners are visible only from 2 – 4 aerial photos, thus that might lead to estimate the position of the point poorly [5]. We evaluated that those certain errors may arise from certain features such as higher flight altitude and/or lower resolution due to that trajectory. However, considering overall performance of all photogrammetric models, there is no significant difference

Table 6. Cross-validation of coordinate differences at each point between terrestrial observations and photogrammetric model results (C: corner, DC: deep corners).

	30 m		45 m		60 m	
Point No	2D pos. dif.(m)	3D pos. dif.(m)	2D pos. dif.(m)	3D pos. dif.(m)	2D pos. dif.(m)	3D pos. dif.(m)
C1	0.068	0.073	0.056	0.060	0.090	0.090
C2	0.030	0.034	0.037	0.037	0.011	0.016
C3	0.035	0.068	0.027	0.028	0.020	0.020
C4	0.035	0.045	0.026	0.032	0.009	0.017
C5	0.057	0.058	0.058	0.068	0.091	0.091
C6	0.037	0.068	0.023	0.067	0.024	0.031
C7	0.018	0.045	0.009	0.054	0.013	0.052
C8	0.014	0.036	0.014	0.034	0.029	0.068
C9	0.020	0.038	0.021	0.024	0.024	0.066
C10	0.046	0.082	0.049	0.052	0.037	0.068
C11	0.050	0.056	0.059	0.068	0.042	0.060
C12	0.024	0.060	0.024	0.025	0.041	0.062
DC1	0.009	0.020	0.005	0.036	0.069	0.111
DC2	0.029	0.057	0.042	0.048	0.020	0.026
DC3	0.085	0.092	0.054	0.074	0.138	0.181
DC4	0.057	0.088	0.036	0.076	0.080	0.120
DC5	0.045	0.094	0.027	0.090	0.115	0.131
DC6	0.061	0.093	0.052	0.056	0.093	0.111
DC7	0.014	0.085	0.027	0.043	0.025	0.043
DC8	0.042	0.048	0.029	0.040	0.008	0.017

Table 7. Statistics for each flight considering terrestrial observations.

	30 m model		45 m model		60 m model	
	2D	3D	2D	3D	2D	3D
Min. (m)	0.009	0.02	0.005	0.024	0.008	0.016
Max. (m)	0.085	0.094	0.059	0.09	0.138	0.181
Mean (m)	0.039	0.061	0.034	0.051	0.049	0.069
RMS. (m)	0.045	0.066	0.038	0.055	0.064	0.084

in mean error in 2D (0.039 – 0.049 m) and in 3D (0.051 – 0.069 m) and in the manner of RMS in 2D (0.038 – 0.064 m) and in 3D (0.055 – 0.084 m).

RMS values for each flight at Table 7 indicates the standard deviation of the residuals for the positioning of each point. That might give us an overlook for the results in general.

Values are below 0.07 m in 2D and 0.09 m in 3D positioning for all flights. These can be considered as statistically valid if the positioning errors are in a predefined limit. For that reason, there should be some limitations and regulations to eliminate the error sources and take the results to a certain confidence level. Considering the construction of base maps, in specific, Turkey has strict rules for that purpose [21]. After completing a photogrammetric model, values derived from it, can be controlled in such ways to find out the consistency of the observations. General process for that

purpose is established by comparing the photogrammetric results with terrestrial observations (GNSS, etc.). Actually, we have conducted that condition in our study.

While controlling our model accuracy, we used Table 6 as an outcome. According to the regulations in Turkey, coordinates of a certain percentage of detail points in a base map, derived by photogrammetry, should be controlled or compared by GNSS or total station observations. That process includes 2D position and height differences separately and leads the photogrammetric model to offer certain errors below those limits:

$$RMS_{X,Y} < \pm\left(-1,665\times10^{-6}\times S^2 + 0,01745\times S - 1,166\right) \quad (3)$$

$$RMS_Z < \pm RMS_{X,Y}\times 1,33 \quad (4)$$

where S is the denominator of the scale of the base map [21]. Considering the equations above, RMS values can be calculated for a 1/500 scale base map as ±0.071 m and ±0.095 m, respectively. From Table 7, derived RMS values for each flight are below those calculated limitation values in both 2D and 3D positioning. Our photogrammetric models have positioning errors, but according to the results, they can supply adequate accuracy comparable with terrestrial observations. And considering the RMS values derived in this study, a photogrammetric survey model can offer high accuracy during the construction of base maps; not in only rural areas, but also in highly populated/constructed zones.

On the other hand, there is no clear evidence for an improvement in positioning when we lowered the flight altitude from 45 m to 30 m. Additionally, 45 m flight gives better performance than 30 m in this study for mean error (0.051 m/0.061 m) and RMS (0.055 m/0.066 m) values at their maximum. That might indicate that lowering the flight altitude may not contribute a significant difference in photogrammetric modeling in every situation.

In this study, we evaluated 500, 111, and 65 photos for 30 m, 45 m and 60 m flights, respectively. That is an important issue while planning the photogrammetric model because there should be much more photos with lowering the flight altitude. That concludes a significant increase in both flight and software processing time and might be an important issue if the final data is crucial in a short time window.

Main issue in this study was to estimate the proper locations of the deep corners. They are visible from a minimum number of photos considering regular corners and data acquisition might lack of accuracy at those points. During our UAV flights, we evaluated that the deep corners can only be observed with less then ~36% view angle from the sky (Table 5). Thus, for gathering full view of every structure corners, we recommend increasing the side and front overlap ratios during the flight or widening the model area with longer flight trajectory. By that way, UAV can have more photo-shoot points while advancing through the edges of the flight trajectory. Although our study area is not in a highly populated region, one might notice that this condition might emerge in every residential territory which has squeezed constructed regions.

During this study, we planned the altitude of the UAV almost 4, 6 and 8 times of the interested building height (~7 m). Heights of the structures might differ at different regions, but if there are certain features which has deep corners like our study, we recommend the flight altitude to not exceed ~45 m for a UAV flight on the field, if the specifications of the device is similar to ours [28].

In addition, positioning accuracy might depend strongly in some conditions, such as over radiated corners due to sunlight or view block by vegetation or their shadows. Our study conducted under those circumstances and we recommend to choose flight time-window during shorter shadows and lower vegetation if possible.

In conclusion, all the results indicate that UAV photogrammetry can provide high positioning accuracy as far as terrestrial observations. That condition might occur even in a highly populated and/or constructed regions while producing base maps and can reach to a centimeter and roughly decimeter level accuracy in 2D and 3D data acquisition.

References

1. Nex F, Remondino F. UAV for 3D mapping applications: a review. Applied Geomatics 6 (2014) 1–15.
2. Krause S, Sanders TGM, Mund JP, Greve K. UAV–based photogrammetric tree height measurement for intensive forest monitoring. Remote Sensing 11 (2019) 758.
3. Akturk E, Altunel AO. Accuracy assessment of a low–cost UAV derived digital elevation model (DEM) in a highly broken and vegetated terrain. Measurement 136 (2018) 382–386.
4. Barba S, Barbarella M, Benedetto AD, Fiani M, Limongiello M. Quality assessment of UAV photogrammetric archaeological survey. International Archives of the Photogrammetry, Remote Sensing and Spatial Information Sciences XLII(2)/W9 (2019) 93–100.
5. Bemis SP, Micklethwaite S, Turner D, James MR, Akciz S, Thiele ST, Bangash HA. Ground–based and UAV–based photogrammetry: a multi–scale, high resolution mapping tool for structural geometry and paleoseismology. Journal of Structural Geology 69 (2014) 163–178.
6. Uysal M, Toprak AS, Polat N. DEM generation with UAV photogrammetry and accuracy analysis in Sahitler Hill. Measurement 73 (2015) 539–543.
7. Fernandez T, Perez JL, Cardenal J, Gomez JM, Colomo C, Delgado J. Analysis of landslide evolution affecting olive

groves using UAV and photogrammetric techniques. Remote Sensing 8 (2016) 837.
8. Tomastík J, Mokros M, Salon S, Chudy F, Tunak D. Accuracy of photogrammetric UAV–based point clouds under conditions of partially–open forest canopy. Forests 8(5) (2017) 151.
9. Eisenbess H, Sauerbier M. Investigation of UAV systems and flight modes for photogrammetric applications. The Photogrammetric Record 26(136) (2011) 400–421.
10. Jiang S, Jiang W, Huang W, Yang L. UAV–based oblique photogrammetry for outdoor data acquisition and offsite visual inspection of transmission line. Remote Sensing 9 (2017) 278.
11. Dominici D, Alicandro M, Massimi V. UAV photogrammetry in the post–earthquake scenario: case studies in L'Aquila. Geomatics, Natural Hazards and Risks 8(1) (2017) 87–103.
12. Franco CD, Buttazzo G. Coverage path planning for UAVs photogrammetry with energy and resolution constraints. Journal of Intelligent & Robotic Systems 83 (2016) 445–462.
13. Cabreira TM, Franco CD, Ferreira Jr PR, Buttazzo GC. Energy–aware spiral coverage path planning for UAV photogrammetric applications. IEEE Robotics and Automation Letters 3(4) (2018) 3662–3668.
14. Martinez–Carricondo P, Agüera–Vega F, Carvajal–Ramirez F, Mesas–Carrascosa FJ, Garcia–Ferrer A, Perez–Porras FJ. Assessment of UAV–photogrammetric mapping accuracy based on variation of ground control points. International Journal of Applied Earth Observation and Geoinformation 72 (2018) 1–10.
15. Gonçalves JA, Henriques R. UAV photogrammetry for topographic monitoring of coastal areas. ISPRS Journal of Photogrammetry and Remote Sensing 104 (2015) 101–111.
16. Chudley TR, Christoffersen P, Doyle SH, Abellan A, Snooke N. High–accuracy UAV photogrammetry of ice sheet dynamics with no ground control. The Cryosphere 13 (2019) 955–968.
17. https://www.pix4d.com/blog/GCP–accuracy–drone–maps (last visited: 10.02.2020).
18. https://www8.cs.umu.se/kurser/5DV115/VT14/handouts/fundamentals_of_photogrammetry.pdf (last visited: 10.02.2020).
19. Zhang C, Yao W. The comparisons of 3D analysis between photogrammetry and computer vision. Paper Presented at XXIst ISPRS Congress Technical Commission III, Beijing, 3–11 July, pp. 33–36, 2008.
20. https://support.pix4d.com/hc/en–us/articles/205327965–Menu–Process–Processing–Options–1–Initial–Processing–Calibration (last visited: 10.02.2020).
21. https://www.hkmo.org.tr/resimler/ekler/466222ca92eaecb_ek.pdf (last visited: 10.02.2020).
22. www.arcgis.com (last visited: 10.02.2020).
23. http://trl.trimble.com/docushare/dsweb/Get/Document–844535/SG–SP80–Br–v2.pdf (last visited:10.02.2020).
24. https://www.tusaga–aktif.gov.tr/Sayfalar/IstasyonKonumBilgileri.aspx (last visited: 10.02.2020).
25. Aykut NO, Gülal E, Akpinar B. Performance of single base RTK GNSS method versus network RTK. Earth Sciences Research Journal 19(2) (2015) 135–139.
26. https://www.tkgm.gov.tr/sites/default/files/icerik/ekleri/tusaga–aktif_2018.pdf (last visited: 10.02.2020).
27. Spectra Precision Focus 8 total station user manual
28. https://www.dji.com/phantom–4–pro (last visited: 10.02.2020).
29. https://support.pix4d.com/hc/en–us/articles/205327965–Menu–Process–Processing–Options–1–Initial–Processing–Calibration (last visited: 10.02.2020).

Hittite Journal of Science and Engineering, 2020, 7 (2) 125-134
ISSN NUMBER: 2148-4171
DOI: 10.17350/HJSE19030000181

A Novel Navigation Algorithm for Mapping Indoor Environments with a Quadrotor

Omer Oral[1] Ali Emre Turgut[1] Kutluk Bilge Arikan[2]
[1]Middle East Technical University, Department of Mechanical Engineering, Ankara, Turkey
[2]TED University, Department of Mechanical Engineering, Ankara, Turkey

ABSTRACT

In the last decade, unmanned aerial vehicle gained popularity and started to be used in different tasks most of which are performed in outdoor environments. Still, there is a great potential to use quadrotors in indoor tasks such as urban relief and disaster operations. In this paper, we developed a framework and a novel target-based navigation algorithm for mapping of an unknown 2D environment with a quadrotor using an ultra-wideband system. The target-based navigation algorithm aims to explore map of the environment by moving the border between the discovered and undiscovered areas. It uses A* search algorithm for path planning if there is an obstacle present in the environment. The target-based navigation algorithm is implemented on Gazebo simulator and its performance is compared with the well-known wall following algorithm and exploration algorithm in terms of task completion time and distance travelled. The target-based navigation algorithm outperforms the other two algorithms especially in environments with obstacles.

Article History:
Received: 2020/03/04
Accepted: 2020/05/22
Online: 2020/06/26

***Correspondence to**: Omer Oral,*
Middle East Technical University,
Department of Mechanical Engineering,
06800, Ankara, TURKEY
E-mail: omroral@gmail.com

Keywords:
LIDAR; SLAM; Mapping; UWB; Trilateration technique; Quadrotor; UAV; Indoor; Obstacle avoidance.

INTRODUCTION

Recently, quadrotors gained popularity due to their high maneuverability, cost and vertical take-off/landing capabilities. Nevertheless, they also have disadvantages such as they have a limited flight time and small payload capabilities. In addition to these, a major part of the energy of a quadrotor is spent against gravity for hovering. Still, they are one of the most adopted air vehicles for commercial and research purposes. Most of the time UAV's (Unmanned Aerial Vehicles) are used in outdoor applications such as surveillance, search/rescue and patrolling. Recently, UAV's started to find uses in indoor environments. Material handling in manufacturing and inspection in harsh environments are to name a few[1] of these applications. One of the most promising applications is to utilize them in urban relief and disaster operations where a UAV moves autonomously avoiding obstacles in GPS-denied buildings to help human operators for rescue operations.

In order to navigate in an indoor environment, a map of the environment is needed. However, in most of the cases either the map is unknown or some partial information about the environment is available. Indoor mapping process can be performed by using several methods. SLAM technique is usually employed for mapping. SLAM (Simultaneous Localization and Mapping) is the process of simultaneous map extraction and robot localization. The difficulty of this process is inherent in its definition. A map is required for correct localization, while an accurate localization is required for mapping [2]. In indoor environments, ground-based robots were commonly employed for map extraction [3]. In studies with ground robots, while LIDAR (Laser Imaging Detection and Ranging) and IMU (Inertial Measurement Unit) were mostly used, Omara et al. [4] used a Kinect sensor for exploration and mapping of the environments using SLAM methods. Different sensors were utilized when UAV's were used for mapping. John son [5] used IMU, optic flow sensors and a camera to navigate autonomously in indoor environments. Due to unreliable attitude estimations with inertial sensors, Hough transform was adopted for attitude estimation of the quadrotor. Ahrens et al. [6] also used a quadrotor equipped with IMU and a camera to navigate in indoor environments with obstacles. They used "good features to track" detector for feature tracking and use these features for navigation and mapping. Roberts et al. [7] developed a quadrotor capable of navigating in indoor environments autonomously using and IMU, an ultra-

sonic sensor and four infrared sensors. The system managed to fly indoors with success. Mohamed et al. [8] proposed an indoor navigation system to estimate the position and orientation of the UAV. In this system, three laser diodes were integrated to the body of the UAV and they generate three dots on the ground. These dots were captured by the camera and their coordinates were determined using Scale Invariant Feature Transform algorithm, hence the position and orientation of the UAV were determined. Achtelik et al. [9] developed a method for autonomous navigation and exploration in indoor environments. They used an odometry algorithm with Extended Kalman Filter to estimate the position of the quadrotor and they employed a SLAM algorithm and a mission planner for building the map of the environment. Parallel to Achtelika's work, Grzonka et al. [10] performed mapping and exploration tasks using a UAV, an IMU and a LIDAR. A mirror was used to reflect laser beams to the ground and height of the air vehicle was determined accordingly. Wang et al. [11] presented a method for navigation and control for a UAV operating in an indoor environment. The quadrotor was equipped with an IMU, a downlooking camera, a barometer for height measurement, and a LIDAR to get distance information. The robot was able to estimate its position and velocity using Kalman filter, and fly in the room without colliding any walls. Wall following was used for navigation.

In the studies discussed so far, IMU and LIDAR were mostly used for localization. However, in some recent studies, wireless localization systems started to be employed. One of the widely used wireless localization technology for indoor environments is the UWB(Ultra-wideband) systems. UWB is an old radio technology used for short-range wireless communication that utilizes frequencies from 3.1 to 10.5 GHz and supports a bandwidth of 500 MHz. Due to its high bandwidth, very high data rates can be achieved with UWB systems. The only drawback of UWB is its limited communication range. Recently, due to the advances in technology, UWB is started to be used for real-time localization and tracking of objects in indoor environments by making time of flight measurements. In UWB-based localization, trilateration technique is used where a UWB tag is placed on the robot and at least three UWB anchors are placed at known positions in the environment [12]. In this way, the robot calculates its position with respect to the anchors [13,14]. UWB-based localization systems are capable of detecting robots with a 10 cm accuracy that are moving at a speed of 20 km/h. Barral et al. [15] developed a system for tracking forklifts using UWB technology in an indoor environment. They tested various real world scenarios on Gazebo simulator by defining different modes of operation.

The aim of this paper is to develop a framework and propose a method to obtain the 2D map of an unknown indoor environment with a quadrotor using an UWB system. We improved the state-of-the-art in two different aspects: First, to the best of our knowledge, this is the first implementation of a UWB system with a UAV for mapping an indoor environment. Second, we proposed a novel indoor navigation algorithm for mapping with a UAV and compared its performance with the two well-known algorithms.

MATERIAL AND METHODS

First, we present the localization and mapping techniques. Following that the three different navigation algorithms including our novel navigation algorithm are discussed. Lastly, the experimental setup is introduced.

Localization and Mapping

The most important and challenging part of this study is to obtain the location of the UAV and the map of the environment simultaneously. The aim of the SLAM process is to update the position of the robot by exploring the environment. SLAM operation consists of several stages. In general, odometry information calculated from the IMU is used to estimate the position of the UAV. However, this information is inaccurate due to noise and drift in IMU's. Therefore, we used a UWB localization system to estimate the position of the UAV. A LIDAR is also used both to reduce the error in position estimation and to detect the walls and obstacles in the environment. During mapping, the walls and obstacles present in the environment are extracted and observed. When the robot moves, observations are redone at the new position of the robot. Then, the robot tries to associate the new observations with the previous ones. Reobserved landmarks are used for updating the position estimation while the new landmarks are stored and used in the next steps. The UWB localization system is used together with the SLAM process and it is responsible for updating the position of the robot and the map of the environment.

Navigation Algorithms

In this section, the three navigation algorithms including our novel navigation algorithm are introduced.

Wall Following Algorithm

Wall following algorithm is a simple but highly effective method used for exploring and mapping of indoor environments [16]. Details of the wall following algorithm is discussed in a related study [17]. There are two different versions of the wall following algorithm in which the robot moves to the right or left of the wall. In this study, we employed the right version of the algorithm as detailed in Algorithm 1.

Algorithm 1. Pseudocode for Wall Following Algorithm [17].

```
while True do
    if Wall is not sensed ahead of the UAV then
        Adjust the turning velocity;
        Adjust the forward velocity;
        Adjust the altitude;
    else
        Turn 90 degrees right
    end
end
```

Exploration Algorithm

The purpose of this algorithm is to explore a closed area while avoiding collisions and covering the minimum possible distance. The total velocity of the UAV is obtained by the vectorial addition of the velocity contributions from the opening detection and obstacle avoidance behaviours [17].

The opening detection behaviours is used to identify the openings in the environment and to select the next destination point accordingly. The opening points are obtained by comparing the proportions of distances obtained from two consecutive angles over the entire scanning area. The distance of the opening from the station where the robot stops is found using the following formula:

$$r_{corner} = max \frac{r_i}{r_i + 1}, i = 1,2,3...,270 \quad (1)$$

where r_i and r_{i+1} are two consecutive laser scans while r_{corner} is the detected distance from the station.

Since the UAV's orientation, estimated position, UWB data, distance to the corner point and angle information are known, the position of the corner point can be obtained using Eq. 2 and Eq. 3.

$$x_{corner} = x_{UAV} + r_{corner} cos\ (\psi + \theta) \quad (2)$$

$$y_{corner} = y_{UAV} + r_{corner} cos(\psi + \theta) \quad (3)$$

where, x_{corner} is the x coordinate of the destination point and y_{corner} is the y coordinate of the destination point, ψ and θ refer to the heading angle and the angle between corner and quadrotor, respectively. Then, the angle between the target and the UAV is selected to be 10° away form the corner compared to the the angle between the corner point and the UAV. While the UAV's orientation is always towards the target, its forward speed is adjusted according to its distance from the target as calculated in the Eq. 4. Here, $v_{forward}$ is the forward velocity. K_0 and K_p represents the predefined velocity gain coefficients and l is the distance to destination point. The reason why using the cube root of the distance is to obtain smoother velocity changes as quadrotor gets closer to the destination.

$$v_{forward} = K_0 + K_p \sqrt[3]{l} \quad (4)$$

The speed contribution required to move around the obstacles safely and to move around the walls without collisions is calculated using the information obtained from the laser range finder at each angle. Using laser scans at each angle, velocity vectors are generated such that the magnitude is inversely proportional to and opposite to the distance as:

$$v_i = \frac{K}{r_i} \hat{r}_i \quad (5)$$

where, K is the predefined obstacle avoidance gain and v_i is the obstacle avoidance velocity. By summing the velocity vectors from the opening detection algorithm and obstacle avoidance algorithm, the velocity of the UAV is calculated.

Target-Based Navigation Algorithm

Target-based navigation algorithm is based on "Frontier-based Probabilistic Approach" algorithm [18]. This algorithm aims to explore map of the environment by moving the border between the discovered and undiscovered areas.

Basically, the target-based navigation algorithm creates an occupancy matrix by using data coming from the sensors. In this matrix, unknown areas take "-1" value and known regions take a value between "0" and "100" according to the occupancy rate. The Algorithm 2 first finds potential points to move using the Algorithm 3 and adds these points to a list. Then, it selects the nearest destination point and creates a path from the UAV to the target point. If the target point is reachable, UAV flies directly to that point as in the Algorithm 4. If there is an obstacle between the current position of the UAV and the next destination point, it uses A* algorithm to find the shortest obstacle-free path to the destination point. The algorithm monitors if the UAV reaches the destination point, and gives the next destination point until all the region is explored.

Algorithm 2. Pseudocode for Navigation Controller Algorithm Main Function.

```
prevNavStatus = DestNotReached;
NavStatus = DestNotReached;
while True do
    if NavStatus == DestReached && prevNavStatus == DestNotReached then
        Add current destination to AlreadyVisitedPoints;
        FindOpenSpaces(); //Reexamine the map;
        if PointsToBeVisitedList.empty() then
            Print a Message that all of the map is visited;
            return 0;
        else
            SelectNextDestination();
        end
    end
end
```

Algorithm 3. Pseudocode for Navigation Controller Algorithm FindOpenSpaces Function.

```
For each Grid Point on currentMap;
CheckOccupancy();
CheckClearance();
CheckAlreadyVisitiedList();
CheckToBeVisitiedList();
if Point meets criteria listed above then
    Add the point to PointsToBeVisited list;
end
```

Algorithm 4. Pseudocode for Navigation Controller Algorithm SelectNextDestination.

```
NearestPoint = FindTheNearestPointToBeVisited(); // Gets the nearest point in the
  PointsToBeVisitedList;
if isFlyable(CurrentPoint,NearestPoint) then
    NextDestination = NearestPoint; // If the nearest point is directly flyable, then it is the
      next destination;
    publish(NextDestination); // Send it to the FlightController;
else
    SelectNextDestinationByAStar(); // If the nearest point is not directly flyable, let A*
      algorithm decide the next destination point;
end
```

A* search algorithm [19] calculates the cost of each adjacent point by using an heuristic evaluation function as in Eq. 6. After all the calculations are done, it creates a suitable path by combining the points with minimum cost.

$$F(n) = G(n) + H(n) \tag{6}$$

In Equation 6, n is the previous point of the path, *G(n)* is the cost of the path from the start point to the adjacent point, and *H(n)* is the heuristic that estimates the cost of the lowest cost path from n to the target point. In our case, *H(n)* is the Euclidian distance between corresponding point and target point.

Experimental Setup

In this section, the software packages and the hardware used are introduced.

Software Packages

In this paper, ROS (Robot Operating System) is used as the middleware for controller development [20]. ROS speeds up controller development considerably due to its readily available libraries. Recently, it has been widely adopted in the robotics literature [21, 22]. ROS provides convenient low-level features such as device control, hardware abstraction, and management of packages, as well as many libraries for mapping and localization, navigation and perception.

Figure 1. Hector Quadrotor [23].

Gazebo is used as the simulation environment. Gazebo is a physics-based 3D simulator used widely in robotics studies. It uses different physics engines such as ODE and Bullet. OGRE is used as the graphics engine. ROS can seamlessly be integrated to Gazebo that eases the development of controllers in Gazebo. In the simulations, a PC with Ubuntu 16.04 LTS(Xenial Xerus) is used running ROS Kinetic Kame distribution and Gazebo 7.1.

Quadrotor

The Hector quadrotor model is used as the quadrotor platform [23]. "Hector SLAM" package including "Hector Mapping, Hector IMU Tools and Hector Nav Msgs" for simultaneous localization and mapping, which is developed especially for indoor environments, are used.

The laser range finder "Hokuyo UTM-30LX LIDAR [24]" is selected and mounted under the UAV. A sonar sensor is used to measure the height of the quadrotor from the ground. An IMU is used to measure the angular velocity and acceleration of the UAV. Lastly, a UWB sensor is used for localization. A tag is mounted on the quadrotor and anchors are placed on the walls of the environment as shown in Fig. 2. A new plugin named "Gazebosensorplugin" that is developed by Barral et al. [15] is adopted for reading the senors. The Hector Quadrotor model is shown with the integrated laser range finder in Fig. 1.

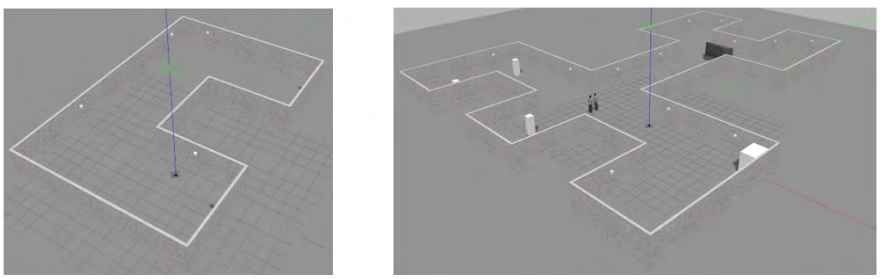

(a) (b)

Figure 2. Maps Used for Simulations. UWB anchors are shown with white spheres on the walls. (a) Map 1 [25] (b) Map 2 with Obstacles

Table 1. Performance Comparison Table for Map 1 (σ_{Exp}, σ_{Tar} and σ_{W} all denote the standard deviation of distance and time for the exploration, target-based and wall following methods, respectively.).

	Exploration Algorithm	*Target-Based Navigation Algorithm*	*Wall Following Algorithm*	σ_{Exp}	σ_{Tar}	σ_{Wall}
d [m]	*38*	*36*	*45*	*7,8*	*5,9*	*8,2*
t [s]	*253*	*247*	*312*	*52*	*40*	*57*

EXPERIMENTAL PROCEDURE

In Gazebo, two maps are developed with different complexities. On these maps, the aforementioned navigation algorithms are tested. The size of Map 1 is set to be approximately 280m^2 and there are no obstacles present on this map [25]. Similarly, a more challenging map is designed with a size of 850m^2 having different sized and shaped obstacles such as standing man, cube and barrier. The corresponding maps are shown in Fig. 2.

All three algorithms are tested on Map 1. However, exploration algorithm failed on Map 2 since it is not smart enough to carry out navigation and mapping on huge maps with obstacles. Therefore, only two algorithms are tested on Map 2. The quadrotor is released from ten different positions in order to check the repeatability of the algorithms. Simulations are completed after the entire map is explored.

Performance Metrics

All described algorithms perform the same task that is to obtain the map of an unknown indoor environment without colliding with any obstacles. It is required to determine some criteria in order to measure the effectiveness of algorithms in different scenarios. Hence two performance metrics are defined.

Distance

The distance travelled by the robot is recorded. The smaller the distance is, the more successful the algorithm is. *d* represents the distance of the robot in meters.

Time

This criterion is the total time spent throughout the mapping process of an unknown indoor environment. Time is indicated by *t* and it is measured in seconds.

RESULTS AND DISCUSSION

Simulations

The results of the simulations performed in Map 1 are shown in Fig. 3 for the exploration, target-based naviga-

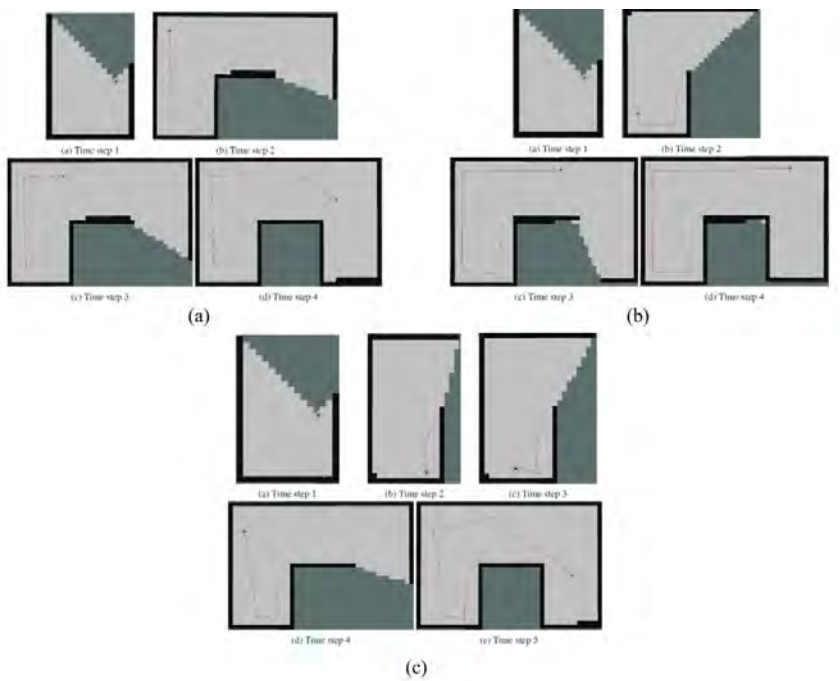

Figure 3. Navigation Algorithms for Mapping on Map 1. (a) Navigation with the Target-Based Navigation Algorithm (b) Navigation with the Wall Following Algorithm (c) Navigation with the Exploration Algorithm

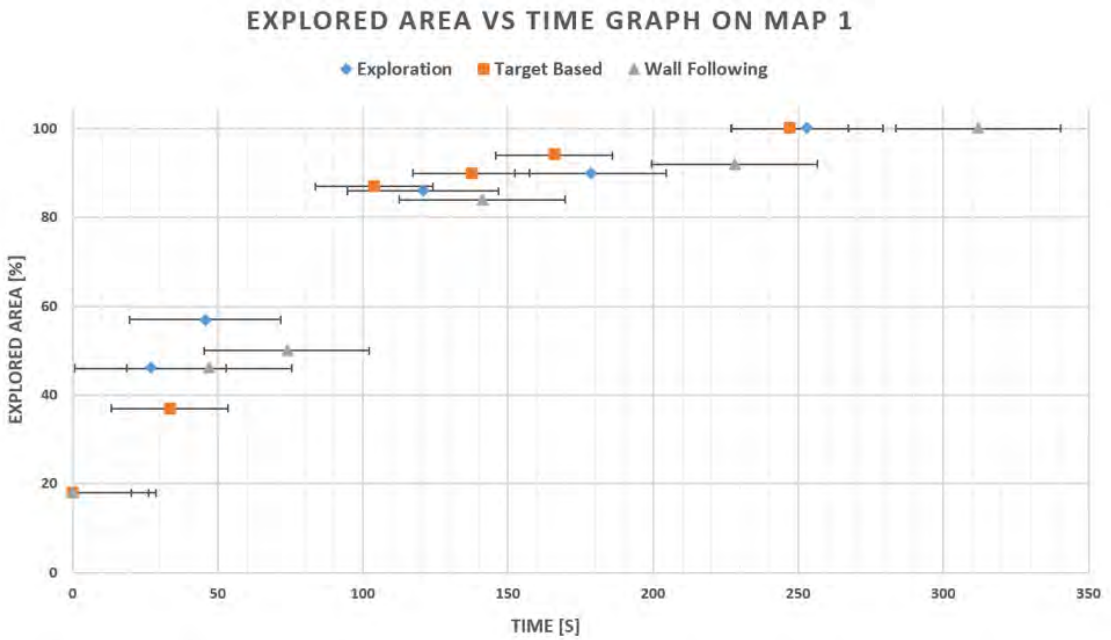

Figure 4. Time-Dependent Performance of the Navigation Algorithms on Map 1. Points show the mean and error bars show the variance. Time measurements are taken at some stop points of the corresponding algorithm as shown in Figure 3. For instance, quadrotor stops four times during navigation for the wall following algorithm while it stops five times for the exploration algorithm.

tion and wall following algorithms, respectively. In Fig. 3, the map is explored with five stops for the exploration algorithm while it is explored with six stops for the target-based navigation algorithm. On the other hand, number of stops is four for the wall following algorithm and it is equal to number of corners since wall following algorithm stops if it encounters a wall.

The performance of each algorithm on Map 1 are shown in Fig.s 4, 5 and Table 1 for time and distance, respectively. Target-based navigation algorithm performs better in terms of time and distance travelled when compared to the other two algorithms.

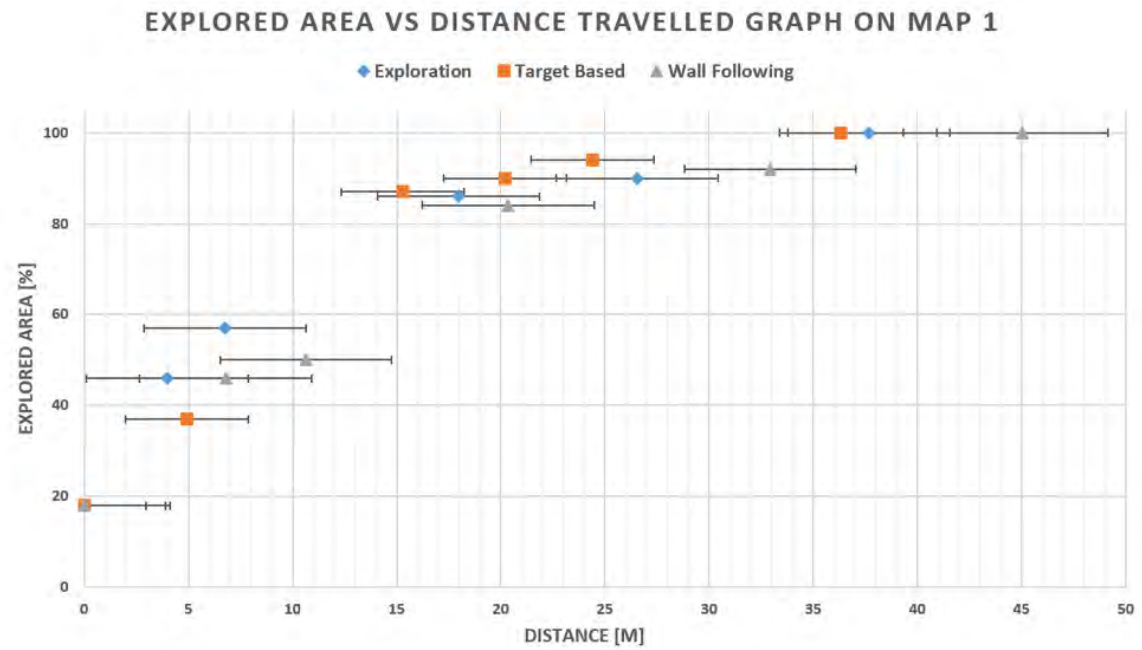

Figure 5. Path-Dependent Performance of the Navigation Algorithms on Map 1. Points show the mean and error bars show the variance. Distance measurements are taken at some stop points of the corresponding algorithm as shown in Figure 3. For instance, quadrotor stops four times during navigation for the wall following algorithm while it stops five times for the exploration algorithm.

Table 2. Performance Comparison Table for Map 2 with Obstacles (σ_{Tar} and σ_{W} all denote the standard deviation of distance and time for the target-based and wall following methods, respectively.).

	Target-Based Navigation Algorithm	*Wall Following Algorithm*	σ_{Tar}	σ_{Wall}
d [m]	*103*	*182*	*14,1*	*6,68*
t [s]	*812*	*1393*	*110*	*51*

The results of the simulations performed in Map 2 with obstacles are shown in Fig. 6 for target-based navigation and wall following algorithms, respectively. In Fig. 6, number of stops decreases for the target-based navigation algorithm due to the presence of obstacles in the environment. The wall following algorithm performs almost the same way as the previous map. However, longer distance is travelled with the wall following algorithm due to the larger size of Map 2.

The performance of each algorithm on Map 2 are shown in Fig.s 7, 8 and Table 2 for time and distance, respectively. Target-based navigation algorithm is far more superior than the wall following algorithm in terms of all performance measures.

Discussion

In this study, performance of different navigation algorithms on two different maps have been investigated based on time and travelled distance. The exploration algorithm makes the UAV to move to the corner points. It is successful on relatively small environments. However, it fails on the large ones. The simulation results of this algorithm was not shown in Map 2 since it failed on this map. The number of destination points visited is directly proportional to the number of corners as seen in Fig. 3. The algorithm revisits the discovered areas since it does not keep the positions in its memory. Major changes are observed in time and distance travelled values when the initial position of the robot is altered (see Fig.s 4 , 5 and Table 1). This indicates that the algorithm has poor repeatability performance.

Wall following is a well-known algorithm to navigate in indoor environments. Although it is known as a simple and effective algorithm, it has some drawbacks. If the size of the map increases, the distance travelled and the time spent also increase. It explores the map in similar ways. Thus, starting from different points for navigation does not affect the repeatability performance(see Fig. 4, 5, 7, 8 and Tables 1, 2). It does not check whether the map is explored or not since the only reference is wall tracking. It may obtain successful results in the indoor environments with continuous walls. However, it fails if there are multiple continuous walls in the environment.

The target-based navigation algorithm assigns targets and generates obstacle free paths. This algorithm is able to explore both Map 1 and Map 2 for each case. Although the target-based navigation algorithm performed similar to the other two algorithms on Map 1, it outperformed the two on Map 2.

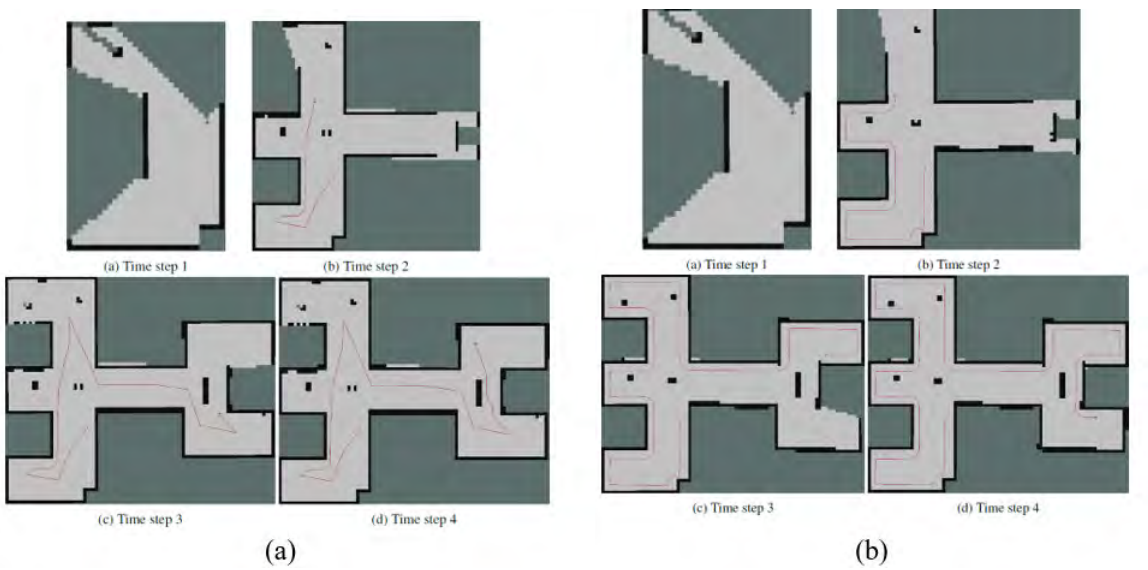

Figure 6. Navigation Algorithms for Mapping on Map 2 with Obstacles (a) Navigation with the Target-Based Navigation Algorithm (b) Navigation with the Wall Following Algorithm

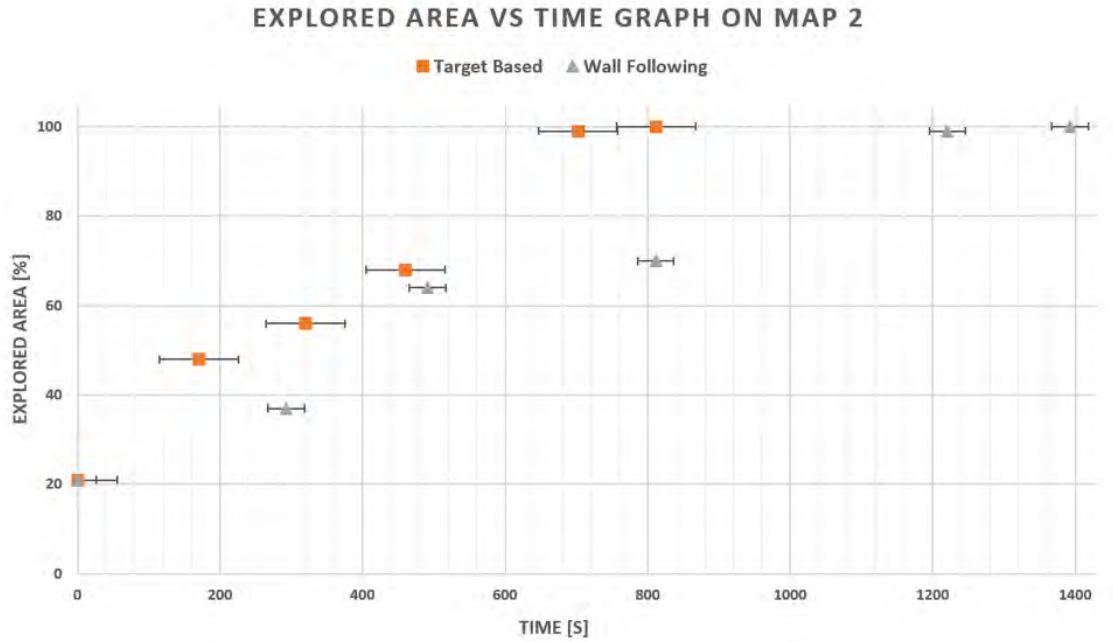

Figure 7. Time-Dependent Performance of the Navigation Algorithms on Map 2. Points show the mean and error bars show the variance. Time measurements are taken at some stop points of the corresponding algorithm as shown in Figure 6. For instance, quadrotor stops fourteen times during navigation for the target-based navigation algorithm while it stops twenty two times for the wall following algorithm.

In addition, with the target-based navigation algorithm similar results are obtained regardless of the initial position of the UAV since it has a consistent target generation algorithm as shown in Fig.s 4, 5, 7, 8 and Tables 1, 2. Therefore, repeatability performance is superior compared with the other navigation algorithms.

All in all, the exploration and the wall following algorithms move by using the details such as corners, walls and obstacles in the indoor environment. Therefore, they do not check whether the map has been discovered. On the other hand, the target-based navigation algorithm directly uses the explored areas to select the next destination. This feature guarantees that the map is explored.

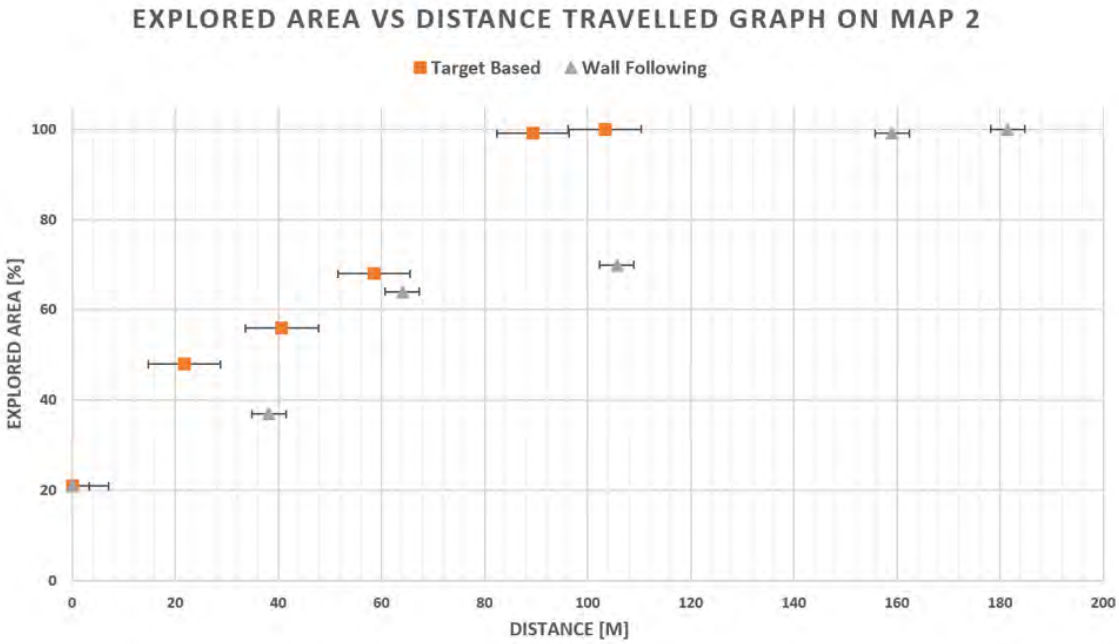

Figure 8. Path-Dependent Performance of the Navigation Algorithms on Map 2. Points show the mean and error bars show the variance. Distance measurements are taken at some stop points of the corresponding algorithm as shown in Figure 6. For instance, quadrotor stops fourteen times during navigation for the target-based navigation algorithm while it stops twenty two times for the wall following algorithm.

In addition, comparisons show that the target-based navigation algorithm gets better results than the other navigation algorithms.

CONCLUSION

In this study, a novel navigation algorithm was developed for a quadrotor in order to obtain the map of unknown indoor environments. Two different navigation algorithms that were presented in the previous studies were used to compare the performance of the proposed novel algorithm using different performance metrics. LIDAR-based SLAM method was used in all algorithms. UWB localization was applied to the exploration algorithm and the novel algorithm by using anchors placed on the walls and a tag mounted on quadrotor. In this way, local positioning system was formed. Local positioning was not used for the wall following algorithm since it does not require localization. Wall following is an old and well-known navigation algorithm. It is suitable for mazelike environments but it can also be used for any indoor environment. However, it performs poorly when time and distance travelled are important. In addition, it does not succeed in indoor environments with large empty spaces. The exploration algorithm uses corners and open spaces to find destination points. Even if it is considered as successful in small indoor environments, it fails in large indoor environments with obstacles. Different than this, the novel algorithm guarantees to obtain the whole map since it directly uses the explored areas by composing a matrix. Navigation system of the wall following and exploration algorithms is not based on explored map. The map of an indoor environment is explored unconsciously by these algorithms since they just use the features of the environment without checking whether the map is explored or not. In addition, novel algorithm may be applied for any robots including aerial robots, ground robots and underwater robots.

The performed simulations showed that the novel algorithm mostly beats the opponents. Exploration algorithm directly failed in large indoor environments including different obstacles. Although wall following algorithm managed to obtain map of indoors, it wasted time and travelled a longer distance. Moreover, repeatability analysis indicates that performance metrics come out with close values for novel algorithm. In other words, navigation with novel algorithm raises similar results regardless of the robot's initial position.

As a future work, the navigation algorithms can be tested in physical environments by setting up the maps in real world. Instead of LIDAR based SLAM method, camera based SLAM method may be used easily by taking advantage of generic novel algorithm. In addition, several quadrotors can be released from different points simultaneously in order to reduce the discovery time of the map and communication among quadrotors can be established using wireless technologies. Furthermore, the novel algorithm can be tested using various aerial, ground and underwater robots.

References

1. Y. Khosiawan and I. Nielsen, "A system of uav application in indoor environment," Production & Manufacturing Research 4(1), 2–22 (2016).
2. C. Hegde and N. S. Guptha, "Implementation of Mapping Algorithm for SLAM Operation," Ijetae 3(9), 235–238 (2013).
3. A. Araujo, D. Portugal, M. S. Couceiro, et al., "Integrating Arduino-Based Educational Mobile Robots in ROS," Journal of Intelligent and Robotic Systems: Theory and Applications 77(2), 281–298 (2014).
4. H. I. M. A. Omara and K. S. M. Sahari, "Indoor mapping using kinect and ROS," 2015 International Symposium on Agents, Multi-Agent Systems and Robotics, ISAMSR 2015 , 110–116 (2016).
5. N. Johnson, "Vision-Assisted Control of a Hovering Air Vehicle in an Indoor Setting," Engineering and Technology (August) (2008).
6. S. Ahrens, D. Levine, G. Andrews, et al., "Vision-based guidance and control of a hovering vehicle in unknown, gps-denied environments," Proceedings - IEEE International Conference on Robotics and Automation , 2643–2648 (2009).
7. J. F. Roberts, T. S. Stirling, J.-C. Zufferey, et al., "Quadrotor Using Minimal Sensing For Autonomous Indoor Flight," European Micro Air Vehicle Conference and Flight Competition (EMAV2007) (September), 17–21 (2007).
8. M. Kara Mohamed, S. Patra, and A. Lanzon, "Designing simple indoor navigation system for UAVs," 2011 19th Mediterranean Conference on Control and Automation, MED 2011, 1223–1228 (2011).
9. M. Achtelik, J. Williams, M. J. Owen, et al., "Autonomous Navigation and Exploration of a Quadrotor Helicopter in GPS-denied Indoor Environments," First Symposium on Indoor Flight (2009).
10. S. Grzonka, G. Grisetti, and W. Burgard, "A fully autonomous indoor quadrotor," IEEE Transactions on Robotics 28(1), 90–100 (2012).
11. F. Wang, J. Cui, S. K. Phang, et al., "A mono-camera and scanning laser range finder based UAV indoor navigation system," 2013 International Conference on Unmanned Aircraft Systems, ICUAS 2013 - Conference Proceedings , 694–701 (2013).
12. O. Oguejiofor, A. Aniedu, H. Ejiofor, et al., "Trilateration Based localization Algorithm for Wireless Sensor Network," Int. J. Sci. Mod. Eng (10), 21–27 (2013).
13. H. Liu, J. Liu, P. Banerjee, et al., "Survey of Wireless Indoor Positioning Techniques and Systems," IEEE Transactions on Systems, Man, and Cybernetics, Part C (Bucharest, Romania : 1990) 35(1), 39–42 (1991).
14. B. Kempke, P. Pannuto, and P. Dutta, "SurePoint: Exploiting Ultra Wideband Flooding and Diversity to Provide Robust, Scalable, High-Fidelity Indoor Localization," SenSys , 318–319 (2016).
15. V. Barral, P. Su´arez-Casal, C. J. Escudero, et al., "Multi-sensor accurate forklift location and tracking simulation in industrial indoor environments," Electronics (Switzerland) 8(10) (2019).
16. J. R. B. del Rosario, J. G. Sanidad, A. M. Lim, et al., "Modelling and Characterization of a Maze-Solving Mobile Robot Using Wall Follower Algorithm," Applied Mechanics and Materials 446-

447(July), 1245–1249 (2013).
17. E. B. Küçüktabak, M. M. Pelit, Z. O¨ . Orhan, et al., "Kapalı Bir Alanda Basit Bir IHA ile Keşif Metodu Tasarımı Indoor UAV Exploration Method with UWB Localization," TOK , 1–6 (2017).
18. L. Freda and G. Oriolo, "Frontier-Based Probabilistic Strategies for Sensor-Based Exploration," International Conference on Robotics and Automation (April), 3892–3898 (2005).
19. P. E. Hart, N. J. Nilsson, and B. Raphael, "A Formal Basis for the Heuristic Determination of Minimum Cost Paths," IEEE Transactions of Systems Science and Cybernetics 4(2), 100–107 (1968).
20. M. Quigley, K. Conley, B. P. Gerkey, et al., "Ros: an open-source robot operating system," in ICRA Workshop on Open Source Software, (2009).
21. M. S. Güzel, V. B. Ajabshir, P. Nattharith, et al., "A novel framework for multi-agent systems using a decentralized strategy," Robotica 37(4), 691–707 (2019).
22. M. S. Güzel, E. C. Gezer, V. B. Ajabshir, et al., "An adaptive pattern formation approach for swarm robots," in 2017 4th International Conference on Electrical and Electronic Engineering (ICEEE), 194–198, IEEE (2017).
23. J. Meyer, A. Sendobry, S. Kohlbrecher, et al., "Comprehensive Simulation of Quadrotor UAVs using ROS and Gazebo," 7628(November) (2012).
24. Hokuyo, "Scanning Rangefinder Distance Data Output/URG-04LX-UG01 Product Details — Hokuyo Automatic Co. Ltd."
25. O. Oral, A. E. Turgut, and K. B. Arıkan, "IHA ile GPS Kullanmadan Kapalı Alanların Haritasının Çıkartılması," ToRK 2019 - Turkiye Robotbilim Konferansı 5(1), 105–111 (2019).

Hittite Journal of Science and Engineering, 2020, 7 (2) 135-148
ISSN NUMBER: 2148-4171
DOI: 10.17350/HJSE19030000182

An Experimental Study On The Performance And Exhaust Emission Characteristics Of A CI Engine Powered By Alcohol/Biodiesel/Diesel Fuel Blends Containing Different Types Of Alcohol (Isopropanol-C3, 1-Butanol-C4, And Isopentanol-C5)

Murat Kadir Yeşilyurt
Yozgat Bozok University, Department of Mechanical Engineering, Yozgat, Turkey

ABSTRACT

Alcohols are significant alternative and renewable fuel candidates for the utilization in the internal combustion engines due to encouraging favorable environmental and economic outputs. Long-chain alcohols have various advantages over short-chain alcohols because of their larger energy content, elevated cetane number (CN) and preferable blending properties, etc. The objective of the present experimental research deal with the exploring and compare the influence of the ternary fuel mixtures of petroleum-based diesel fuel, cottonseed oil methyl ester (COME) and long-chain alcohols of isopropanol (Pr), 1-butanol (Bt), and isopentanol (Pt) on the performance and emission characteristics of a single-cylinder, four-stroke, naturally-aspirated, direct-injection compression-ignition (CI) engine. As the prepared tested fuel samples, four different blends were as follows on a volume basis: B20 (20% COME + %80 diesel fuel), B20Pr20 (20% COME + %20 isopropanol + %80 diesel fuel), B20Bt20 (20% COME + %20 1-butanol + %80 diesel fuel), and B20Pt20 (20% COME + %20 isopentanol + %80 diesel fuel). The engine trials were carried out at various loads (0-1250 W) and under a constant speed (3000 rpm) to observe the aforementioned behaviors. Based on the experimental outcomes, brake specific fuel consumption (BSFC) values of B20Pr20 exhibited higher than those of other ternary blends at all loads. Brake thermal efficiency (BTE) values for B20Pt20 were observed as larger than those of ternary blends. B20Pt20 had higher exhaust gas temperature (EGT) values than those of B20Bt20 and B20Pr20. The infusion of long-chain alcohols to COME/diesel blend caused to reduce NO_x emissions meanwhile isopropanol, 1-butanol, and isopentanol were the most to least influential alcohol types, respectively. Besides, with the addition of alcohol, a substantial decrement was noticed in smoke opacity at entire loads owing to the excess amount of oxygen content and lesser ratio of C/H of the alcohols. However, CO and HC emissions rose by infusion of long-chain alcohols to the blends. Finally, it can be concluded that higher alcohols could be a possible fuel additive for the fractional replacement for petroleum-based diesel fuel and biodiesel in the blends for CI engine practices.

Keywords:
Cottonseed oil methyl ester, Long-chain alcohols, Performance, Emission, Diesel engine

Article History:
Received: 2020/03/20
Accepted: 2020/06/09
Online: 2020/06/26

***Correspondence to**: Murat Kadir Yeşilyurt, Department of Mechanical Engineering, Yozgat Bozok University, Yozgat, Turkey*
Tel: +90 3542421001
Fax: +90 3542421005
E-Mail:kadir.yesilyurt@bozok.edu.tr

INTRODUCTION

Diesel engines or CI engines have been taken into consideration to be a vital and important power source all over the world for various areas such as transportation (land, air, and sea), agriculture, power generation, industrial activities, and construction engineering sectors because they have high-performance features [1-3]. Diesel engines possess also capacity in terms of supplying higher torque, higher power outcome, higher durability and superior fuel conversion efficiency in comparison with the spark ignition engines [4]. The aforementioned characteristics, therefore, showed that diesel engines are preferable selection as compared to the gasoline engines considering the widespread area of applications [5]. Unfortunately, diesel engines are largely depended on the fossil-based fuels. The pollutants released from the engines have been increased worldwide owing to the production as well as consumption of

Nomenclature

BSFC	Brake specific fuel consumption (g/kWh)
BTE	Brake thermal efficiency (%)
CA	Crank angle (degree)
COME	Cottonseed oil methyl ester
CN	Cetane number
CI	Compression-ignition
Pr	Isopropanol
Bt	1-butanol
Pt	Isopentanol
B20	20% COME + %80 diesel fuel
B20Pr20	20% COME + %20 isopropanol + %80 diesel fuel
B20Bt20	20% COME + %20 1-butanol + %80 diesel fuel
B20Pt20	20% COME + %20 isopentanol + %80 diesel fuel
D100	Diesel fuel
EGT	Exhaust gas temperature (°C)
TDC	Top dead center
EGR	Exhaust gas recirculation
NaOH	Sodium hydroxide
CO	Carbon monoxide (%)
LHV	Latent heat of vaporization (kJ/kg)
HC	Unburned hydrocarbon (ppm)
ID	Ignition delay (degree)
NOx	Oxides of nitrogen (ppm)
NO_2	Nitrogen dioxide (ppm)
NO	Nitrogen monoxide (ppm)
CO2	Carbon dioxide (%)
R	Dependent factor
X	Independent variables
W	Uncertainty value

fossil-based fuels. By all means, most of the pollutants have been spread because of the utilization of diesel fuel [6, 7]. The portion of contaminants in the overall atmospheric air pollution brought about by transportation vehicles powered by diesel engines has been augmenting along with the rise of these vehicles in the world [8]. From those issues, it is to be noted that alternative, renewable, sustainable and clean fuel resources for diesel engines have to be searching because of the motivating parameters related to the fluctuations in the petroleum prices, concerns with global warming, toxic pollutants released from the engines and strict emission legislation [9-13].

Alternative fuel resources have commenced acquiring higher popularity by countries owing to their capability in the reduction of greenhouse gasses, presence in nature and availability, less dependency on petroleum imports, etc. [14, 15]. Among the above-mentioned sources, biodiesel and alcohols have great potentials in the countries where have a higher amount of biomass capacity. Also, they are come up with alternative candidates for replacement over diesel fuel [16]. Biodiesel can be briefly described as the mixture of the mono-alkyl esters of long-chain fatty acids synthesized from different raw materials like vegetable oils, animal fats and their wastes, etc. [17]. Although there are different techniques (dilution, pyrolysis, transesterification, microemulsion) to obtain biodiesel, the transesterification method has been mostly used by researchers [18, 19]. One of the most significant characteristics of biodiesels is to being possess lesser emissions in comparison with mineral diesel fuel. Biodiesel is an alternative, renewable, non-toxic, environmentally-friendly, sulfur-free, and clean fuel [20, 21]. Biodiesel fuels have not only direct use in diesel engines but they can be also used by mixed with conventional diesel fuel at any concentrations [22]. However, the diesel engines have not been operated with pure biodiesel up to 100% out of any engine alteration because of its higher density and viscosity values. In addition, the worse low-temperature properties for biodiesel fuels are limited in terms of direct usage. The above mentioned worse characteristics of biodiesel can be eliminated with blending alcohols [23, 24]. Alcohol can be synthesized from renewable raw materials like biomass, thus, it is an important renewable fuel [25]. On the other hand, alcohols have a few substantial disadvantages like low CN, high latent heat of vaporization (LHV). It can be clearly, therefore, stated that the alcohols could not be preferred as a fuel in CI engines directly [26].

As known, the fuel properties of biofuels have to be enhanced and brought closer to the traditional diesel fuel before using in the diesel engines. Many fuel specifications like viscosity and density can be developed with the supplementation of various types of alcohols to biodiesel or diesel fuel/biodiesel mixtures [27, 28]. When the present literature was surveyed, such researches performed and the focus on the point of these investigations has generally been related to the diesel fuel/biodiesel mixtures and the infusion of particular alcohols into those blends [29-31]. The researchers have been the most commonly tested biodiesel produced from various vegetable oils and ethanol (C_2H_5OH) as renewable, sustainable, and alternative fuels in CI engines at several proportions [32, 33]. Ethanol leads to separation of phase above 10°C when it is mixed with biodiesel or diesel fuels to power the CI engines [34]. Besides that, ethanol cannot be blended with pure diesel fuel with high proportions due to less CN resulting in ignition delay (ID), low energy content and worse lubricity characteristic of ethanol [35]. Noteworthy, it has been considered that alcohol can be more smoothly blended with biodiesel and diesel fuels regarding the increase of carbon atoms in the chemical bonds of the alcohol. Moreover, the rise of the carbon atom number inside the alcohol causes to boost CN, energy capacity, viscosity, and density while decreasing the excessive amount of inherent oxygen content. Concerning the quantity of carbon atoms in the chemical bonds of long-chain alcohols such

as propanol-C_3H_7OH, butanol-C_4H_9OH, and pentanol-C5H11OH have higher energy contents, densities, viscosities, CN, flame speeds even though they have lower LHV, risk of corrosion, and ignition temperature [36, 37]. When the literature was comprehensively evaluated, there is a limited number examination with respect to the investigation of propanol with blending biodiesel and diesel fuels on the influences of the engine characteristics involving performance, emissions, and combustion [38-41]. No doubt that the recent literature has exhibited numerous papers investigating the butanol blends with diesel and biodiesel [4, 25, 42-49]. However, the researches that use of many pentanol isomers as alternative additives for diesel fuel and biodiesel have not been enough. For instance, Campos-Fernández et al. [50], Li et al. [51, 52], Yang et al. [53], Santhosh et al. [54] and Sridhar et al. [55] studied the effects of pentanol on the engine performance, emissions, and combustion behaviors of different types of diesel engines.

Based on the aforementioned studies conducted by various researchers, butanol and pentanol might be tested to be as oxygenated fuel additives for diesel fuel, biodiesel, and their blends out of any major alteration on the engine. In addition to this, these researches have approved that the higher-order alcohols such as butanol and pentanol have been found to be more powerful additives than short-chain alcohols in terms of improving the fuel properties of biodiesel, and hence, they can be accepted as next-generation biofuels owing to the above-mentioned potentials. In spite of the fact that there are many researches regarding the higher-order alcohols as referring above, as far as the author knows that there is a skimpy number of papers in the recent literature for the assessment of propanol, butanol, and pentanol in the identical test engine. Some of them were summarized as follows: Atmanli [8], for instance, performed comparative analyses of waste oil biodiesel/diesel fuel and propanol, n-butanol or 1-pentanol blends in a CI engine to observe the performance and emissions levels. The researcher found that the supplementation of the above-mentioned higher-order tested alcohols to the biodiesel/diesel fuel blend inspired to enhance the cold flow specifications. BSFC for ternary blends increased owing to the lower calorific values of the alcohols in the meantime BTE augmented. All the tested long-chain alcohol fuel samples boosted CO emissions meanwhile NO_X emissions decreased in contrast to the diesel/biodiesel fuel blend. Jin et al. [9] scrutinized the impacts of the different kinds of propanol (n-propanol, iso-propanol), butanol (n-butanol, iso-butanol, sec-butanol, tert-butanol), and pentanol (n-pentanol, iso-pentanol, tert-pentanol) on the solubility of alcohol/diesel mixtures. Kumar and Saravanan [36] reviewed the usage of higher-order alcohols in the CI engines comprehensively. Kumar et al. [41] optimized the performance and emission features of a DI diesel engine fueled with the blends of diesel/n-propanol, n-butanol or n-pentanol applying statistical approach such as response surface methodology. The best engine configurations were monitored for diesel/n-propanol as injected at 25o crank angle (CA) before top dead center (TDC) with 30% exhaust gas recirculation (EGR) and for others, as injected at 24º CA before TDC with 10% EGR. Ghadikolaei et al. [56] scrutinized the performance, combustion, and emission patterns of a CI engine running on diesel/biodiesel/alcohol (methanol-C1, ethanol-C2, propanol-C3, butanol-C4, and pentanol-C5) blends. Interestingly, the researchers ensured the blends with the same oxygen concentration as 5%. They concluded that the methanol blend exhibited the best performance with least emission profiles amongst the tested fuel blends. Yilmaz et al. [57] experimented the influence of the several higher-order alcohols such as propanol, n-butanol, and 1-pentanol addition into the methyl ester obtained from waste oil on the performance and emission properties of a CI engine under diverse engine loads (0, 3, 6, and 9 kW) and a constant speed of 1800 rpm. As a result, they highlighted that 10% (by volume) alcohol addition into the waste oil methyl ester seems reasonable to accept as an alternating to traditional fossil-based diesel fuel taking into account their higher BSFC figures. Atmanli and Yilmaz [58] examined the combustion features of a CI engine under the semi-low temperature fuelled condition with waste oil biodiesel/alcohol (propanol-C3, n-butanol-C4, and 1-pentanol-C5). They marked that all of the tested alcohols in the experiments have been found to be candidates for diesel engines in the reduction of harmful gases released from the engine. As observed, currently published papers in this subject figured out many outcomes on the influences of higher alcohols concerning the performance and exhaust gas pollutants in the CI engine. The present experimental examination was performed so as to complete the above-mentioned gap since the comparison of performance and emission characteristics of the handled alcohols have not been scrutinized in detail.

In the present work, as alternative and clean fuels, the long-chain alcohols of isopropanol, 1-butanol, and isopentanol were blended with diesel fuel and COME as a fractional substitution in CI engine applications. The methyl ester namely alternative biodiesel fuel from the cottonseed oil was produced via implementing a single-step transesterification reaction using methanol in the presence of NaOH. For preparing the tested fuel samples, 20% (by volume) isopropanol, 1-butanol, and isopentanol was added into the diesel/COME blend to obtain B20Pr20, B20Bt20, and B20Pt20. In order to evaluate the performance and emission characteristics of a single-cylinder, four-stroke, DI diesel engine, the trials were conducted on under five dissimilar engine loads (0-1250 W) with a fixed speed (3000 rpm) for each tested fuels. Afterward, the results coming from the experiments were meticulously compared with the reference fuels those are diesel and diesel/COME blend.

Table 1. The key fuel characteristics of the tested fuel samples

No	Property	Unit	D100	B20	B20Pr20	B20Bt20	B20Pt20	Isopropanol	1-butanol	Isopentanol
1	Density at 15°C	kg/m^3	825	838	830	834	835	784	807	812
2	Kinematic viscosity at 40°C	mm^2/s	2.539	3.011	2.857	2.955	3.088	1.769	2.258	2.923
3	Lower calorific value	kJ/kg	43571	42306	39322	40192	40540	28652	33002	34741
4	Cetane number	-	52.30	51.04	42.98	43.98	44.58	12[1]	17[1]	20[1]
5	Carbon	wt. %	87.05	84.64	79.23	80.20	80.87	60.00	64.87	68.18
6	Hydrogen	wt. %	12.95	12.96	13.04	13.07	13.10	13.33	13.51	13.64
7	Oxygen	wt. %	0	2.40	7.73	6.73	6.03	26.67	21.62	18.18
8	Carbon/Hydrogen		6.722	6.531	6.078	6.136	6.174	4.501	4.802	4.999
9	Water content	ppm	23	118	230	185	279	580	350	820
10	Latent heat of evaporation[1]	kJ/kg	270-375	-	-	-	-	727.88	581.4	308.5
11	Copper strip corrosion[2]	Degree of corrosion	la	la	la	la	la	-	-	-

[1] These values were adopted from Kumar and Saravanan [36]
[2] 3 h at 50°C

MATERIALS AND METHODS

In this experimental research, the influences of different kinds of alcohol infusion into the biodiesel/diesel mixture on the engine performance and emissions patterns have been explored elaborately. For the aforementioned intent, diesel fuel, cottonseed oil methyl ester (COME), and alcohols (isopropanol-C3, 1-butanol-C4, and isopentanol-C5) have been used during the experiments. Isopropanol (99.7% purity) and 1-butanol (99% purity) were bought from Emir Chemical (Ankara-Turkey) while isopentanol (>98% purity) was supplied from Tekkim Laboratory Chemicals (Bursa-Turkey). During the engine test, commercially available diesel fuel purchased from a regional oil station (Yozgat- Turkey) was experimented in order to get the baseline data. Diesel fuel was called as D100.

The biodiesel fuel was produced by implementing a laboratory-scale single-step transesterification process in the Biofuel Laboratory, Mechanical Engineering Department, Yozgat Bozok University (Yozgat-Turkey). The transesterification technique using methanol (99.8% purity) and sodium hydroxide (NaOH) pellets (99% purity) was used to prepare the COME. Cottonseed oil was taken from a local market (Ankara, Turkey). In order to produce the COME, the optimum transesterification reaction conditions were applied as follows: reaction temperature of 60°C, methanol to oil molar ratio of 6:1, reaction duration of 60 min, and catalyst concentration of 0.6%. More detail about the production of biodiesel from cottonseed oil can be also come across in the previous work of the author [59].

COME was mixed with pure diesel at the proportion of 20% on a volume basis and coded as B20 (20% COME + %80 diesel fuel). Later, the above-mentioned higher-order alcohols were mixed with B20 at the same ratio with biodiesel, i.e., 20% (by volume) decreasing the diesel concentration in the blend. These blends are called as B20Pr20 (20% COME + %20 isopropanol + %80 diesel fuel), B20Bt20 (20% COME + %20 1-butanol + %80 diesel fuel), and B20Pt20 (20% COME + %20 isopentanol + %80 diesel fuel). Some of the physicochemical specifications of the chosen alcohols in the current study and the key fuel characteristics of the tested fuel specimens used in the engine trials were presented in Table 1.

The diesel engine experiments were executed at several loads such as 0 W, 500 W, 750 W, 1000 W, and 1250 W under the fixed speed (3000 rpm). To eliminate the errors, all of the fuel specimens were tried under almost identical working conditions. All of the parameters coming from the engine tests were compared with the reference D100 and B20.

The diagrammatic appearance of the experimental layout was technically illustrated in Fig. 1. The engine trials have been achieved in a single-cylinder, DI diesel engine. This diesel engine was mounted on a generator and the series of electrical resistance components were placed to load this test engine. The technical properties of the diesel power generator were given in Table 2. The engine experiments were performed without any engine modification. Besides, all data were recorded during the tests whenever the tested engine attained the conditions of steady-state. For this purpose, the engine had been operated at least 15 minutes, before each experiment commenced.

The emission patterns (carbon monoxide, carbon dioxide, unburned hydrocarbon, and nitrogen oxides) and smoke opacity data of the fuels used in this study were measured with the assistance of a gas analyzer and opacimeter (Italo Plus-Spin type). Table 3 showed the range of the measurement and accuracy values of the exhaust gas analyzer and opacimeter. Prior to the emission measurement, the gas

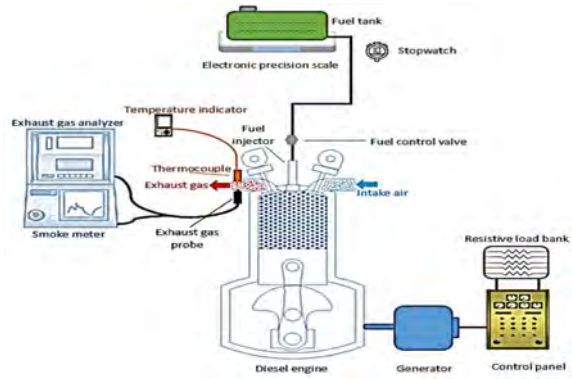

Figure 1. The schematic diagram of the experimental setup

Table 2. Technical specifications of the diesel power generator

Diesel engine		Generator	
Manufacturer	Katana	Manufacturer	Katana
Model	Km 178Fe	Model	KD 4500E
Cylinder number	Single-cylinder	Maximum power	4.2 kVA
Cycle number	Four	Power	3.6 kVA
Bore x Stroke	78 mm x 62 mm	Phase	1
Volume of cylinder	296 cm^3	Voltage	230 V
Power output (Continuous)	6 hp	Frequency	50 Hz
Power output (Maximum)	6.7 hp		
Speed	3000 rpm		
Compression ratio	18:1		
Injection system	DI		
Cooling system	Air-cooled		
Injection timing	31°bTDC		
Injection pressure	200 bar		
Intake system	Naturally-aspirated		
Injector nozzle number	4		

sensors of the device were calibrated thanks to the standard gases so as to keep away from the faults. To get each exhaust gas emission findings and to avoid unsteadiness, the measurements were carried out at least five times at a similar interruption and their averages were calculated and presented in this study.

To measure the EGT values for the tested fuels, a K-type thermocouple was embedded on the exhaust pipe. As observed from Fig. 1, the consumption of the tested fuel samples was assigned in mass using a stopwatch and an electronic precision scale. As a measure, the fuel consumption of all the fuel samples, the initial and final mass was recorded each 15 minutes duration at each engine load operating condition.

As is well known that, the probability of errors occurring

Table 3. Technical properties of the exhaust gas analyzer and opacimeter

Parameter	Unit	Range	Accuracy
CO	%	0-9.99	± 0.06
CO2	%	0-19.99	± 0.05
HC	ppm	0-2500	± 12
NOx	ppm	0-2000	± 5
Smoke opacity	%	0-99	± 2
EGT	°C	0-750	± 1
Operating temparature	°C	5-40	
Storage temperature	°C	(-20)-(+60)	
Feed voltage	V DC	12	

in any examination is high in the course of whole investigations. Indeed, many errors form from the side of the researcher though some of them are randomly comprised. In plenty of cases, the uncertainty of the investigation is commonly overcome by exerting the increase of the experimental run. On the other hand, sometimes there may be no chance of repeating experiments owing to the particular conditions that high-cost studies may be executed. Accordingly, the researchers should be meticulous and attentive in order to ensure the experimental findings for reducing the errors. With this intend, the uncertainties of the used apparatuses in the present research like exhaust gas emission sensors, temperature sensor, etc. were considered [60]. It is to be noted that the uncertainty values of the findings of the current work can be estimated in accordance with the square root method by using Equation (1) [61-63]. The values of the uncertainties as percentages for the detected parameters have been shown in Table 4.

$$w_R = \left[\left(\frac{\partial R}{\partial x_1} w_1 \right)^2 + \left(\frac{\partial R}{\partial x_2} w_2 \right)^2 + \ldots + \left(\frac{\partial R}{\partial x_n} w_n \right)^2 \right]^{1/2} \quad (1)$$

where;

- R: Dependent factor,
- x: Independent variables,
- w: Uncertainty value.

As a result, the entire uncertainty value coming from the types of equipment used in the experiments was calculated as ±2.74% applying the formula given underneath. It can be concluded that this value is well within the acceptable limits [64, 65].

$$\begin{aligned} &Overall\ uncertainity = Square\ root\ of\ \{(uncertainity\ of\ BSFC)^2 \\ &+(uncertainity\ of\ BTE)^2 + (uncertainity\ of\ CO)^2 + (uncertainity\ of\ NOx)^2 \\ &+(uncertainity\ of\ HC)^2 + (uncertainity\ of\ CO_2)^2 + (uncertainity\ of\ smoke)^2 \\ &+(uncertainity\ of\ EGT)^2\} \end{aligned} \quad (2)$$

Table 4. Uncertainties values of the measured parameters

No	Instrument	Uncertainty (%)
1	Load indicator	± 0.5
2	Temperature sensor	± 1.0
3	Speed	± 0.2
4	Smoke meter	± 1.0
5	Precision scales	± 0.5
6	Digital stop watch	± 0.2
7	Exhaust gas analyzer	
	CO	± 0.4
	CO_2	± 0.6
	HC	± 0.5
	NOx	± 0.9

$$= Square\,root\,of \left\{ \begin{matrix} (1.4)^2 + (1.4)^2 + (0.4)^2 + (0.9)^2 \\ + (0.5)^2 + (0.6)^2 + (1.0)^2 + (1.0)^2 \end{matrix} \right\} \quad (3)$$

$$= 2.74\% \quad (4)$$

RESULTS AND DISCUSSION

The performance and emission patterns for all the tested fuels (D100, B20, B20Pr20, B20Bt20, and B20Pt20) have been detected under different engine loads from 0 W to 1250 W and at a fixed speed (3000 rpm). In the course of the research, great deals of parameters have been evaluated and the aforementioned experimental outcomes have been taken into account so as to compare with the conventional baseline D100 and B20 fuel blend. In addition, these findings were comprehensively discussed considering the recent literature in this section which was presented underneath.

3.1. Engine performance characteristics

The BTE, BSFC, and EGT have been regarded the principal factors which have been benefited to identify the engine performance properties of a test engine while it is being run on the suited fuel samples. These major parameters are discussed in the below subsections point by point.

3.1.1. Brake thermal efficiency

BTE is summarized as being the efficiency of chemical energy conversion to the effective work obtained from the internal combustion engine. BTE is depended upon the net calorific value of the used fuel in the test engine since it is the rate of the output power to the heat ensured from the fuel [66]. Change of BTE values for the D100, B20, B20Pr20, B20Bt20, and B20Pt20 against the engine load was shown in Fig. 2. As it is obvious from the graph, BTE rises along with a promotion in load and the maximum results have been appeared under the highest condition operating condition. This case can be explained with much more fuel is spent at the higher loads able to generate a higher output of power in the engine [67]. The peak BTE values were observed by D100 all of the loads that are owing to its highest content of the energy of 43.571 MJ/kg. In contrast to D100, the lowest BTE values were obtained by B20Pr20 at all loads. It can be predicated to the fact that the net calorific value namely energy content of isopropanol (28.652 MJ/kg) is the least among the tested fuel samples, as seen in Table 1. Besides, B20 blend fuel shows lower values than that of pure D100 because of worse viscosity and atomization characteristics of the biodiesel fuel [68]. Actually, the B20Pt20 fuel blend is displayed by comparatively higher BTE values than those of ternary blends as a result of the existence of D100 that satisfies a reduction in the energy content of COME. At the maximum load, BTE values of D100, B20, B20Pr20, B20Bt20, and B20Pt20 were found to be at 23.83%, 21.51%, 18.24%, 19.75%, and 20.36%, respectively. As expected, all the ternary blends figure lesser BTE values than that of B20 at entire loads. This is because of the tested alcohols in the blends which they have less net calorific value than diesel fuel resulting in the reduction of calorific value of the blend [69]. Isopentanol has the highest net calorific value than those of other alcohols used in the present study. Moreover, similar trends have been indicated by Ning et al. [29] and Silintonga et al. [70]

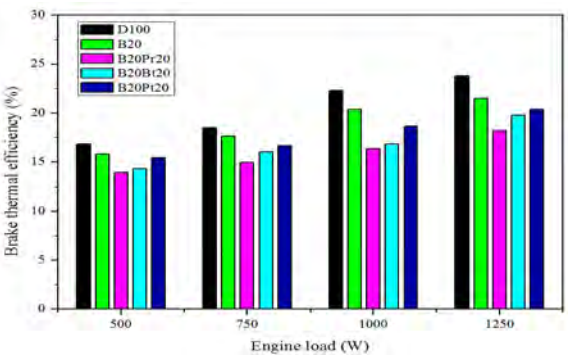

Figure 2. Change of BTE against the engine load

3.1.2. Brake specific fuel consumption

BSFC infers a comparison amongst the fuel quantity extinguished in any engine and the corresponding power generated by the engine. Indeed, it is an important indicator for the efficiency of the fuel consumed of an engine, and therefore, it permits the comparison of fuel efficiency for various engines directly [4]. Fig. 3 portrays the change of BSFC values as a function of load for the tested fuel samples. It is to be noted that BSFC declines with the promotion of the load because it is a good agreement with the fact that larger fuel injection pressure and extended duration provided for fuel to mix in the chamber

of combustion under the elevated loads exists. Based on the before mention, the minimum BSFC values for the tested fuel specimens were encountered to be as the highest load in this work [71, 72]. At 1250 W, BSFC values were calculated as 351.64 g/kWh for D100 and 397.52 g/kWh for B20. As seen, the B20 fuel blend shows a slightly larger BSFC than that of traditional D100. This case is a common inclination for the plenty of the alternative and renewable fuel candidates since they have lesser energy content than that of diesel fuel. It is an important factor to acquire a similar output power from the engine [69]. This can be also explained by the inappropriate atomization behaviors and high spray penetration of biodiesel fuel [73]. It is to be noted that this is led owing to a substantial descending in the net calorific value of the biodiesel fuel and not only its higher viscosity but density values also exhibit a basic role in the consumption of the fuel throughout the engine operation [74]. Moreover, the BSFC results for the ternary blends of 20% (by volume) ratio of isopropanol, 1-butanol, and isopentanol at the highest load are determined to be as 508.51 g/kWh, 458.28 g/kWh, and 437.59 g/kWh, respectively. The BSFC values for B20Pr20, B20Bt20, and B20Pt20 fuel blends were averagely by 41.97%, 32.40%, and 22.15%, respectively higher than that of D100 while averagely by 28.29%, 19.65%, and 10.40%, respectively higher than that of the B20 blend. Noteworthy, it was evident that BSFC values for isopentanol infused ternary blend are lower than those of other ternary blends. This is because of the larger energy amount of the isopentanol than that of tested higher-order alcohols, as shown in first Table. These findings have been a good agreement with the findings put forth by Babu and Anand [75] as well as Devarajan et al. [76].

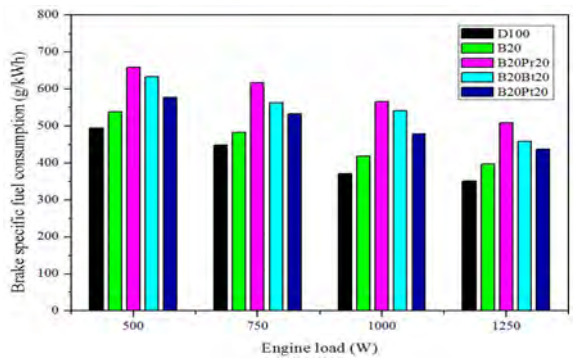

Figure 3. Change of BSFC against the engine load

3.1.3. Exhaust gas temperature

The change of the EGT with respect to the load for various fuels has been demonstrated in Fig. 4. It is anticipated from this research that the maximum EGT values are determined at the peak load operating condition. EGT values are ascended with the increase of the load for whole the fuel specimens [77, 78]. The minimum EGT values for D100, B20, B20Pr20, B20Bt20, and B20Pt20 were observed to be as in the order of 137°C, 121°C, 99°C, 108°C, and 115°C while the maximum EGT values were found to be at 298°C, 263°C, 234°C, 244°C, and 256°C, respectively. As seen, the peak EGT values at all engine loads have occurred with pure diesel fuel. The EGT is a significant indicator that influences the exhaust gas pollutants released from the engine. Normally, EGT can change depending upon the operating conditions of the engine like injection pressure, compression ratio, engine speed, engine load, etc. and specifications of the consumed fuel like net calorific value, viscosity, CN, density, etc. [79]. It is evident from the graph that there is a considerable variation between the experimental findings for the used fuel samples. The supplementation of biodiesel into D100 inspired reductions in EGT values due to lesser energy content of biodiesel [80]. A similar trend was also seen in the ternary blends. The alcohol infusion to the B20 blend has led to a decrease in the values of EGT [81]. The minimum EGT values at all engine loads were observed using isopropanol blended fuel sample because of the net heat capacity of the isopropanol, as presented in Table 1. Among the ternary blends, the maximum values were achieved with isopentanol owing to the above-mentioned reason. The alcohols can draw back the heat energy from the surrounding region because they have high LHV. Hence, EGT values decrease significantly when the test engine powered by the alcohol added fuels [82]. LHV of the tested alcohols can be seen in Table 1 and it can be ordered from highest to the lowest as follows: isopropanol, 1-butanol, and isopentanol. Accordingly, the EGT values can be sorted from highest to the lowest as follows: isopentanol, 1-butanol, and isopropanol. In this way, the EGT alteration was validated. One has not passed without saying the situation that this can be linked to the lower end temperature of the combustion occurred inside the cylinder when diesel engine fuelled with the tested fuel samples that have a high native content of oxygen in the chemical bonds as well as lower heat capacity [56]. It is stated to be in other words that the higher concentration of oxygen amount in the chamber of combustion leads to a decrease in EGT values by improving the combustion efficiency as compared to conventional diesel fuel [81, 83].

3.2. Exhaust emission parameters

This section indicates a comprehensive and detailed discussion on the exhaust gas patterns like carbon monoxide (CO), unburned hydrocarbon (HC), carbon dioxide (CO_2), oxides of nitrogen (NO_X), and smoke opacity measured from the experiments conducting diesel fuel, diesel/biodiesel blend, and ternary blends of alcohol/biodiesel/diesel at desired loads.

3.2.1. Hydrocarbon emissions

The unburned HC of any engine is key evidence of the attribute of the combustion reaction. The factors such

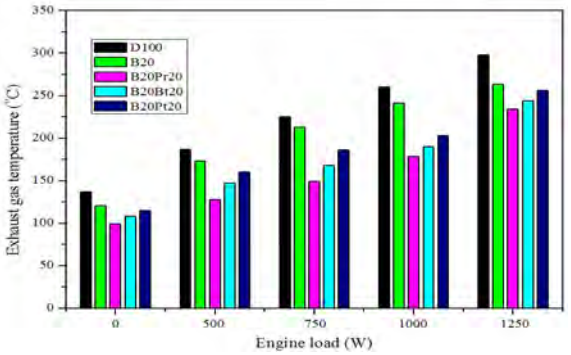

Figure 4. Change of EGT against the engine load

as spray characteristics of the fuel, air/fuel ratio, fuel properties, and engine working circumstances affect unburned HC emission formation inside the cylinder [4, 84]. Fig. 5 depicts the change of HC emissions of the tested fuel samples concerning the loads. As figured out from the illustration, the conventional diesel fuel releases the highest concentration of HC emissions than that of performed fuel samples at entire loads. COME that is an alternative fuel as biodiesel has a native content of oxygen in the chemical structure contrary to mineral diesel fuel. D100 is composed of pure hydrocarbon chains. Similar outcomes have been also reported by many kinds of literature operating with various biodiesel fuelled CI engine [67, 85, 86]. At 1250 W operating conditions, the maximum HC emission for D100, B20, B20Pr20, B20Bt20, and B20Pt20 were found to be at 365.82 ppm, 329.42 ppm, 262.99 ppm, 283.92 ppm, and 296.66 ppm, respectively. On average, B20 fuel blend exhibited a 9.20% reduction in HC emission in comparison with that of D100 while B20Pr20, B20Bt20, and B20Pt20 showed decreases by 30.40%, 22.19%, and 16.20%, respectively. As is well known that the alcohols possess abundant oxygen molecules in their structure and thence they are oxygenated fuel additives for the diesel. Accordingly, isopropanol, 1-butanol, and isopentanol have approximately 26.67%, 21.62%, and 18.18% oxygen content, respectively. By virtue of the entity of a surplus quantity of oxygen molecules inside the chamber of combustion, ternary blends of COME, alcohol, and D100 are contemplated to emit a lower concentration of HC emission during the combustion. In fact, the outcomes coming from the experimentations have been shown that the HC emissions increase by adding higher-order alcohols into the blends. The minimum results were observed with the usage of B20Pr20 whereas the B20Pt20 blend fuel released maximum HC emission to the environment among the ternary blends. It can be attributed to the combined impact of the LHV and the quality of the ignition of the tested alcohols [84]. The higher LHV (as seen in Table 1) causes to retract the heat from the combustion chamber, i.e., quenching effect inside the cylinder [87]. Moreover, a lower CN elongates the ID period. These effects have control over the other influences of blended fuel samples such as improved atomization property which encourages better combustion process inside the chamber of combustion. As the long duration for combusting that decreased auto-ignition properties present for long-chain alcohols blended fuel samples which cause to forms leaner external flame regions in the cylinder resulting in larger HC emissions [42].

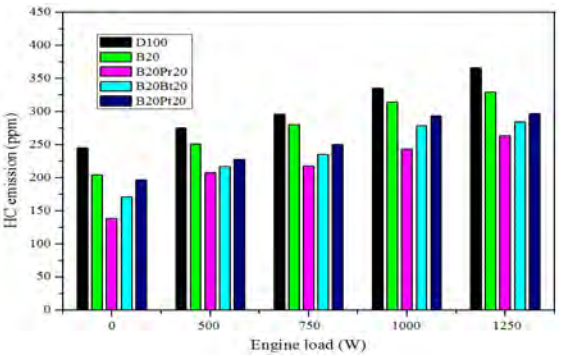

Figure 5. Change of unburned HC emissions against the engine load

3.2.2. Carbon dioxide emission

Fig. 6 illustrates the CO_2 emissions in percentages in accordance with the loads for the tested fuels. It has been clearly determined by monitoring the figure that the engine loads were increased, the CO_2 emission levels violently increased [88]. The aforementioned increase in CO_2 emission patterns can be linked to the rise in BSFC in consequence of BTE with an ascending in engine load. Not interestingly, diesel portrays the lowest CO_2 emissions at entire the engine loads since petroleum-based diesel fuel has high energy content, elevated BTE as well as better atomization characteristics causes to reduce the CO_2 emissions. The long-chain alcohols because of their native oxygen content in the molecular structure react lightly with CO molecules and hence the formation of CO_2 emissions increases [89]. Therefore, it is difficult to say that higher alcohols have little or no effect on CO_2 emissions. The CO_2 emissions for D100, B20, B20Pr20, B20Bt20, and B20Pt20 at 1250 W engine load were noticed to be as 7.15%, 7.42%, 8.64%, 9.00%, and 10.33%, respectively. The lesser viscosity and density values resulting from the alcohol addition to the B20 blend have improved the vaporization process of fuel inside the cylinder and therefore the CO_2 emission was increased [75]. Similar findings have been also obtained in Refs. [90, 91].

3.2.3. Oxides of nitrogen emission

The emissions of NO_X in the exhaust gases of diesel engine composes of heavily nitrogen monoxide (NO) and nitrogen dioxide (NO_2) [92]. The NO_X emissions are affected from several factors such as the oxidation of nitrogen is found in the atmosphere under an elevated temperature of the combustion chamber, the oxidation reaction of nitrogen coming from the fuel chemical structure,

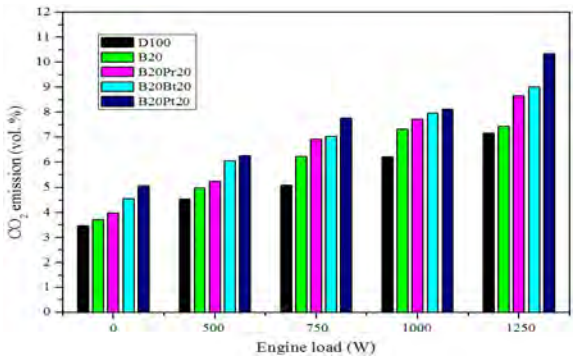

Figure 6. Change of CO_2 emissions against the engine load

through decline on CN group forming intermediate species such as ketones, NO_X, etc. ın other words, the above-mentioned parameters are largely accountable from the increasing the formation of NO_X in CI engines [73]. The alteration of NO_X emissions for the tested fuel samples used in this experimentations with regard to the loading is presented in Fig. 7. Not only as is well known from the literature, but also theoretically, biodiesel fuels have been emitted higher amount of NO_X emissions when compared to the neat D100 on account of the being of inherent oxygen molecules in their molecular bonds [93]. This case can be also validated from the graph given underneath. It was distinct from Fig. 7 that the NO_X emission of the B20 blend was the highest amongst the other all the tested fuels due to the aforementioned reason. At 1250 W operating condition, the NO_X emission of B20 was observed to be as 56.94% which was more than that of D100. It is to be noticed from the measurement that the NO_X emissions raised with the increment in the load and the highest results were obtained at the peak load (1250 W). Namely, the current research showed the NO_X emissions for entire the tested fuel specimens were predicted concerning the brake power. Hence, the increasing inclinations were monitored with the increase in the load. By the way, the lowest NO_X emissions were normally observed with reference fuel (D100). The NO_X emissions for D100, B20, B20Pr20, B20Bt20, and B20Pt20 were averagely measured as 197.11 ppm, 293.20 ppm, 206.39 ppm, 230.96 ppm, and 248.98 ppm, respectively. As observed, the addition of various alcohols to the diesel/biodiesel blend caused to decrease the NO_X pollutants slightly because of the 20% fraction in the blend. It was evident from the figure that the high LHV of alcohol (as given in Table 1) leads to becoming a cooling impact inside the engine cylinder even though an excessive amount of oxygen content is found in the alcohol. Hence, the aforementioned characteristics cause the reduction of the combustion chamber temperature resulting in assist to decline the formation of NO_X emission since the NO_X generation is led by both the abundance of the oxygen molecule in the cylinder and the combustion temperature [94, 95]. On the other hand, from the graph, it can be appeared that the decrement in the NO_X emission is comparatively lower for the B20Pt20 blend as the isopentanol has a higher CN than those of isopropanol and 1-butanol which enhances the combustion process in the cylinder. CN may be correlated with the ID duration of the engine [96]. A higher CN leads to a decrease in the ID period. This subject was also discussed elaborately in the related subsection. The larger ID extends the premixed mode and therefore the peak in-cylinder pressure, as well as, the temperature was increased. It can be concluded that the prolonged ID period and the availability of the excess amount of oxygen molecules with the addition of isopentanol cause a higher amount of NO_X formation. Additionally, the lowest results were obtained with the infusion of isopropanol. This is maybe owing to the higher LHV, lesser calorific value, higher oxygen content, and lesser CN of the isopropanol. Kumar and Saravanan [36] stated that the NO_X emission was higher for long-chain alcohol/diesel fuel blends comparatively because of raising in the LHV and CN of the blend. It can be accomplished that the outcomes for the NO_X emission coming from this study also in accordance with the previously conducted research reports [67, 97, 98].

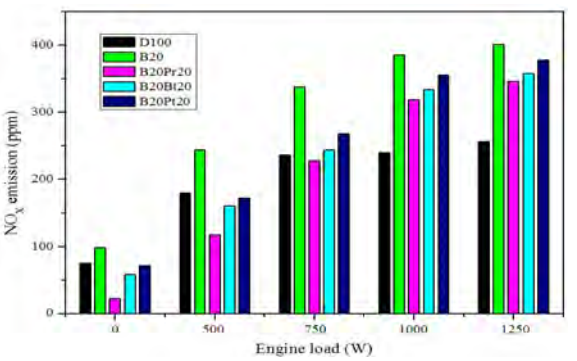

Figure 7. Change of NO_X emissions against the engine load

3.2.4. Carbon monoxide emission

One of the most hazardous exhaust gases that immediately influences the people as well as the environment is the CO emission and it implies the incomplete combustion process [98]. Thus, it is taken to the account as a substantial space in the emission regulation all over the world. The inappropriate injection of fuel inside the cylinder, burning in the shortage of oxygen situations or rich air-fuel mixture are the major features that lead to the formation of CO emission in the cylinder [73]. The variation of CO emission for the used fuel samples in this study according to the load is shown in Fig. 8. Even though the CO emissions of the tested fuels increased with the increase in the load, the figures up to 750 W operating conditions were observed almost similar. This is a common trend for this type of engine that has been monitored in all fixed speed CI engines for different alternative fuel samples as well [99]. This is may be due to the engine is operating with a leaner air/fuel mixture at the lower

loads and the attendance of much more fuel at the highest loads causes to the generation of more fuel-rich regions inside the cylinder [84]. It is evident from Fig. 8 that the petroleum-based diesel fuel released more CO emission at all engine load in comparison with the B20 fuel. This can be briefly explained as the native characteristics of the COME since biodiesel fuels are an oxygenated fuel additive and they have approximately 10-12% oxygen content in their chemical bonds whereas conventional diesel fuel is a mineral petroleum product and consists of the pure hydrocarbon chain [88, 100]. At 1250 W, the CO emissions for D100, B20, B20Pr20, B20Bt20, and B20Pt20 were found to be at 1.31%, 1.09%, 1.39%, 1.52%, and 1.66%, respectively. As seen, the supplementation of alcohol to the diesel/biodiesel blend led to increasing CO emission drastically. This can be mainly because of the longer ID duration resulting from the addition of alcohol. The alcohols have a lower CN (as presented in Table 1) which leads to an increase in the ID period. In other words, a large number of fuel accumulates in the combustion chamber because of lower CN of fuel. Hence, a lot of fuel-rich places in the cylinder occurs resulting, in turn, raise the CO emission [8]. Furthermore, another reason is the elevated LHV of alcohol. This case leads to becoming a quenching impact in the combustion chamber which helps to decrease the temperature of the cylinder resulting in the getting worse the combustion efficiency [52, 101]. When Fig. 8 was evaluated, the isopentanol added fuel sample release more CO emission from the exhaust. This is due to the number of carbon atoms in the chemical structure of alcohol. Table 1 presents the carbon numbers of the alcohols. Namely, the increase in the carbon content of the alcohol put across becoming a higher amount of CO emission formation in accordance with the B20. In addition, the achieved results have been consistent with the previous researches [102, 103]

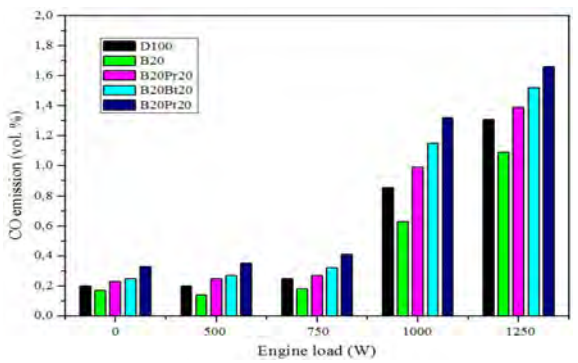

Figure 8. Change of CO emissions against the engine load

3.2.5. Smoke opacity

Smoke opacity, the only visible exhaust gas, is a characteristic that performs the optical properties of exhaust gases of diesel engines. The main reason for the formation of smoke opacity is that large-sized fuel particles forming the fuel-rich places inside the chamber of combustion cause the formation of unburned fuel particles in the exhaust gases [73]. In this direction, the change of smoke opacity results for the tested fuel samples against the several loads is represented in Fig. 9. It is to be noticed from the graph that the smoke opacity is in turn raised with the rise of the engine load for all the tested fuels. Moreover, the maximum figures were observed at the peak load of 1250 W. It is seen that D100 generated the utmost smoke intensity results among the tested fuels at entire the loads. When the tested CI engine run on the biodiesel fuel blend, the smoke opacity values dropped at all loads and the outcomes are good agreement with the conducted experiments from various researchers [104, 105]. The main reason for this trend is the capability of fine combustion process resulting in the reduction of the smoke opacity. It is noteworthy to notice that the smoke opacity results for all the tested ternary alternative blends were lesser than those of pure D100 and B20. At 1250 W, the smoke opacity values for D100, B20, B20Pr20, B20Bt20, and B20Pt20 were found to be at 74.0%, 72.0%, 71.2%, 70.5%, and 69.6%, respectively. As appeared, the addition of alcohols having various chain lengths led to mitigating the smoke opacity strictly with respect to the D100. Accordingly, this is due to the wealth of the native oxygen concentration of the alcohols which may result in smoke emission decreasing [102]. Remarkably, the smoke opacity for the isopropanol blend is slightly lower than that of the B20 blend at the maximum engine load. This might be grounded to the course of the isopropanol being somewhat chain length that means include much more oxygen molecules in its structure than the others leading to becoming a cooling effect inside the cylinder. The opposite of this situation can be clearly said to occur with isopentanol. Kumar et al. [37] have indicated that the smoke opacity for a CI engine might be rearranged thanks to using long-chain alcohol infusion as a fuel additive.

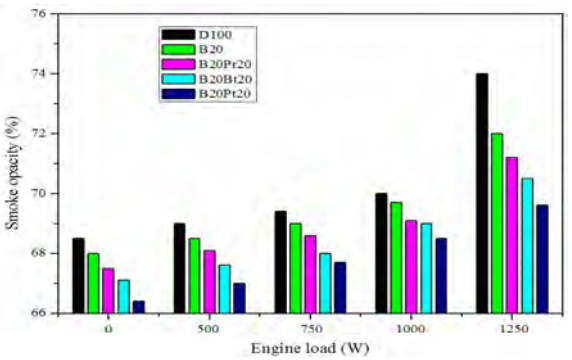

Figure 9. Change of smoke emissions against the engine load

CONCLUSION

In the present experimental research, a comprehensive study has been conducted on in a single-cylinder, four-stroke, naturally-aspirated, DI diesel engine using higher-

order alcohols like isopropanol-C3, 1-butanol-C4, and isopentanol-C5 as alternative fuel additives with D100 and COME as ternary blends at various engine loads (0, 500, 750, 1000, and 1250 W) and a constant engine speed. The concentration of alcohol, as well as biodiesel, was maintained to be 20% since obtaining stable engine operation during the experimentations. Moreover, the physicochemical characteristics of these prepared ternary blends set out that they could be utilized as alternative fuels in the CI engine when blended with COME and diesel fuel. Based on the experimental investigation, the following conclusions are found.

- BTE of ternary blends is lower than those of D100 and B20 due to the lower calorific value of alcohol. The BTE outcomes increased with the addition of higher-order alcohols in terms of the increase in the number of the carbon atoms, and hence, 20% isopentanol exhibits the highest BTE by 20.36% among the ternary blends.

- On the other hand, BSFC for the tested ternary blends is found to be higher than those of pure D100 and B20 fuel blend because of the aforementioned reason. In contrast to the BTE inclination, BSFC is observed to be the utmost for B20Pr20 among all the tested fuels. It implies that with the usage of higher carbon chained alcohol in the mixture, BSFC reduces on account of the higher net calorific value of long-chain alcohols.

- As far as the EGT results are taken into consideration, the maximum EGT values for D100, B20, B20Pr20, B20Bt20, and B20Pt20 at the maximum load were noted to be as 298°C, 263°C, 234°C, 244°C, and 256°C, respectively. A lower energy content resulting in lower heat energy and higher LHV leading to decrease cylinder temperature due to the quenching effect caused to decrease the EGT when the test engine fuelled with the alcohol-infused alternative fuel blends.

- The unburned HC and smoke opacity emissions for the ternary blends were concerned, it is to be noted that there is a sharp decrement due to the addition of higher alcohols having elevated inherent oxygen molecules in their molecular structures resulting in improved fuel atomization characteristics.

- The CO_2 emissions for D100, B20, B20Pr20, B20Bt20, and B20Pt20 at 1250 W engine load were determined to be as 7.15%, 7.42%, 8.64%, 9.00%, and 10.33%, respectively.
- During the experimentation, the reduction in the NO_X emissions for B20Pr20, B20Bt20, and B20Pt20 at all loads with respect to the B20 blend were recorded, but, the results still higher than that of pure D100.

Overall, it can be accomplished that the addition of higher-order alcohol like isopropanol, 1-butanol, and isopentanol as fuel additives with diesel/COME may be assessed as the potential alternative fuel blends for the CI engine application. However, many kinds of research are necessary to be performed in long term usage in present engines such as vehicle engines, diesel generator, etc. prior to the considering as a commercial meaning.

REFERENCES

1. Kalam MA, Masjuki HH, Jayed MH, Liaquat AM. Emission and performance characteristics of an indirect ignition diesel engine fuelled with waste cooking oil. Energy 36(1) (2011) 397–402.
2. fe Ş, Ceviz MA, Temur H. Comparative engine characteristics of biodiesels from hazelnut, corn, soybean, canola and sunflower oils on DI diesel engine. Renewable Energy 119 (2018) 142–151.
3. Ashok B, Ashok SD, Kumar CR. LPG diesel dual fuel engine–A critical review. Alexandria Engineering Journal 54(2) (2015) 105–126.
4. Ashok B, Nanthagopal K, Saravanan B, Azad K, Patel D, Sudarshan B, Ramasamy RA. Study on isobutanol and Calophyllum inophyllum biodiesel as a partial replacement in CI engine applications. Fuel 235 (2019) 984–994.
5. Keskin A, Sağıroğlu S. Exhaust emissions originated diesel engines and their control methods. Engineer and Machinery 51(606) (2010) 2–9. (in Turkish)
6. Yilmaz N. Performance and emission characteristics of a diesel engine fuelled with biodiesel–ethanol and biodiesel–methanol blends at elevated air temperatures. Fuel 94 (2012) 440–443.
7. Aytav E, Kocar G. Biodiesel from the perspective of Turkey: Past, present and future. Renewable and Sustainable Energy Reviews 25 (2013) 335–350.
8. Atmanli A. Comparative analyses of diesel–waste oil biodiesel and propanol, n-butanol or 1-pentanol blends in a diesel engine. Fuel 176 (2016) 209–215.
9. Jin C, Pang X, Zhang X, Wu S, Ma M, Xiang Y, Ma J, Ji J, Wang G, Liu H. Effects of C3–C5 alcohols on solubility of alcohols/diesel blends. Fuel 236 (2019) 65–74.
10. Rajak U, Verma TN. Effect of emission from ethylic biodiesel of edible and non-edible vegetable oil, animal fats, waste oil and alcohol in CI engine. Energy Conversion and Management 166 (2018) 704–718.
11. Singh SP, Singh D. Biodiesel production through the use of different sources and characterization of oils and their esters as the substitute of diesel: A review. Renewable and Sustainable Energy Reviews 14 (2010) 200–216.
12. Chauhan BS, Singh RK, Cho HM, Lim HC. Practice of diesel fuel blends using alternative fuels: A review. Renewable and Sustainable Energy Reviews 59 (2016) 1358–1368.
13. Moka S, Pande M, Rani M, Gakhar R, Sharma M, Rani J, Bhaskarwar AN. Alternative fuels: an overview of current trends and scope for future. Renewable and Sustainable Energy Reviews 32 (2014) 697–712.
14. Atmanli A. Effects of a cetane improver on fuel properties and engine characteristics of a diesel engine fueled with the blends of diesel, hazelnut oil and higher carbon alcohol. Fuel 172 (2016) 209–217.
15. Abdullah AZ, Salamatinia B, Mootabadi H, Bhatia S. Current status and policies on biodiesel industry in Malaysia as the world's leading producer of palm oil. Energy Policy 37(12) (2009) 5440–5448.

16. Agarwal AK. Biofuels (alcohols and biodiesel) applications as fuels for internal combustion engines. Progress in Energy and Combustion Science 33(3) (2007) 233–271.
17. Atabani AE, Silitonga AS, Badruddin IA, Mahlia TMI, Masjuki HH, Mekhilef S. A comprehensive review on biodiesel as an alternative energy resource and its characteristics. Renewable and Sustainable Energy Reviews 16(4) (2012) 2070–2093.
18. Lin L, Cunshan Z, Vittayapadung S, Xiangqian S, Mingdong D. Opportunities and challenges for biodiesel fuel. Applied Energy 88(4) (2011) 1020–1031.
19. Sharma YC, Singh B, Upadhyay SN. Advancements in development and characterization of biodiesel: A review. Fuel 87(12) (2008) 2355–2373.
20. Atzemi M, Lois E, Kosyfologou I. Effects of biodiesel and hydrotreated vegetable oil on the performance and exhaust emissions of a stationary diesel engine. IOSR Journal of Applied Chemistry 12(1) (2019) 44–54.
21. Ooi XY, Gao W, Ong HC, Lee HV, Juan JC, Chen WH, Lee KT. Overview on catalytic deoxygenation for biofuel synthesis using metal oxide supported catalysts. Renewable and Sustainable Energy Reviews 112 (2019) 834–852.
22. Yesilyurt MK, Yilbasi Z, Aydin M. The performance, emissions, and combustion characteristics of an unmodified diesel engine running on the ternary blends of pentanol/safflower oil biodiesel/diesel fuel. Journal of Thermal Analysis and Calorimetry (2020) 1-40.
23. Atmanli A, Ileri E, Yuksel B, Yilmaz N. Extensive analyses of diesel–vegetable oil–n-butanol ternary blends in a diesel engine. Applied Energy 145 (2015) 155–162.
24. Gülüm M, Bilgin A. A comprehensive study on measurement and prediction of viscosity of biodiesel-diesel-alcohol ternary blends. Energy 148 (2018) 341–361.
25. Ibrahim A. Performance and combustion characteristics of a diesel engine fuelled by butanol–biodiesel–diesel blends. Applied Thermal Engineering 103 (2016) 651–659.
26. Yilmaz N, Atmanli A, Vigil FM. Quaternary blends of diesel, biodiesel, higher alcohols and vegetable oil in a compression ignition engine. Fuel 212 (2018) 462–469.
27. Hulwan DB, Joshi SV. Performance, emission and combustion characteristic of a multicylinder DI diesel engine running on diesel–ethanol–biodiesel blends of high ethanol content. Applied Energy 88(12) (2011) 5042–5055.
28. Çelebi Y, Aydın H. An overview on the light alcohol fuels in diesel engines. Fuel 236 (2019) 890–911.
29. Ning L, Duan Q, Chen Z, Kou H, Liu B, Yang B, Zeng K. A comparative study on the combustion and emissions of a non-road common rail diesel engine fueled with primary alcohol fuels (methanol, ethanol, and n-butanol)/diesel dual fuel. Fuel 266 (2020) 117034.
30. Jamrozik A, Tutak W, Gnatowska R, Nowak Ł. Comparative analysis of the combustion stability of diesel-methanol and diesel-ethanol in a dual fuel engine. Energies 12(6) (2019) 971.
31. Dabas N, Dubey V, Chhabra M, Dwivedi G. Performance analysis of an IC engine using methanol, ethanol, and its blend with gasoline and diesel as a fuel. In Advances in Fluid and Thermal Engineering (2019) 223–232.
32. Kwanchareon P, Luengnaruemitchai A, Jai-In S. Solubility of a diesel–biodiesel–ethanol blend, its fuel properties, and its emission characteristics from diesel engine. Fuel 86(7-8) (2007) 1053–1061.
33. Shahir SA, Masjuki HH, Kalam MA, Imran A, Fattah IR, Sanjid A. Feasibility of diesel–biodiesel–ethanol/bioethanol blend as existing CI engine fuel: An assessment of properties, material compatibility, safety and combustion. Renewable and Sustainable Energy Reviews 32 (2014) 379–395.
34. Lei J, Shen L, Bi Y, Chen H. A novel emulsifier for ethanol–diesel blends and its effect on performance and emissions of diesel engine. Fuel 93 (2012) 305–311.
35. Al-Hassan M, Mujafet H, Al-Shannag M. An Experimental study on the solubility of a diesel-ethanol blend and on the performance of a diesel engine fueled with diesel-biodiesel-ethanol blends. Jordan Journal of Mechanical & Industrial Engineering 6(2) (2012) 147–153.
36. Kumar BR, Saravanan S. Use of higher alcohol biofuels in diesel engines: A review. Renewable and Sustainable Energy Reviews 60 (2016) 84–115.
37. Kumar BR, Saravanan S, Rana D, Nagendran A. A comparative analysis on combustion and emissions of some next generation higher-alcohol/diesel blends in a direct-injection diesel engine. Energy Conversion and Management 119 (2016) 246–256.
38. Yogesh P, Sakthi SD, Aravinth C, Sathiyakeerthy K, Susenther M. Performance test on diesel-biodiesel–propanol blended fuels in CI engine. International Journal of Innovative Science and Research Technology 3(2) (2018) 294–299.
39. Şen M. The effect of the injection pressure on single cylinder diesel engine fueled with propanol–diesel blend. Fuel 254 (2019) 115617.
40. Muthaiyan P, Gomathinayagam S. Combustion characteristics of a diesel engine using propanol diesel fuel blends. Journal of the Institution of Engineers (India): Series C 97(3) (2016) 323–329.
41. Kumar BR, Muthukkumar T, Krishnamoorthy V, Saravanan S. A comparative evaluation and optimization of performance and emission characteristics of a DI diesel engine fueled with n-propanol/diesel, n-butanol/diesel and n-pentanol/diesel blends using response surface methodology. RSC Advances 6(66) (2016) 61869–61890.
42. Kumar BR, Saravanan S. Effects of iso-butanol/diesel and n-pentanol/diesel blends on performance and emissions of a DI diesel engine under premixed LTC (low temperature combustion) mode. Fuel 170 (2016) 49–59.
43. Zhang ZH, Chua SM, Balasubramanian R. Comparative evaluation of the effect of butanol–diesel and pentanol–diesel blends on carbonaceous particulate composition and particle number emissions from a diesel engine. Fuel 176 (2016) 40–47.
44. Saravanan S, Kumar BR, Varadharajan A, Rana D, Sethuramasamyraja B. Optimization of DI diesel engine parameters fueled with iso-butanol/diesel blends–response surface methodology approach. Fuel 203 (2017) 658–670.
45. Ganesh D, Ayyappan PR, Murugan R. Experimental investigation of iso-butanol/diesel reactivity controlled compression ignition combustion in a non-road diesel engine. Applied Energy 242 (2019) 1307–1319.
46. Wei M, Li S, Xiao H, Guo G. Combustion performance and pollutant emissions analysis using diesel/gasoline/iso-butanol blends in a diesel engine. Energy Conversion and Management 149 (2017) 381–391.
47. Zhang ZH, Balasubramanian R. Physicochemical and toxicological characteristics of particulate matter emitted from a non-road diesel engine: Comparative evaluation of biodiesel-diesel and butanol-diesel blends. Journal of Hazardous Materials 264 (2014) 395–402.
48. Yilmaz N, Vigil FM, Benalil K, Davis SM, Calva A. Effect of biodiesel–butanol fuel blends on emissions and performance characteristics of a diesel engine. Fuel 135 (2014) 46–50.
49. Işık MZ, Bayındır H, Iscan B, Aydın H. The effect of n-butanol additive on low load combustion, performance and emissions of biodiesel-diesel blend in a heavy duty diesel power generator. Journal of the Energy Institute 90(2) (2017) 174–184.
50. Campos-Fernández J, Arnal JM, Gómez J, Dorado MP. A

comparison of performance of higher alcohols/diesel fuel blends in a diesel engine. Applied Energy 95 (2012) 267–275.
51. Li L, Wang J, Wang Z, Xiao J. Combustion and emission characteristics of diesel engine fueled with diesel/biodiesel/pentanol fuel blends. Fuel 156 (2015) 211–218.
52. Li L, Wang J, Wang Z, Liu H. Combustion and emissions of compression ignition in a direct injection diesel engine fueled with pentanol. Energy 80 (2015) 575–581.
53. Yang K, Wei L, Cheung CS, Tang C, Huang Z. The effect of pentanol addition on the particulate emission characteristics of a biodiesel operated diesel engine. Fuel 209 (2017) 132–140.
54. Santhosh K, Kumar GN. Effect of 1-pentanol addition and EGR on the combustion, performance and emission characteristic of a CRDI diesel engine. Renewable Energy 145 (2020) 925–936.
55. Sridhar R, Jeevahan J, Chandrasekaran M. Effect of the addition of 1-pentanol on engine performance and emission characteristics of diesel and biodiesel fuelled single cylinder diesel engine. International Journal of Ambient Energy 41(1) (2020) 58–63.
56. Ghadikolaei MA, Cheung CS, Yung KF. Study of combustion, performance and emissions of diesel engine fueled with diesel/biodiesel/alcohol blends having the same oxygen concentration. Energy 157 (2018) 258–269.
57. Yilmaz N, Ileri E, Atmanli A. Performance of biodiesel/higher alcohols blends in a diesel engine. International Journal of Energy Research 40(8) (2016) 1134–1143.
58. Atmanli A, Yilmaz N. An experimental assessment on semi-low temperature combustion using waste oil biodiesel/C3-C5 alcohol blends in a diesel engine. Fuel 260 (2020) 116357.
59. Yesilyurt MK, Aydin M. Experimental investigation on the performance, combustion and exhaust emission characteristics of a compression-ignition engine fueled with cottonseed oil biodiesel/diethyl ether/diesel fuel blends. Energy Conversion and Management 205 (2020) 112355.
60. Verma P, Dwivedi G, Behura AK, Patel DK, Verma TN, Pugazhendhi A. Experimental investigation of diesel engine fuelled with different alkyl esters of Karanja oil. Fuel 275 (2020) 117920.
61. Shrivastava P, Salam S, Verma TN, Samuel OD. Experimental and empirical analysis of an IC engine operating with ternary blends of diesel, karanja and roselle biodiesel. Fuel 262 (2020) 116608.
62. Shrivastava P, Verma TN, Pugazhendhi A. An experimental evaluation of engine performance and emisssion characteristics of CI engine operated with Roselle and Karanja biodiesel. Fuel 254 (2019) 115652.
63. Singh TS, Verma TN. Taguchi design approach for extraction of methyl ester from waste cooking oil using synthesized CaO as heterogeneous catalyst: Response surface methodology optimization. Energy Conversion and Management 182 (2019) 383–397.
64. Rajak U, Nashine P, Singh TS, Verma TN. Numerical investigation of performance, combustion and emission characteristics of various biofuels. Energy Conversion and Management 156 (2018) 235–252.
65. Rajak U, Nashine P, Verma TN, Pugazhendhi A. Alternating the environmental benefits of Aegle-diesel blends used in compression ignition. Fuel 256 (2019) 115835.
66. Rakopoulos DC, Rakopoulos CD, Giakoumis EG, Dimaratos AM, Kyritsis DC. Effects of butanol–diesel fuel blends on the performance and emissions of a high-speed DI diesel engine. Energy Conversion and Management 51(10) (2010) 1989–1997.
67. Ramesh A, Ashok B, Nanthagopal K, Pathy MR, Tambare A, Mali P, Phuke P, Patil S, Subbarao R. Influence of hexanol as additive with Calophyllum Inophyllum biodiesel for CI engine applications. Fuel 249 (2019) 472–485.
68. Prakash T, Geo VE, Martin LJ, Nagalingam B. Effect of ternary blends of bio-ethanol, diesel and castor oil on performance, emission and combustion in a CI engine. Renewable Energy 122 (2018) 301–309.
69. Ors I, Kahraman A, Ciniviz M. Performance, emission and combustion analysis of a compression ignition engine using biofuel blends. Thermal Science 21(1 Part B) (2017) 511–522.
70. Silitonga AS, Masjuki HH, Ong HC, Sebayang AH, Dharma S, Kusumo F, Siswantoro J, Milano J, Daud K, Mahlia TMI, Chen WH, Sugiyanto B. Evaluation of the engine performance and exhaust emissions of biodiesel-bioethanol-diesel blends using kernel-based extreme learning machine. Energy 159 (2018) 1075–1087.
71. Emiroğlu AO, Şen M. Combustion, performance and emission characteristics of various alcohol blends in a single cylinder diesel engine. Fuel 212 (2018) 34–40.
72. Qi DH, Chen H, Geng LM, Bian YZ. Experimental studies on the combustion characteristics and performance of a direct injection engine fueled with biodiesel/diesel blends. Energy Conversion and Management 51(12) (2010) 2985–2992.
73. Ashok B, Nanthagopal K, Darla S, Chyuan OH, Ramesh A, Jacob A, Sahil G, Thiyagarajan S, Geo VE. Comparative assessment of hexanol and decanol as oxygenated additives with calophyllum inophyllum biodiesel. Energy 173 (2019) 494–510.
74. Leite D, Santos RF, Bassegio D, de Souza SNM, Secco D, Gurgacz F, da Silva TRB. Emissions and performance of a diesel engine affected by soybean, linseed, and crambe biodiesel. Industrial Crops and Products 130 (2019) 267–272.
75. Babu D, Anand R. Effect of biodiesel-diesel-n-pentanol and biodiesel-diesel-n-hexanol blends on diesel engine emission and combustion characteristics. Energy 133 (2017) 761–776.
76. Devarajan Y, Nagappan BK, Munuswamy DB. Performance and emissions analysis on diesel engine fuelled with cashew nut shell biodiesel and pentanol blends. Korean Journal of Chemical Engineering 34(4) (2017) 1021–1026.
77. Venu H, Subramani L, Raju VD. Emission reduction in a DI diesel engine using exhaust gas recirculation (EGR) of palm biodiesel blended with TiO2 nano additives. Renewable Energy 140 (2019) 245–263.
78. Yilmaz N. Comparative analysis of biodiesel–ethanol–diesel and biodiesel–methanol–diesel blends in a diesel engine. Energy 40(1) (2012) 210–213.
79. Candan F, Ciniviz M, Ors I. Effect of cetane improver addition into diesel fuel: Methanol mixtures on performance and emissions at different injection pressures. Thermal Science 21(1 Part B) (2017) 555–566.
80. An H, Yang WM, Chou SK, Chua KJ. Combustion and emissions characteristics of diesel engine fueled by biodiesel at partial load conditions. Applied Energy 99 (2012) 363–371.
81. Yesilyurt MK, Eryilmaz T, Arslan M. A comparative analysis of the engine performance, exhaust emissions and combustion behaviors of a compression ignition engine fuelled with biodiesel/diesel/1-butanol (C4 alcohol) and biodiesel/diesel/n-pentanol (C5 alcohol) fuel blends. Energy 165 (2018) 1332–1351.
82. Žaglinskis J, Lukács K, Bereczky Á. Comparison of properties of compression ignition engine operating on diesel–biodiesel blend with methanol additive. Fuel 170 (2016) 245–253.
83. Rakopoulos CD, Antonopoulos KA, Rakopoulos DC. Experimental heat release analysis and emissions of a HSDI diesel engine fueled with ethanol–diesel fuel blends. Energy 32(10) (2007) 1791–1808.
84. Ashok B, Jeevanantham AK, Nanthagopal K, Saravanan B, Kumar MS, Johny A, Mohan A, Kaisan MU, Abubakar S. An experimental analysis on the effect of n-pentanol-Calophyllum Inophyllum

Biodiesel binary blends in CI engine characteristcis. Energy 173 (2019) 290–305.
85. Joy N, Devarajan Y, Nagappan B, Anderson A. Exhaust emission study on neat biodiesel and alcohol blends fueled diesel engine. Energy Sources Part A 40(1) (2018) 115–119.
86. Balan KN, Yashvanth U, Booma Devi P, Arvind T, Nelson H, Devarajan Y. Investigation on emission characteristics of alcohol biodiesel blended diesel engine. Energy Sources Part A 41(15) (2019) 1879–1889.
87. Nabi MN, Zare A, Hossain FM, Bodisco TA, Ristovski ZD, Brown RJ. A parametric study on engine performance and emissions with neat diesel and diesel-butanol blends in the 13-Mode European Stationary Cycle. Energy Conversion and Management 148 (2017) 251–259.
88. Uyumaz A. Combustion, performance and emission characteristics of a DI diesel engine fueled with mustard oil biodiesel fuel blends at different engine loads. Fuel 212 (2018) 256–267.
89. Imdadul HK, Masjuki HH, Kalam MA, Zulkifli NWM, Alabdulkarem A, Rashed MM, Teoh YH, How HG. Higher alcohol-biodiesel-diesel blends: An approach for improving the performance, emission, and combustion of a light-duty diesel engine. Energy Conversion and Management 111 (2016) 174–185.
90. Imdadul HK, Masjuki HH, Kalam MA, Zulkifli NWM, Alabdulkarem A, Kamruzzaman M, Rashed MM. A comparative study of C4 and C5 alcohol treated diesel-biodiesel blends in terms of diesel engine performance and exhaust emission. Fuel 179 (2016) 281–288.
91. Ramakrishnan P, Kasimani R, Peer MS, Rajamohan S. Assessment of n-pentanol/Calophyllum inophyllum/diesel blends on the performance, emission, and combustion characteristics of a constant-speed variable compression ratio direct injection diesel engine. Environmental Science and Pollution Research 25(14) (2018) 13731–13744.
92. Palash SM, Kalam MA, Masjuki HH, Masum BM, Fattah IR, Mofijur M. Impacts of biodiesel combustion on NOx emissions and their reduction approaches. Renewable and Sustainable Energy Reviews 23 (2013) 473–490.
93. Uyaroğlu A, Uyumaz A, Çelikten İ. Comparison of the combustion, performance, and emission characteristics of inedible Crambe abyssinica biodiesel and edible Hazelnut, Corn, soybean, sunflower, and Canola biodiesels. Environmental Progress & Sustainable Energy 37(4) (2018) 1438–1447.
94. Zhu L, Cheung CS, Zhang WG, Huang Z. Combustion, performance and emission characteristics of a DI diesel engine fueled with ethanol–biodiesel blends. Fuel 90(5) (2011) 1743–1750.
95. Siwale L, Kristóf L, Adam T, Bereczky A, Mbarawa M, Penninger A, Kolesnikov A. Combustion and emission characteristics of n-butanol/diesel fuel blend in a turbo-charged compression ignition engine. Fuel 107 (2013) 409–418.
96. Yilmaz N, Atmanli A. Experimental evaluation of a diesel engine running on the blends of diesel and pentanol as a next generation higher alcohol. Fuel 210 (2017) 75–82.
97. Anbarasu A, Saravanan M, Loganathan M. The effect of ethanol addition in a biodiesel operated DI diesel engine on combustion, performance, and emission characteristics. International Journal of Green Energy 10(1) (2013) 90–102.
98. Çelik M, Örs İ, Bayindirli C, Demiralp M. Experimental investigation of impact of addition of bioethanol in different biodiesels, on performance, combustion and emission characteristics. Journal of Mechanical Science and Technology 31(11) (2017) 5581–5592.
99. Dhanasekaran R, Krishnamoorthy V, Rana D, Saravanan S, Nagendran A, Kumar BR. A sustainable and eco-friendly fueling approach for direct-injection diesel engines using restaurant yellow grease and n-pentanol in blends with diesel fuel. Fuel 193 (2017) 419–431.
100. Zheng M, Mulenga MC, Reader GT, Wang M, Ting DS, Tjong J. Biodiesel engine performance and emissions in low temperature combustion. Fuel 87(6) (2008) 714–722.
101. Wei L, Cheung CS, Huang Z. Effect of n-pentanol addition on the combustion, performance and emission characteristics of a direct-injection diesel engine. Energy 70 (2014) 172–180.
102. Kumar BR, Saravanan S. Effect of exhaust gas recirculation (EGR) on performance and emissions of a constant speed DI diesel engine fueled with pentanol/diesel blends. Fuel 160 (2015) 217–226.
103. Karabektas M, Hosoz M. Performance and emission characteristics of a diesel engine using isobutanol–diesel fuel blends. Renewable Energy 34(6) (2009) 1554–1559.
104. Tan PQ, Hu ZY, Lou DM, Li ZJ. Exhaust emissions from a light-duty diesel engine with Jatropha biodiesel fuel. Energy 39(1) (2012) 356–362.
105. Tsolakis A, Megaritis A, Wyszynski ML, Theinnoi K. Engine performance and emissions of a diesel engine operating on diesel-RME (rapeseed methyl ester) blends with EGR (exhaust gas recirculation). Energy 32(11) (2007) 2072–2080.

Hittite Journal of Science and Engineering, 2020, 7 (2) 149-155
ISSN NUMBER: 2148-4171
DOI: 10.17350/HJSE19030000183

Production of 20 mm Thick API PSL 2 X60 and X70 Grade Plates from a Nb-Ti Microalloyed Steel

Erkan Konca
Atilim University, Department of Metallurgical and Materials Engineering, Ankara, Turkey

ABSTRACT

This study was undertaken to determine the controlled rolling and cooling conditions for the production of 20 mm thick American Petroleum Institute (API) X60 and X70 grade steel plates. Nb-Ti microalloyed steel slabs of 200 mm thickness were rolled at four different finish rolling temperatures (conventional, 950°C, 850°C and 800°C). In some trials, a water table was employed to provide accelerated cooling just after finish rolling. Mechanical tests (tensile, impact and drop weight tear-DWTT) and microstructural examinations were performed on the samples taken from the trial production plates. Fine grained and essentially ferritic microstructures with strength values satisfying the minimum yield strength requirement of 415 MPa for the API X60 grade were easily obtained in all rolling conditions. However, the minimum yield strength requirement of 485 MPa for the API X70 grade was reached only when accelerated cooling was applied after finish rolling. The minimum 85% shear fracture required by the DWTT of the API PSL 2 specification could be met when the finish rolling temperature was lowered or when accelerated cooling was applied regardless of the finish rolling temperature.

Keywords:
Controlled rolling, API X60, API X70, Accelerated cooling, Pipeline steel, DWTT

Article History:
Received: 2020/04/01
Accepted: 2020/06/12
Online: 2020/06/26

***Correspondence to**: Erkan Konca*
Atilim University, Department of Metallurgical and Materials Engineering, Ankara, Turkey
E-mail: erkan.konca@atilim.edu.tr
Tel: +90 (312) 586 8785

INTRODUCTION

There are currently hundreds of thousands of kilometers long petroleum and natural gas pipelines installed worldwide and new lines are being installed continuously [1, 2]. As the demand for petroleum and natural gas by the developed and developing countries has increased over time, the pipelines of larger diameter pipes that can work at higher operating pressures were required [2, 3]. This necessitated the development of steel plates with higher mechanical properties from which these pipes could be produced [4].

Pipeline steels should have high weldability since pipelines are installed by joining pipes to each other by welding. For this reason, pipeline steels must have low carbon content and low carbon equivalent values and this essentially implies ferritic microstructures [5, 6]. As a way of having high strength, high ductility and high weldability at the same time, grain size refinement mechanism is utilized in pipeline steels. By decreasing the ferrite grain size, both strength and toughness can be simultaneously increased without increasing the carbon content of the steel [5]. Pipeline steels also contain low amounts of alloying elements that are mainly added due to their roles in decreasing the ferrite grain size. Therefore, these steels are grouped under high strength low alloy (HSLA) steels [6, 7].

Throughout the world, the specifications established by American Petroleum Institute (API) are followed for the petroleum and natural gas pipelines. API Specification 5L classifies pipelines steels according to their required yield strength values [8]. For example, API X52 corresponds to a minimum yield strength requirement of 52200 psi. API grades X52 to X70 were developed during the 1950s to 1970s, while newer grades, X80 to X120, were adopted later [9, 10].

Based on the required properties, API 5L classifies pipeline steels in two main product specification levels as PSL 1 and PSL 2. The main difference between PSL 1 and PSL 2 specifications is towards the deformation

behavior of the steel rather than its strength. As compared to the PSL 1, PSL 2 has additional impact and ductility requirements. Some of the mechanical property requirements for the API X60 and X70 grades that constitute the focus of this study are given in Table 1.

Table 1. Some mechanical property requirements for the API X60 and X70 grade steels based on the API 5L PSL 1/PSL 2 specification [8].

Grade	Yield Strength (MPa)	Tensile Strength (MPa)	YS/TS Ratio (max)	% Elongation (min)	Impact Energy* at 0°C (J, min)	DWTT**
PSL 1 X60	min. 415	min. 520	-	24	-	
PSL 1 X70	min. 485	min. 570	-	22	-	
PSL 2 X60	415-565	520-760	0.93	24	27-54	≥ 85 %
PSL 2 X70	485-635	570-760	0.93	22	40-68	≥ 85 %

*Required impact energy depends on the outer diameter of the pipe and the wall thickness.
**Drop Weight Tear Test (DWTT) is used to determine the degree of shear fracture.

The development of steel plates with superior mechanical properties to be used in pipelines became possible by utilizing the rolling operation not only for reducing slabs to the specified thickness but also for creating the microstructures that would produce the targeted mechanical properties. Controlled rolling or Thermomechanical Controlled Rolling (TCR) covers the selection of rolling temperatures, reduction ratios and rolling speeds considering the microstructural evolution behavior (kinetics of phase transformations, recrystallization, grain growth, and precipitation reactions, etc.) of the steel to obtain the desired microstructures [4, 6].

In typical rolling operations, the overall reduction in thickness is accomplished in two main stages, namely rough rolling and finish rolling. Conventionally, shaping is performed in successive passes where the rolling load per pass is kept at low values and rough rolling is followed by the finish rolling without any intentional waiting time in between. Hence, the whole shaping process is completed at high temperatures.

In controlled rolling, however, finish rolling is done at lower temperatures in order to prevent or minimize the recrystallization and grain growth of the deformed austenite so that the number of sites for ferrite nucleation is maximized. Therefore, there is an intentionally given waiting time between the rough and finish rolling stages, which is needed for the cooling of the steel being rolled. Inevitably, rolling at lower temperatures brings higher loads to rolls as compared to the conventional rolling since the flow strength of the steel is higher at lower temperatures [11]. The other concern caused by the waiting time between the rough and finish rolling stages is that the throughput of the rolling mill decreases with increasing waiting time and this means higher cost per produced plate.

The temperature below which austenite does not recrystallize is called non-recrystallization temperature (T_{nr}). When the finish rolling is performed below the T_{nr}, the nucleation of ferrite occurs while the deformed austenite grains are in the pancake form and thus, there are a lot of nucleation sites available (austenite grain boundaries and deformation bands) for a given volume [12]. Hence, microstructures consisting of finer ferrite grains can be obtained (Fig. 1).

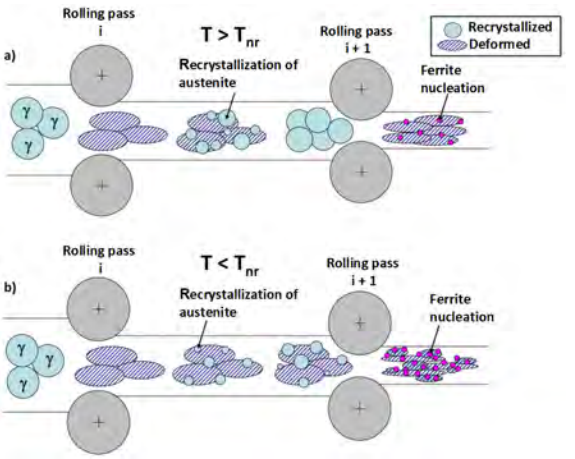

Figure 1. The effect of rolling a) above and b) below the Tnr temperature. The austenite grains deformed below the T_{nr} take pancake form and they provide a higher number of nucleation sites for austenite to ferrite transformation as recrystallization is limited. Adapted from [12].

The alloying elements such as Nb, Ti and V raise the T_{nr} so that the processing window for controlled rolling can be opened towards higher temperatures and thus, less waiting time is required. This also eases the rolling loads. The most effective alloying element to raise the T_{nr} is Nb [13]. It is possible to calculate the T_{nr} for a given steel composition through empirical equations of Boratto and Bai [13]:

Boratto equation:

$$T_{nr}(°C) = 887 + 464*\mathbf{C} + \left(6445*\mathbf{Nb} - 644*\sqrt{\mathbf{Nb}}\right) + \left(732*\mathbf{V} - 230*\sqrt{\mathbf{V}}\right) + 890*\mathbf{Ti} + 363*\mathbf{Al} - 357*\mathbf{Si} \quad (1)$$

Bai equation:

$$T_{nr}(°C) = 174\ log\left[\mathbf{Nb}*\left(\mathbf{C} + (12/14)*\mathbf{N}\right)\right] + 1444 \quad (2)$$

In addition to the T_{nr}, another temperature to pay attention to in controlled rolling is the austenite to ferrite transformation start temperature on cooling (A_{r3}) of the steel being rolled. If the rolling is done below the A_{r3} then ferrite grains are also plastically deformed during rolling since the steel is in two phase ($\alpha + \gamma$) region.

The A_{r3} for given steel can be calculated using the Ouchi equation [14]:

$$A_{r3}(°C) = 910 - 310*\mathbf{C} - 80*\mathbf{Mn} - 20*\mathbf{Cu} - 15*\mathbf{Cr} - 55*\mathbf{Ni} - 80*\mathbf{Mo} + 0.35*(t-8), \quad (3)$$

t : *plate thickness* (mm)

Fine ferritic microstructures obtained by sole controlled rolling can satisfy the mechanical properties required for some API grades. However, in order to reach higher strength levels without increasing the carbon content, which deteriorates some properties such as weldability, accelerated cooling right after finish rolling was devised so that even finer and different ferritic microstructures (e.g. acicular, bainitic) can be produced [4, 9]. The practice which utilizes both controlled rolling and accelerated cooling together is called Thermo-Mechanical Controlled Processing (TMCP) [15]. A schematic showing the conventional rolling, thermomechanical controlled rolling and thermomechanical controlled processing is given in Fig. 2.

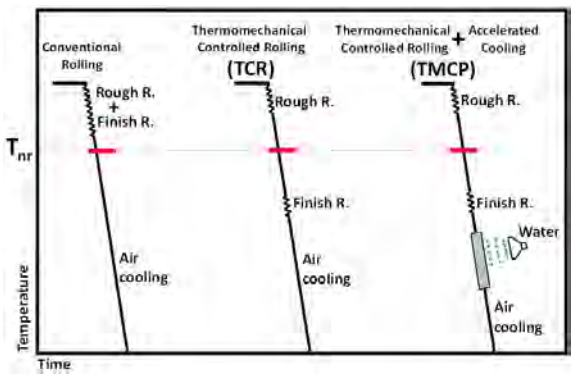

Figure 2. A schematic representation of conventional rolling, thermomechanical controlled rolling (TCR) and thermomechanical controlled processing (TMCP). T_{nr} = Non-recrystallization temperature.

Being an energy corridor in its region, domestic production of coiled API PSL 1 X52 and X60 grade steels with less than 20 mm thickness were previously studied in Turkey [16, 17] and they are commercially available. On the other hand, the domestic production of 20 mm or thicker API PSL 2 X60 and X70 grade steel plates, which are not coiled, was not realized yet in spite of the growing demand.

Producing thicker steel plates of higher grades is not straightforward due to a few reasons. First, the total amount of deformation experienced by the slab decreases as the final plate thickness increases. This, inevitably, makes it more difficult to obtain fine grained microstructures that would give the required strength values. Secondly, satisfying the ductility and toughness requirements of PSL 2 specification brings an additional challenge. Therefore, starting with the appropriate alloying, the controlled rolling and cooling conditions should be combined in such a way that the rolling mill would be able to produce these higher grade steel plates while minimizing the loss in throughput as much as possible.

As a contribution to the pre-commercialization studies [18], the effects of finish rolling temperature and cooling conditions on the production of 20 mm thick API PSL 2 X60 and X70 steel plates from 200 mm thick Nb-Ti microalloyed slabs were investigated in this exploratory work.

MATERIAL AND METHODS

Material

Two full size (12000x2000x200mm) slabs with chemical compositions (Table 2) compliant to the API X60 and X70 grades were sliced into small slabs (2000x2000x200mm) for the plate rolling trials. Trials were done in the hot rolling mill of an integrated iron and steel plant.

Rolling Trials

As mentioned in the Introduction section, the non-recrystallization temperature (T_{nr}) and the austenite to ferrite transformation start temperature (A_{r3}) should be considered when deciding for the controlled rolling conditions. Using the Boratto Eq.(1) and Bai Eq.(2) equations given before the T_{nr} of the slabs used were calculated as 1062°C and 1040°C. The A_{r3} of the slabs were found as 751°C based on the Ouchi formula Eq.(3) .

The finish rolling temperatures and cooling conditions chosen for the rolling trials are listed in Table 3 and graphically shown in Fig. 3. In all trials, the thickness to enter the finish rolling was kept fixed at 60 mm and this corresponds to 70.0 % reduction in rough rolling and 66.7 % reduction in finish rolling, respectively. The number of roll passes and the reduction ratios per pass for the rough rolling (200 mm -> 60 mm) and the finish rolling (60 mm -> 20 mm) stages were automatically determined by the rolling mill control software. A water table was used for the accelerated cooling of the rolled plates in some experiments.

Table 2. API X60/X70 specification and the chemical composition of the slabs used in this work (wt.%).

Element	*C*	*Si*	*Mn*	*P*	*S*	*V*	*Nb*	*Ti*	*Cu*	*N.*	*Cr*	*Mo*
API X60 and X70 (max)	*0.12*	*0.45*	*1.60*	*0.025*	*0.015*		*Nb + V + Ti ≤ 0.15*		*0.50*	*0.50*	*0.50*	*0.50*
Used Slabs (max)	*0.09*	*0.25*	*1.60*	*0.020*	*0.010*	*0.01*	*0.06*	*0.03*	*0.10*	*0.10*	*0.20*	*0.15*

Table 3. Rolling and cooling conditions used in the trial productions.

Trial Code	*Temperature to enter Finish Rolling (°C)*	*Accelerated Cooling after Finish Rolling*
Conventional	*1090*	-
950°C-TCR	*950*	-
950°C-TMCP	*950*	*Yes*
850°C-TCR	*850*	-
850°C-TMCP	*850*	*Yes*
800°C-TCR	*800*	-
800°C-TMCP	*800*	*Yes*

In all trials, the enter and exit temperatures for the rough rolling (200mm -> 60mm) were about 1140°C and 1090°C, respectively.

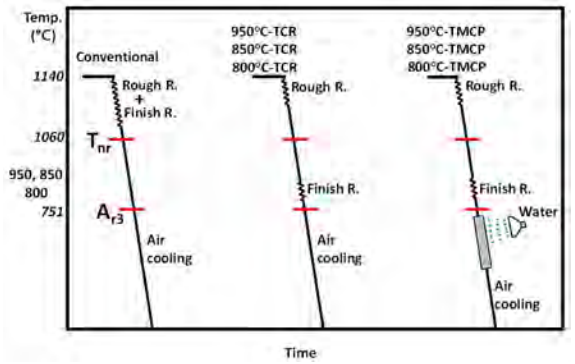

Figure 3. Graphical representation of the rolling and cooling conditions employed in the trials.

Characterization of the Trial Production Plates

Tensile tests, Charpy impact tests, drop weight tear tests (DWTT) and microstructural examinations were performed on the samples cut from the front, middle and end locations along the rolled plates to determine whether the related requirements of API 5L specification (Table 1) were satisfied. Tensile tests were done according to the ASTM A370 [19] standard using a Zwick/Roell Z1200 tensile test machine. The dimensions of the tensile test samples were 38 mm, 50 mm and 250 mm, respectively for the width, gauge and total length as shown in Fig. 4.a. The thickness of the tensile test samples was 20 mm which is the final thickness of the rolled plates. Impact tests were performed at 0°C and -20°C using standard Charpy notched samples of 10 mm*10 mm*55 mm. API RP 5L3 was followed for the DWTT sample dimensions (Fig. 4.b), implementation of the tests and interpretation of the results [20].

Microstructural examinations of 4% nital etched samples were performed using a Nikon Epiphot 200 inverted metallurgical microscope. Average ferrite grain size values of each sample based on the planimetric procedure of the ASTM 112 standard [21] were determined using the Clemex Vision (Clemex Technologies Inc., Longueuil, QC, Canada) and Image J [22] image processing softwares.

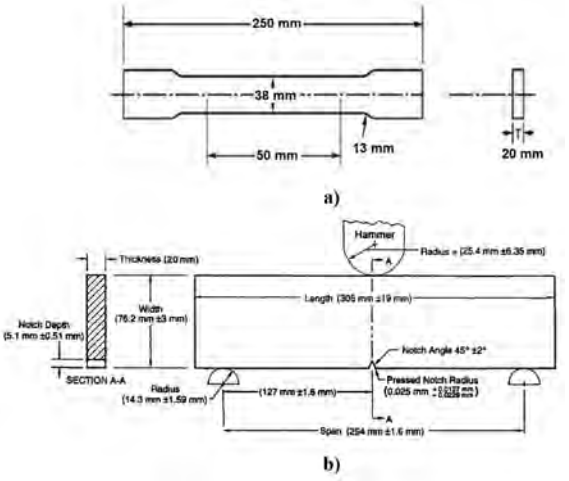

Figure 4. Sample dimensions for a) the tensile tests and b) the DWTT tests.

RESULTS AND DISCUSSION

Tensile Test Results

The results of the tensile tests of the samples taken from the trial production plates are given in Table 4. The yield and tensile strength values of the conventionally rolled sample were determined as 427 MPa and 583 MPa, respectively. The corresponding values were 444 MPa and 585 MPa after finish rolling at 950°C (950°C-TCR), 425 MPa and 550 MPa after finish rolling at 850°C (850°C-TCR) and finally, they were 456 MPa and 562 MPa after finish rolling at 800°C (800°C-TCR). These results show that the yield and tensile strength values of the samples did not change significantly with decreasing finish rolling temperature when only controlled rolling was employed (i.e., no accelerated cooling). In a similar work by Korczak [23] to produce 20 mm thick plates, an average yield strength of 535 MPa and a tensile strength of 618 MPa were obtained after finish rolling of a 0.03% Nb - 0.07% V microalloyed steel at 800°C. However, it should be noted that, in addition to the differences in alloying, the starting slab was thicker (225 mm) and a different rolling schedule (77.8% reduction in rough rolling: 225 mm -> 50 mm, 60.0% reduction in finish rolling: 50 mm -> 20 mm) was used in that study.

The implementation of the accelerated cooling right after the finish rolling significantly increased both the yield and tensile strength values. The yield and tensile strength values of the sample finish rolled at 950°C and then subjected to accelerated cooling (950°C-TMCP) were 511 MPa and 638 MPa, respectively. The corresponding values were 502 MPa and 617 MPa after finish rolling at 850°C with accelerated cooling (850°C-TMCP) and finally, they were 528 MPa and 633 MPa when the finish rolling was done at 800°C

followed by accelerated cooling (800°C-TMCP). Apparently, the application of accelerated cooling greatly improved both yield and tensile strength values while they were still rather independent of the finish rolling temperature.

It was observed that the TMCP samples had significantly higher deviations in their tensile test results as compared to the TCR samples (Table 4). The root cause for this higher deviation is thought to be due to the uneven accelerated cooling of the rolled plates by the water table.

Table 4. Tensile test results of the trial production plates.

Trial Code	Yield Strength (MPa)	Tensile Strength (MPa)	YS / TS Ratio	% Elongation
Conventional	427 ± 6.8	583 ± 5.1	0.73	34.5 ± 0.2
950°C-TCR	444 ± 6.7	585 ± 2.0	0.76	33.3 ± 0.5
850°C-TCR	425 ± 11.8	550 ± 1.5	0.77	34.2 ± 0.4
800°C-TCR	456 ± 6.2	562 ± 1.6	0.81	34.5 ± 0.3
950°C-TMCP	511 ± 28.0	638 ± 20.8	0.80	35.5 ± 1.4
850°C-TMCP	502 ± 38.7	617 ± 20.3	0.81	35.9 ± 2.8
800°C-TMCP	528 ± 34.2	633 ± 27.2	0.83	34.0 ± 1.1

A comparison of the yield and tensile strength values of the trial production plates with the API 5L specification shows that the minimum requirements for the API X60 grade were met by all samples (Fig. 5). On the other hand, the strength requirements of the API X70 grade were satisfied by only three of the seven trial productions, namely, 950°C-TMCP, 850°C-TMCP, and 800°C-TMCP. These results show that accelerated cooling is instrumental in obtaining API X70 grade plates from these slabs.

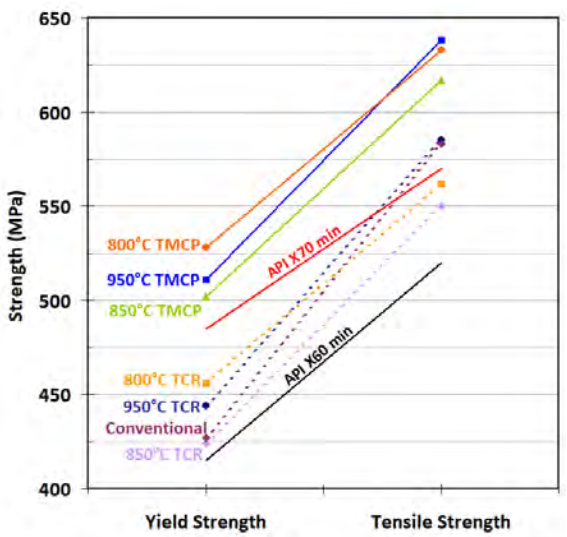

Figure 5. Comparison of the yield and tensile strength values of the trial production plates with the minimum requirements of the API X60 and X70 grades.

Impact Test and DWTT Results

As mentioned previously, the main difference between the PSL 1 and PSL 2 specifications is the requirements towards the deformation behavior of the pipeline steel rather than its strength (see Table 1). The impact test and DWTT results of the trial production plates are given in Table 5. It is found that except 950°C-TCR all samples satisfied the impact energy requirement of API PSL 2.

Table 5. Impact test and DWTT results of the trial production plates.

Trial Code	Impact Test Temperature (°C)	Impact Energy (J)	DWTT (%)
Conventional	-20°C	76 ± 17.2	0
950°C-TCR	-20°C	19 ± 4.8	0
850°C-TCR	-20°C	250 ± 3.4	90
800°C-TCR	-20°C	213 ± 5.9	90
950°C-TMCP	0°C	214 ± 6.7	90
850°C-TMCP	0°C	234 ± 13.8	95
800°C-TMCP	0°C	214 ± 6.9	95

For the DWTT results, the conventionally rolled plate resulted in 0% shear fracture indicating its brittle behavior (Fig. 6.a). Almost the same result was obtained after controlled rolling at 950°C, as seen in Fig. 6.b. Since the requirement of DWTT ≥ 85% is not satisfied, these two plates were appropriately labeled as API PSL 1 X60 based on their strength values. On the other hand, controlled rolling at lower temperatures (850°C-TCR and 800°C-TCR) or the application of accelerated cooling after a higher finish rolling temperature (950°C-TMCP) produced DWTT results with ≥ 85 % shear fracture (see Figure 6.c and Figure 6.d, respectively). Thus, these samples satisfied the ductility requirement of the API PSL 2 specification.

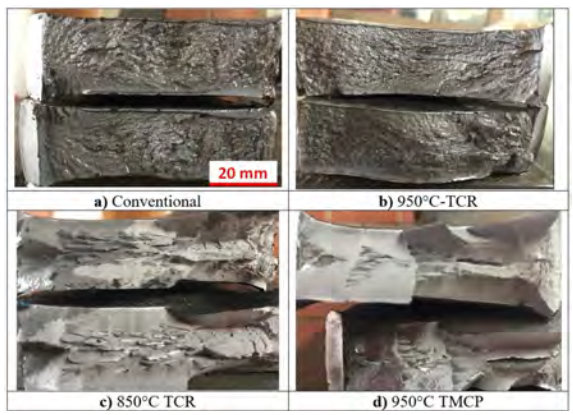

Figure 6. Fracture surfaces of the DWTT samples; a) conventionally rolled, b) finish rolled at 950°C, c) finish rolled at 850°C, and d) finish rolled at 950°C and accelerated cooling applied.

In order to determine the API grades satisfied by the samples, the mechanical properties given in Table 4 and Table 5 were compared with the API requirements listed in Table 1. The rolling conditions of the samples and the corresponding API grades satisfied are listed in Table 6.

Table 6. API grades satisfied by the samples based on their mechanical properties.

Trial Code	*API Grade*
Conventional	*PSL1/X60*
950°C-TCR	*PSL1/X60*
850°C-TCR	*PSL2/X60M*
800°C-TCR	*PSL2/X60M*
950°C-TMCP	*PSL2/X70M*
850°C-TMCP	*PSL2/X70M*
800°C-TMCP	*PSL2/X70M*

Microstructural Examinations

For microstructural examinations, samples were cut from the start, middle and end sections of each trial production plate. Optical microstructural images of the conventionally rolled, 850°C-TCR and 800°C-TMCP samples are given in Fig. 7. In accordance with the tensile test results presented in Table 4, it was observed that finish rolling at a temperature of 850°C (Fig. 7.c-d) and finish rolling at a temperature of 800°C followed by accelerated cooling (Fig. 7.e-f) produced much smaller ferrite grains as compared to the conventional rolling as shown in Fig. 7.a-b. Ferrite was mostly in polygonal form in all samples, which is a typical characteristics found in X60 and X70 grades [24].

Using the optical microstructural images, the average ferrite grain size values of the samples were determined and listed in Table 7. It is clearly observed that the application of accelerated cooling just after finish rolling is very effective in producing smaller grained (3.9 - 4.1 μm) microstructures as compared to the ambient cooling (5.2 - 6.4 μm). The average grain size values determined in this work were inline with the values reported in the literature [25, 26]. For example, in a similar study Masumi et. al found the average ferrite grain size to be around 5-6 μm without accelerated cooling [25]

CONCLUSION

As a part of a study to produce 20 mm thick API PSL 2 X60 and X70 grade steel plates, 200 mm thick Nb-Ti microalloyed slab pieces were rolled at different finish rolling temperatures (conventional, 950°C, 850°C and 800°C) and cooling conditions (ambient or accelerated cooling).

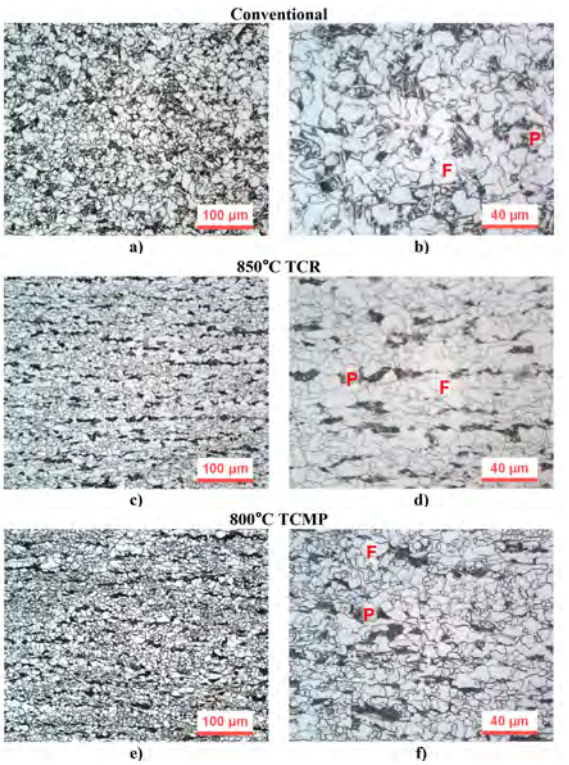

Figure 7. Optical microstructural images of the some of the samples taken from the trial production plates: a)-b) conventionally rolled, c)-d) finish rolled at 850°C, and e)-f) finish rolled at 800°C and accelerated cooled. Images were taken at 200x and 500x for the left and right columns, respectively. Etchant: 4 % nital.

Table 7. Average ferrite grain size values of the samples taken from the trial production plates.

Trial Code	*Average Grain Size (µm)*	*ASTM Grain Size Number*
Conventional	*6.9*	*11.5*
950°C-TCR	*6.4*	*11.5*
850°C-TCR	*5.7*	*12.0*
800°C-TCR	*5.2*	*12.0*
950°C-TMCP	*3.9*	*13.0*
850°C-TMCP	*4.1*	*13.0*
800°C-TMCP	*3.9*	*13.0*

- It is found that the strength requirements of the API X60 grade were easily satisfied in all rolling conditions.
- Very small grained and essentially ferritic microstructures producing the strength values required for the API X70 grade were obtained only when accelerated cooling was applied after the finish rolling.
- The drop weight tear test requirement of the PSL 2 specification was achieved when the finish rolling was started at lower temperatures of 850°C and 800°C regardless of the cooling type or when accelerated cooling was applied after a higher rolling temperature of 950°C.

References

1. The World Factbook, https://www.cia.gov/library/publications/the-world-factbook/fields/383.html (Accessed on 10 June 2020)
2. Hopkins P. Pipelines: Past, Present, and Future, 5th Asian Pacific IIW International Congress, 7–9 March, Sydney, Australia, 2007.
3. Das AK. The Present and the Future of Line Pipe Steels for Petroleum Industry. Materials and Manufacturing Processes 25:1–3, 14–19 (2010). https://doi.org/10.1080/10426910903202427
4. Hillenbrand H-G, Gräf M, Kalwa C. Development and production of high strength pipeline steels. Niobium Science & Technology: Proceedings of the International Symposium Niobium 2001, 2–5 December, Orlando, Florida, USA, 2001.
5. Zhongmin Y. Ultra-Fine Grained Steels: Weng Y. (Ed), Springer-Verlag. Berlin Heidelberg, pp. 53–85, 2009. https://doi.org/10.1007/978-3-540-77230-9
6. Villalobos JC, Del-Pozo A, Campillo B, Mayen J, Serna S. Microalloyed Steels through History until 2018: Review of Chemical Composition, Processing and Hydrogen Service. Metals (2018) 8(5) 351. https://doi.org/10.3390/met8050351
7. Lavigne O, Kotousov A, Luzin V. Microstructural, Mechanical, Texture and Residual Stress Characterizations of X52 Pipeline Steel. Metals (2017) 7(8) 306. https://doi.org/10.3390/met7080306
8. American Petroleum Institute, API Specification 5L, Specification for Line Pipe, Forty-Fifth Edition, December 2012.
9. Rosado DB, De Waele W, Vanderschueren D, Hertelé S. Latest developments in mechanical properties and metallurgical features of high strength line pipe steels. International Journal of Sustainable Construction and Design 4(1) 2013. https://doi.org/10.21825/scad.v4i1.742
10. Zhang G, Bai X, Stalheim D, Li S, Ding W. Development and Production of Heavy Gauge X80 and High Strength X90 Pipeline Steels Utilizing TMCP/Optimized Cooling Process. In: Proceedings of the 10th International Pipeline Conference IPC2014, Calgary, Alberta, Canada, 33265, 2014. https://doi.org/10.1115/IPC2014-33265
11. Outinen J, Mäkeläinen P. Mechanical properties of structural steel at elevated temperatures and after cooling down. Fire and Materials 28 (2-4) (2004) 237–251. https://doi.org/10.1002/fam.849
12. Vervynckt S, Verbeken K, Lopez B, Jonas JJ. Modern HSLA steels and role of non-recrystallisation temperature. Int. Mater. Rev. 57:4 (2012) 187–207. https://doi.org/10.1179/1743280411Y.0000000013
13. Homsher CN. Determination of the non-recrystallization temperature (TNR) in multiple microalloyed steels. MS Thesis, Colorado School of Mines, Colorado, USA, 2013.
14. Quchi C, Sampei T, Kozasu I. The Effect of Hot Rolling Condition and Chemical Composition on the Onset Temperature of - ✣- Transformation after Hot Rolling. Transactions ISIJ 22 (1982) 214–222. https://doi.org/10.2355/isijinternational1966.22.214
15. Tsuyama S. Thick Plate Technology for the Last 100 Years: A World Leader in Thermo Mechanical Control Process. ISIJ International 55–1 (2015) 67-78. http://dx.doi.org/10.2355/isijinternational.55.67
16. Bakkaloğlu A. Effect of processing parameters on the microstructure and properties of an Nb microalloyed steel. Materials Letters 56 (2002) 200-209. https://doi.org/10.1016/S0167-577X(02)00440-8
17. Mahmutoğlu MZ. Microstructure-Mechanical Property Characterization of a Line Pipe Steel Containing Niobium and Vanadium (in Turkish). Ph.D. Thesis, İstanbul Technical University, Istanbul, Turkey, (2003)
18. Gunes S. Production of API X60 and X70 Grade Steel Plates by Thermomechanical Controlled Rolling. MS Thesis, Atılım University, Ankara, Turkey, (2018).
19. ASTM A370-19e1, Standard Test Methods and Definitions for Mechanical Testing of Steel Products, ASTM International, West Conshohocken, PA, 2019, www.astm.org. https://doi.org/10.1520/A0370-19E01
20. API RP 5L3, Recommended Practice for Conducting Drop-Weight Tear Tests on Line Pipe third edition, February, American Petroleum Institute, 1996.
21. ASTM E112-13, Standard Test Methods for Determining Average Grain Size, ASTM International, West Conshohocken, PA, 2013, www.astm.org. https://doi.org/10.1520/E0112-13
22. Rasband WS. ImageJ. U.S. National Institutes of Health: Bethesda, MD, USA, https://imagej.nih.gov/ij/ 1997-2018.
23. Korczak P. Influence of controlled rolling condition on microstructure and mechanical properties of low carbon micro-alloyed steels. Journal of Materials Processing Technology 157-158 (2004) 553-556. https://doi.org/10.1016/j.jmatprotec.2004.07.113
24. Godefroid LB, Cândido LC, Toffolo RVB, Barbosa LHS. Microstructure and Mechanical Properties of Two Api Steels for Iron Ore Pipelines. Materials Research 17(Suppl. 1) (2014) 114-120. http://dx.doi.org/10.1590/S1516-14392014005000068
25. Masoumi M, Echeverri EAA, Silva CC, Beres M, Abreu HFG. Effect of Different Thermomechanical Processes on the Microstructure, Texture, and Mechanical Properties of API 5L X70 Steel. Journal of Materials Engineering and Performance 27 (2018) 1694-1705. https://doi.org/10.1007/s11665-018-3276-z
26. Lan L-Y, Qiu C-L, Zhao D-W, Gao X-H. Microstructural Evolution and Mechanical Properties of Nb-Ti Microalloyed Pipeline Steel. Journal of Iron and Steel Research International 18(2) (2011) 57-63. https://doi.org/10.1016/S1006-706X(11)60024-1

Hittite Journal of Science and Engineering, 2020, 7 (2) 157-162
ISSN NUMBER: 2148-4171
DOI: 10.17350/HJSE19030000184

Microstructure and Mechanical Properties of CoCrFeNi(Ti-Al) High Entropy Alloys

Ilkay Kalay
Cankaya University, Department of Materials Science and Engineering, Ankara, Turkey

ABSTRACT

The structure and mechanical properties of CoCrFeNi and CoCrFeNi$Ti_{0.5}Al_{0.5}$ (in molar ratio) high entropy alloys were investigated using X-ray diffraction (XRD), optical microscope (OM), scanning electron microscope (SEM), hardness and compression tests. With the addition of Ti and Al, the crystal structure of CoCrFeNi changed from FCC to a mixture of FCC and double BCC structures. The lattice parameter of FCC increases upon addition of Al and Ti. The microstructure analysis shows the morphological transition of dendrites from non-equiaxed to equiaxed during the suction casting of CoCrFeNi$Ti_{0.5}Al_{0.5}$ alloy. The Vickers microhardness testing of CoCr-FeNi alloy reveals significant increase in hardness with the addition of Al and Ti. The hardness values are improved in as-suction cast CoCrFeNi and CoCrFeNi$Ti_{0.5}Al_{0.5}$ alloys compared to their as-cast alloys due to strengthening. The CoCrFeNi$Ti_{0.5}Al_{0.5}$ alloy yields at 1997 MPa and fails at 2344 MPa. The fracture mechanism of CoCrFeNi$Ti_{0.5}Al_{0.5}$ alloy reveals a cleavage mode.

Keywords:
High entropy alloys; Microstructure; Microhardness; Compression test; Metallic alloys.

Article History:
Received: 2020/04/16
Accepted: 2020/06/17
Online: 2020/06/26

***Correspondence to**: Ilkay Kalay, Cankaya University, Materials Science and Engineering, 06790, Ankara, TURKEY*
E-Mail: ikalay@cankaya.edu.tr
Phone: +90 312 233 1394
Fax: +90 312 233 1026

INTRODUCTION

Attributed to the combinations of their unique and remarkable properties such as superior high temperature strength, high strength, high hardness, outstanding magnetic properties, excellent oxidation and corrosion resistance, high entropy alloys (HEAs) have attracted much attention [1-5]. Since the proposed concept of HEA by Cantor and et al. [1] and Yeh and et al. [2-4], a number of HEAs, such as the single phase solid solution HEAs, multiphase solid solution HEAs, refractory HEAs [5], amorphous HEAs [6], light weight HEAs [7] and magnetic HEAs [8] have been identified. HEAs were originally expressed as solid solutions composed of five or more principal metallic elements taken into equiatomic or nearly equiatomic proportions between 5 and 35 at.%. The liquid or random solid solutions of the alloys have higher entropy of mixing. Besides principal elements, these alloys can include secondary elements with compositions less than 5 at.%. Even HEAs have typically at least 5 constituent elements, they have simple crystal structures such as face centered cubic (FCC) [9-11], body centered cubic (BCC) [12-14] or hexagonal centered cubic (HCP) [15-17]. However, the HEAs concept has been developed recently as many HEAs have complex multiphase structures rather than a single crystal structure. There are four core effects determined related to the formation of HEAs. These effects can be given as the high entropy, severe-lattice distortion, sluggish diffusion and cocktail effects. Yang and Zhang [18] proposed other important factors are the ratio of mixing entropy, ΔS_{mix} to the mixing enthalpy, ΔH_{mix}, that is $(\frac{\Delta S_{mix}}{\Delta H_{mix}}) = \Omega$, atomic size difference, δ, and valance electron concentrations (VEC). They reported that HEAs can be produced in case $\Omega \geq 1.1$ and $\delta \leq$ % 6.6. ΔH_{mix} and ΔS_{mix} can be expressed as:

$$\Delta H_{mix} = \sum_{i=1,\, j\neq 1}^{n} \Omega_{ij} c_i c_j \quad (1)$$

and

$$\Delta S_{mix} = -R \sum_{i}^{n} c_i \ln c_i \quad (2)$$

where $\Omega_{ij} = 4\Delta H_{AB}$ for binary systems, R is the gas constant, c_i is the atomic percent of i^{th} element. VEC is

$$VEC = \sum_{i}^{n} c_i (\mathrm{VEC})_i \quad (3)$$

Here, $(VEC)_i$ is the valence electron concentration of ith element. VEC is a critical parameter for designing

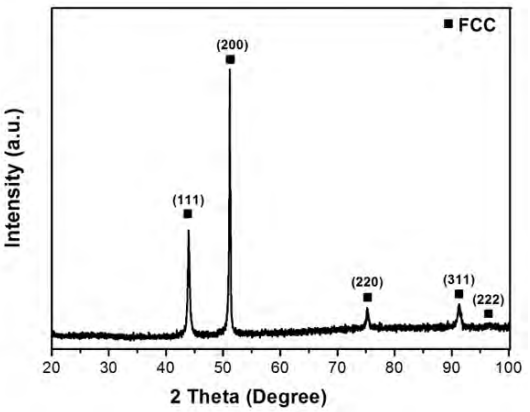

Figure 1. XRD pattern of as-cast CoCrFeNi alloy.

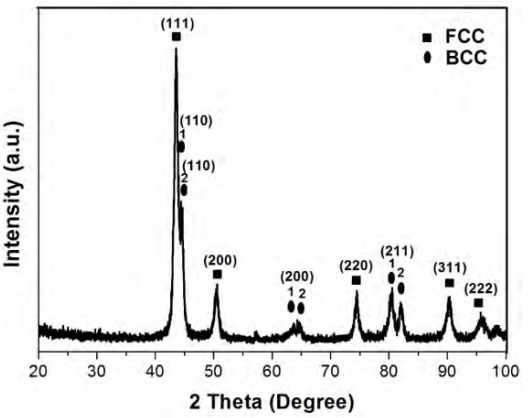

Figure 2. XRD pattern of as-cast $CoCrFeNiTi_{0.5}Al_{0.5}$ alloy.

the compositions of HEAs that relates the structure and strength and ductility. Previous studies reported that when VEC > 8.0, the FCC solid solution is stable, when VEC < 6.87, the BCC solid solution is stable and when 6.87≤VEC<8.0, the structure of HEA will be multiphase consisted of FCC and BCC [19]. Furthermore, HEAs may also contain the coexistence of ordered and disordered forms of the same structure. The presence of BCC and ordered BCC (B2) phases together [20-22] and the coexistence of FCC and ordered FCC (LI_2) phases [23] were reported previously.

In particular, CoCrFeNi HEA has attracted much attention attributed to its outstanding fracture toughness and ductility [24-26]. However, its poor strength values restrict their potential applicability as structural materials. Recently, Liu et al. [27] reported the tensile strength of 1.2 GPa and tensile strain of 18.9% when Mo is added to CoCrFeNi HEAs. Subsequently, Lu et al. [28] proposed that $AlCoCrFeNi_{2.1}$ alloy exhibits a fracture tensile strength of 944-1050 MPa and tensile strain of 17%-25.6%. The work reported here is aimed to investigate the effect of Ti and Al on the structure and mechanical properties of CoCrFeNi HEA and concentrated on $CoCrFeNiTi_{0.5}Al_{0.5}$ alloy using several characterization techniques including XRD, OM, SEM, hardness and compression tests.

MATERIAL AND METHODS

The alloy ingots with nominal compositions of CoCrFeNi and $CoCrFeNiTi_{0.5}Al_{0.5}$ alloys were produced by Edmund Bühler MAM-1 vacuum arc melter with turbomulecular pumping system HVT52/G using highly pure elements (0.999 Al, Ti, Ni, Fe, Cr and Co, by weight) in the bulk form under an Ar atmosphere. The alloy ingots with a mass of 3-5 g were reprocessed three times to ensure homogeneity. The ingots were then cast into copper molds with diameters of 3 mm via suction casting to obtain higher cooling rates during solidification. The effects of cooling rate during suction casting on microstructure and mechanical properties were also investigated. The structural analysis of the as-cast and suction-cast alloys was carried out by D8 Advance Bruker X-ray Diffractometer using Cu-Kα radiation (λ=1.5406 Å). The tube voltage and current of diffractometer were 40 kV and 30 mA, respectively. The diffraction data were collected in a diffraction angle range from 20° to 100° with a scanning rate of 0.5°/min. XRD analysis was carried out on the bulk form of rod specimens which were initially ground to remove any oxide layer. The microstructural analysis of the alloys was performed using Nikon Eclipse LV150 digital camera Optical microscope and FEI Nova NanoSEM 430 Scanning electron microscope. The Nova NanoSEM 430 operated at 20-30 kV. The OM and SEM specimens were initially ground, polished and etched using a mixture of 67 vol. % methanol and 33 vol. % nitric acid (HNO3) solution. The SEM imaging was performed in secondary electron mode. Compression tests were carried out using MTS Criterion Model 45 universal testing machine (100 kN) to investigate the yield and compressive strengths of $CoCrFeNiTi_{0.5}Al_{0.5}$ alloy. During compression tests, the gauge dimensions of the specimens were adjusted to be 3.0 ± 0.3 mm in diameter and 6.0 ± 0.3 mm in length to keep an aspect ratio of 2:1. The crosshead speed and strain rate were chosen as 0.03 mm/min and 10^{-4} s^{-1}, respectively. The fractography analysis was carried out using OM and SEM. The hardness tests were carried out using InnovaTest Nexus 7501 Universal Hardness Tester. The Vickers micro-hardness tests due to ASTM standard E92 were performed using a test load of 10 kgf with a dwell time of 10 s. At least 10 indentations were performed for each specimen. The Vickers Hardness (HV) values were also converted into MPa by multiplying by 9.807.

RESULTS AND DISCUSSION

The ΔH_{mix}, ΔS_{mix} and VEC values of CoCrFeNi and $CoCrFeNiTi_{0.5}Al_{0.5}$ and alloys were calculated using equ-

Table 1. Thermodynamic data of the alloys.

Alloy	ΔH_{mix} (J/mol)	ΔS_{mix} (J/mol.K)	VEC
CoCrFeNi	-3.78	11.53	8.25
$CoCrFeNiTi_{0.5}Al_{0.5}$	-15.52	14.53	7.29

ations (1), (2) and (3), respectively and tabulated in Table 1. The expected crystal structures based on calculated VEC values are FCC for CoCrFeNi and FCC+BCC for $CoCrFeNiTi_{0.5}Al_{0.5}$ alloy. Fig. 1 indicates the XRD diffractogram of CoCrFeNi alloy. It is clear that as-cast CoCrFeNi alloy shows only the diffraction peaks associated with FCC phase as expected from VEC calculations. Fig. 2 indicates the XRD pattern of $CoCrFeNiTi_{0.5}Al_{0.5}$ alloy. It is observed that the new diffraction peaks corresponding to BCC phases appear with the addition of Al and Ti. XRD analysis of $CoCrFeNiTi_{0.5}Al_{0.5}$ alloy reveals the existence of FCC + double BCC (BCC_1 and BCC_2) structure. The lattice parameters (a) of the corresponding BCC and FCC structures were calculated from the indexed XRD patterns. The lattice parameters were determined using the combination of Bragg's Law ($\lambda = 2d\sin\theta$), where λ=1.5406 Å for CuKα radiation, θ is the Bragg's angle, d is the interplanar spacing) and d-spacing equation

Table 2. Lattice parameters of the main constituent phases of the alloys.

Alloy	a_{FCC} (nm)	$a_{BCC(1)}$ (nm)	$a_{BCC(2)}$ (nm)
CoCrFeNi	0.357 ±0.0005	-	-
$CoCrFeNiTi_{0.5}Al_{0.5}$	0.360 ±0.0009	0.293 ±0.0009	0.288 ±0.0005

for cubic structures ($\left(\frac{1}{d^2} = \frac{h^2+k^2+l^2}{a^2}\right)$), where h, k, l are the indices of the corresponding planes). Table 2 tabulates the lattice parameters of the corresponding crystal structures of the alloys. The lattice parameter of the FCC structure in the CoCrFeNi alloy was determined as 0.357 nm, based on the interplanar spacing of peaks from XRD pattern. The corresponding lattice parameters of FCC, BCC_1 and BCC_2 phases in $CoCrFeNiTi_{0.5}Al_{0.5}$ alloy were determined as 0.360 nm, 0.293 nm and 0.288 nm, respectively. The lattice parameter of FCC increases with the further addition of Al and Ti. Al and Ti have the largest atomic size in the system therefore distortions and enlargement occur in the crystal lattice of $CoCrFeNiTi_{0.5}Al_{0.5}$.

The SEM images of as-cast $CoCrFeNiTi_{0.5}Al_{0.5}$ alloy are presented in Fig. 3 (a, b). The microstructure of the as-

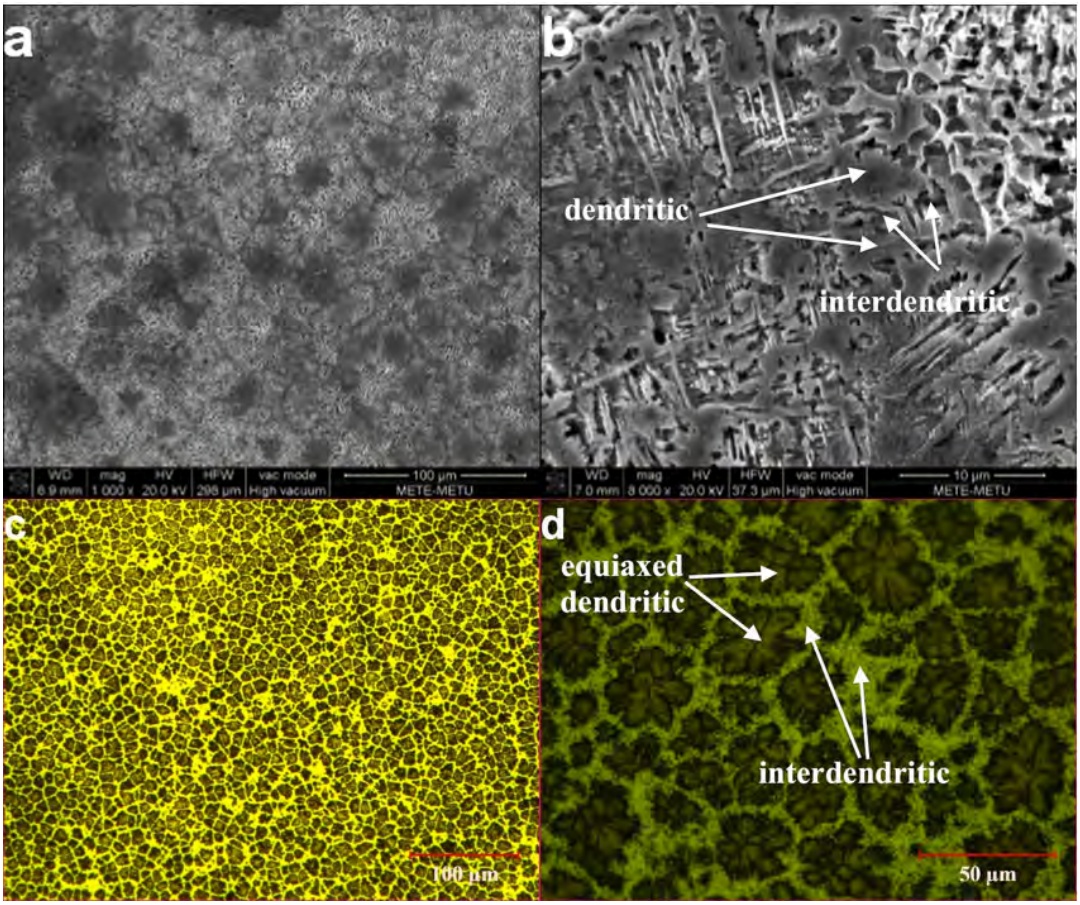

Figure 3. (a-b) SEM images of as cast $CoCrFeNiTi_{0.5}Al_{0.5}$ alloy, (c-d) OM images of as suction cast 3 mm diameter $CoCrFeNiTi_{0.5}Al_{0.5}$ rod.

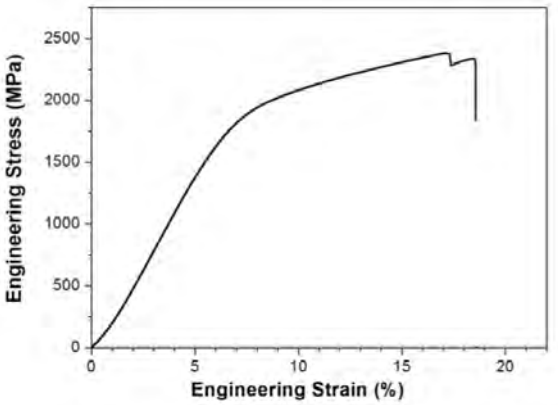

Figure 4. The compressive stress-strain curve of $CoCrFeNiTi_{0.5}Al_{0.5}$ alloy at room temperature.

cast $CoCrFeNiTi_{0.5}Al_{0.5}$ alloy exhibits two distinct regions; dendritic and interdendritic, which are typical of many HEAs after casting. It is clear that even within the dendritic and interdendritic regions, contrast differences are observed due to the variable chemical compositions. Fig. 3 (c, d) indicate the optical microscope images of 3 mm diameter suction-cast $CoCrFeNiTi_{0.5}Al_{0.5}$ alloy. The micrographs show the dendritic and interdendritic structures. It should be noted that Al is a strongest stabilizer of the BCC structure leading to the formation dual BCC modulated microstructure in $CoCrFeNiTi_{0.5}Al_{0.5}$ system. By the addition of Al, complete FCC structure changes to FCC+BCC structures. With the addition of Ti, dual BCC phase were observed in $CoCrFeNiTi_{0.5}Al_{0.5}$ alloy. Fig. 3 (a-d) reveals that the structure of dendrites has also been changed from non-equiaxed dendritic grain to equiaxed dendritic grains during suction casting of the alloy.

The compressive engineering stress-strain diagram of $CoCrFeNiTi_{0.5}Al_{0.5}$ alloy is given in Fig. 4. The compressive yield strength and the fracture strength were determined as 1997 MPa and 2344 MPa, respectively. Wang et al. [29] reported the yield stress and compressive strength as 1250.96 MPa and 2004.23 MPa, respectively for AlCoCrFeNi alloy. Our findings for $CoCrFeNiTi_{0.5}Al_{0.5}$ alloy show that the yield strength and compressive strength values are enhanced by the addition of Ti compared to that of AlCoCrFeNi alloy [29]. The microhardness test results were determined as 107±5 HV (1049¬±49.0 MPa) and 134±22 HV (1314±215.8

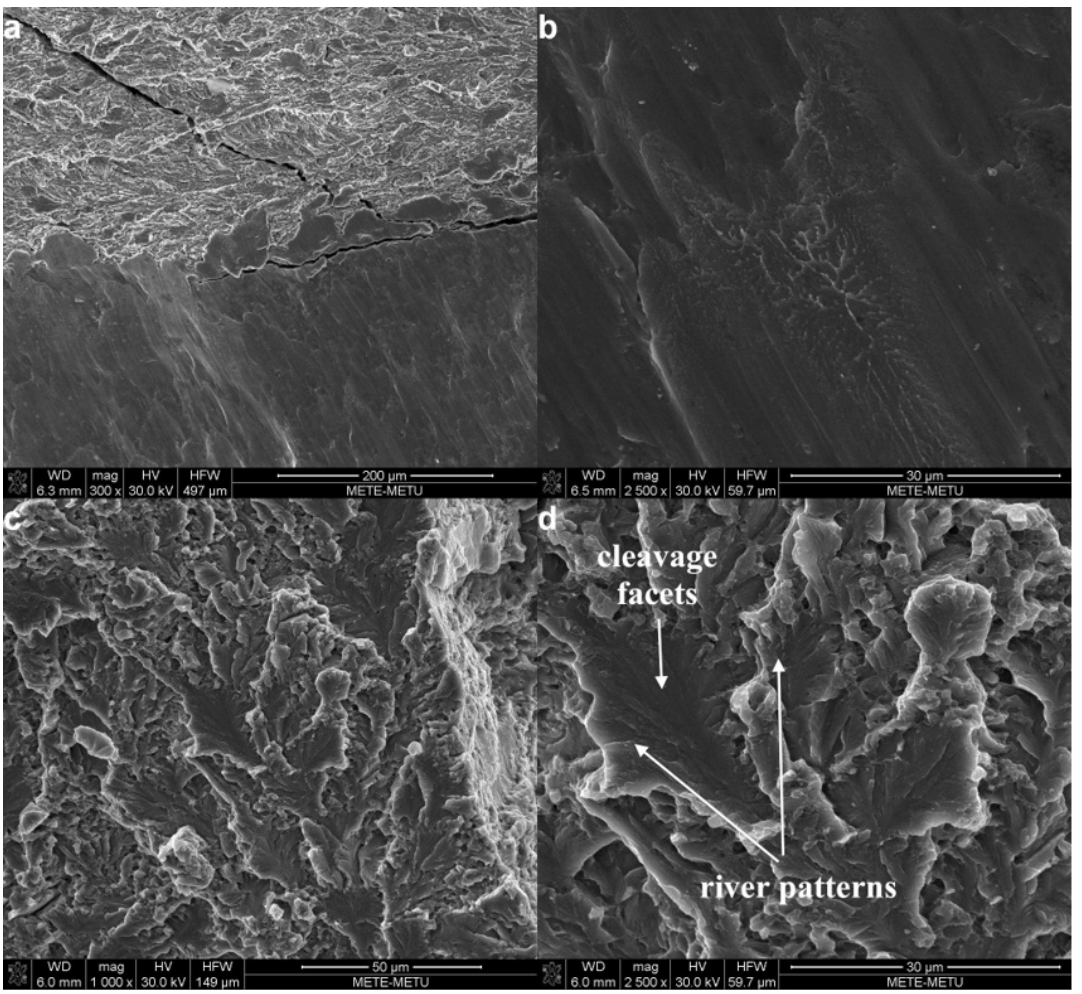

Figure 5. (a-d) SEM micrographs of fractured surfaces of CoCrFeNiTi0.5Al0.5 alloy.

MPa) for as-cast and as-suction cast CoCrFeNi HEAs, respectively. The hardness values were determined as 488±15 HV (4786±147 MPa) and 647±14 HV (6345±137.3 MPa) for as-cast and as-suction cast CoCrFeNiTi0.5Al0.5 alloys, respectively. The hardness value is increasing significantly with the addition of Al and Ti due to the change in crystal structure from FCC in CoCrFeNi alloy to FCC + double BCC in $CoCrFeNiTi_{0.5}Al_{0.5}$ alloy. The formation of BCC phase creates an interface between FCC and BCC structures therefore the dislocation movement is hindered and due to strengthening, the hardness of the alloy is improved. Furthermore, the lattice distortion due to the formation of BCC structure also increases the activation energy of dislocation motion. This results in solid solution strengthening and thus increases the hardness of the alloy. The as-suction cast $CoCrFeNiTi_{0.5}Al_{0.5}$ alloy has higher hardness value than its as-cast alloy. CoCrFeNi alloy also has the same trend. This is mainly caused by the change in cooling rate and thus the microstructure of the produced alloy during suction casting. The reduction in grain size by increasing cooling rate improves the strength of the suction cast alloy.

SEM micrographs of the fractured surface of $CoCrFeNiTi_{0.5}Al_{0.5}$ are illustrated in Fig. 5. The fractured surface of $CoCrFeNiTi_{0.5}Al_{0.5}$ alloy shows a typical cleavage fracture implying a brittle character. The surface of the alloys reveals the cleavage facets and river patters. It is clear that the patterns are propagating along either the grain boundaries or transgranular cleavage planes. Cleavage or quasi-cleavage features are generally observed on the fracture surface HEAs with BCC or BCC+FCC structures [42].

CONCLUSION

The structure and mechanical properties of CoCrFeNi and $CoCrFeNiTi_{0.5}Al_{0.5}$ HEAs were examined using XRD, OM, SEM, compressive fracture and hardness testing. The alloys were prepared via vacuum arc melting and the alloy rods were synthesized by suction casting technique. With the addition of Ti and Al to CoCrFeNi HEA, the crystal structure has changed from FCC to a mixture of double BCC (BCC_1 and BCC_2) and FCC structures. The hardness values were also increased by the addition of Al and Ti. Furthermore, the suction-cast $CoCrFeNiTi_{0.5}Al_{0.5}$ alloy exhibited the higher hardness value compared to its as-cast alloy due to the grain refinement by rapid cooling during suction casting operation. The compression test revealed that $CoCrFeNiTi_{0.5}Al_{0.5}$ high entropy alloy yields at 1997 MPa and resists up to 2344 MPa. SEM analysis of fractured surface of $CoCrFeNiTi_{0.5}Al_{0.5}$ alloy reveals a cleavage mode.

References

1. Cantor B, Chang ITH, Knight P, Vincent AJB. Microstructural development in equiatomic multicomponent alloys. Materials Science and Engineering A 375–377 (2004) 213– 218.
2. Yeh JW, Chen YL, Lin SJ, Chen SK. High-Entropy Alloys – A New Era of Exploitation. Materials Science Forum 560 (2007) 1–9.
3. Yeh JW, Chen SK, Lin SJ, Gan JY, Chin TS, Shun TT, Tsau CH, Chang SY. Nanostructured high-entropy alloys with multiple principal elements: Novel alloy design concepts and outcomes. Advanced Engineering Materials 6 (2004) 299–303.
4. Wu JM, Lin SJ, Yeh JW, Chen SK, Huang YS, Chen HC. Adhesive wear behavior of AlxCoCrCuFeNi high-entropy alloys as a function of aluminum content. Wear 261 (2006) 513–519.
5. Senkov ON, Miracle DB, Chaput KJ, Couzinie JP. Development and exploration of refractory high-entropy alloys—a review. Journal of Materials Research 33 (2018) 3192-3133.
6. Hu Q, Guo S, Wang J, et al. Parametric Study of Amorphous High-Entropy Alloys formation from two New Perspectives: Atomic Radius Modification and Crystalline Structure of Alloying Elements. Science Reports 7 (2017) 39917.
7. Feng R, Gao MC, Lee C, Mathes M, Zuo T, Chen S, Hawk JA, Zhang Y, Liaw PK. Design of Light-Weight High-Entropy Alloys. Entropy 18 (2016) 333.
8. Lucas MS, Mauger L, Muñoz JA, Xiao Y, Xiao Y, Sheets AO, Semiatin SL, Horwath J, Turgut Z. Magnetic and vibrational properties of high-entropy alloys. Journal of Applied Physics 109 (2011) 07E307.
9. Gali A, George E. P. Tensile properties of high- and medium-entropy alloys. Intermetallics 39 (2013) 74–78.
10. Tsai KY, Tsai MH, Yeh JW. Sluggish diffusion in Co–Cr–Fe–Mn–Ni high-entropy alloys. Acta Mater. 61 (2013) 4887–4897.
11. Liu WH, Wu Y, He JY, Nieh TG, Lu ZP. Grain growth and the Hall-Petch relationship in a highentropy FeCrNiCoMn alloy. Scr. Mater. 68 (2013) 526–529.
12. 12. Senkov ON, Woodward CF. Microstructure and properties of a refractory NbCrMo0.5Ta0.5TiZr alloy. Mater. Sci. Eng. A 529 (2011) 311–320.
13. Senkov ON, Wilks GB, Scott JM, Miracle DB. Mechanical properties of Nb25Mo25Ta25W25 and V20Nb20Mo20Ta20W20 refractory high entropy alloys. Intermetallics 19 (2011) 698–706.
14. Senkov ON, Scott JM, Senkova SV, Miracle DB, Woodward CF. Microstructure and room temperature properties of a high-entropy TaNbHfZrTi alloy. J. Alloys. Compd. 509 (2011) 6043–6048.
15. Takeuchi A, Amiya K, Wada T, Yubuta K, Zhang W. High-entropy alloys with a hexagonal close-packed structure designed by equi-atomic alloy strategy and binary phase diagrams. JOM 66 (2014) 1984–1992.
16. Feuerbacher M, Heidelmann M, Thomas C. Hexagonal high-entropy alloys. Mater. Res. Lett. 3 (2015) 1–6.
17. Zhao YJ et al. A hexagonal close-packed highentropy alloy: the effect of entropy. Mater. Des. 96 (2016) 10–15.
18. Yang X, Zhang Y. Prediction of high-entropy stabilized solid-solution in multi-component alloys. Materials Chemistry and Physics 132 (2–3) (2012) 233-238.
19. Guo S, Ng C, Lu J, Liu CT. Effect of valence electron concentration on stability of fcc or bcc phase in high entropy alloys. Journal of Applied Physics 109 (2011) 103505.

20. Singh S, Wanderka N, Murty BS, Glatzel U, Banhart J. Decomposition in multi component AlCoCrCuFeNi high-entropy alloy. Acta Materialia 59 (2011) 182–190.
21. Tsai MH, Yuan H, Cheng G, Xu W, Jian WW, Chuang MH, Juan CC, Yeh AC, Lin SJ, Zhu Y. Significant hardening due to the formation of a sigma phase matrix in a high entropy alloy. Intermetallics 33 (2013) 81–86.
22. Tong CJ, Chen YL, Chen SK, Yeh JW, Shun TT, Tsau CH, Lin SJ, Chang SY. Microstructure characterization of AlxCoCrCuFeNi high-entropy alloy system with multiprincipal elements. Metallurgical Materials and Transactions A 36 (2005) 881–893.
23. Tsai MH, Yuan H, Cheng G, Xu W, Tsai KY, Tsai CW, Jian WW, Juan CC, Shen WJ, Chuang MH, Yeh JW, Zhu YT. Morphology, structure and composition of precipitates in Al0.3CoCrCu0.5FeNi high-entropy alloy. Intermetallics 32 (2013) 329–336.
24. Meshkov II, Novoselov EA, Shapeev AV, Yanilkin AV. Sublattice formation in CoCrFeNi high-entropy alloy. Intermetallics 112 (2019) 106542.
25. Wang B, Haiyan H, Naeem M, et al. Deformation of CoCrFeNi high entropy alloy at large strain. Scripta Materialia 115 (2018) 54-57.
26. Guo S, Ng C, Wang Z, Liu CT. Solid solutioning in equiatomic alloys: limit set by topological instability. Journal of Alloys and Compounds 583 (2014) 410-413.
27. Liu WH, Lu ZP, He JY, Luan JH, Wang ZJ, Liu B,Liu Y, Chen MW, Liu CT. Ductile CoCrFeNiMox high entropy alloys strengthened by hard intermetallic phases. Acta Materialia 116 (2016) 332-342.
28. Lu Y. P., Gao X., Jiang L., Chen Z., et al. Directly cast bulk eutectic and near-eutectic high entropy alloys with balanced strength and ductility in a wide temperature range. Acta Materialia 214 (2017) 143-150.
29. Wang YP, Li BS, Ren MX, Yang C, Fu HZ. Microstructure and compressive properties of AlCrFeCoNi high entropy alloy. Materials Science and Engineering: A 491 (2008) 154-158.